

*Textures and Majorana Excitations
in Multi-Component
Neutral Fermi Superfluids*

2011, March

YASUMASA TSUTSUMI

Graduate School of Natural Science and Technology

(Doctor's Course)

OKAYAMA UNIVERSITY

Abstract

Textures and Majorana excitations in multi-component neutral Fermi superfluids of ^3He atoms and atomic gases are investigated. The superfluid ^3He consists of p -wave Cooper pairs without doubt. Since the interaction of atomic gases can be tuned by the Feshbach resonance, superfluids of Fermi atomic gases through a p -wave scattering will be realized in the near future. Such p -wave superfluids construct a spatial structure of the superfluid order parameter (OP), i.e. texture, by vortices or boundary conditions to lower free energy using the multi-component OP thoroughly. Fermi superfluids have low energy excitations at vortices and boundaries, where a superfluid gap is suppressed. Certain excitations in p -wave Fermi superfluids behave as Majorana quasi-particles (QPs) or Majorana fermions. Existence of the Majorana excitations at vortices and boundary in p -wave Fermi superfluids reflects that p -wave superfluids can be regarded as topological superfluids. Textures and Majorana excitations in the superfluid ^3He and superfluids of p -wave atomic gases are discussed in connection with realistic experiments.

First, recent experiments for the textures of the superfluid ^3He A-phase confined in a narrow cylinder are discussed. Compared to the experiments, the radial disgyration, Mermin-Ho texture, and Pan-Am texture are calculated by the Ginzburg-Landau (GL) theory. The radial disgyration is stable at rest for the cylinders by using the experiments, and the Mermin-Ho texture is stable under rotation. The results show good agreement with the experimental results.

Features of the Majorana excitations are different for a chiral superfluid and helical superfluid, which are different in the topological nature. In the superfluid ^3He , the chiral superfluid is realized in the A-phase and the helical superfluid is realized in the B-phase. Then, we calculate the Majorana edge state for the superfluid ^3He in a realistic slab using the quasi-classical theory. For the A-phase, dispersion relation of the QPs at the edge constructs a Dirac valley. For the B-phase, dispersion relation of the QPs at the edge constructs a Majorana cone. The Majorana QPs exist both phases. Based on a result, we suggest experiments to observe the Majorana QPs.

Finally, textures for superfluids of p -wave atomic gases are calculated by the GL theory. The textures are different from the superfluid ^3He by the boundary condition, because Fermi atomic gases are confined in harmonic trap potential by a magnetic field. In quasi-two dimensional trap potential, conditions to stabilize a quantized vortex with Majorana QP for trap frequency and rotation frequency are derived. This work is helpful to confirm superfluidity and apply the system to a topological quantum computer when superfluids of p -wave Fermi atomic gases are realized in the future.

Acknowledgments

I would like to express my gratitude to Professor Kazushige Machida whose comments and suggestions were of inestimable value for my study. He has guided me to accomplishment of my research by proper advice and prepared environment in which I can concentrate on my investigation.

I would like to thank Professor Masanori Ichioka for invaluable comments and providing the fundamental computer program for solving the Eilenberger equation and Ginzburg-Landau equation which formed the basis of my research. I would also like to thank Professor Takeshi Mizushima for helpful discussions. In particular, I can understand Majorana excitations by his instruction.

I am indebted to Dr. Ken Izumina, Professor Ryosuke Ishiguro, Professor Minoru Kubota, Professor Osamu Ishikawa, Professor Yutaka Sasaki, and Professor Takeo Takagi for helpful discussions about the experiments in ISSP, Univ. of Tokyo. I am also indebted to Professor Tetsuo Ohmi for helpful discussions about the superfluid ^3He .

I want to thank everyone in the Mathematical Physics Laboratory for advice about research and life.

Finally, I would like to acknowledge the financial support of the Research Fellowships of the Japan Society for the Promotion of Science for Young Scientists.

Contents

1	Introduction	1
1.1	Background	1
1.2	Outline of this thesis	1
2	Formulation of superfluidity	3
2.1	Bogoliubov-de Gennes theory	5
2.2	Gor'kov theory	5
2.3	Quasi-classical theory	7
2.3.1	Eilenberger equation	7
2.3.2	Riccati equations	8
2.4	Ginzburg-Landau theory	9
3	Multi-component neutral Fermi superfluids	11
3.1	Superfluid ^3He	11
3.1.1	Texture	13
3.1.2	Half-quantum vortex	13
3.2	Fermi atomic gases	14
3.2.1	Feshbach resonance	15
3.2.2	p -wave resonant Fermi atomic gases	16
4	Majorana excitations	19
4.1	Majorana quasi-particle in vortex	19
4.1.1	Non-Abelian statistics	23
4.2	Majorana edge fermion	24
4.2.1	Chiral edge state	24
4.2.2	Helical edge state	25
5	Superfluid ^3He in a cylinder	29
5.1	Formulation	31
5.1.1	Ginzburg-Landau functional for the superfluid ^3He	31
5.1.2	Numerics and boundary condition	33
5.2	Stable textures	34
5.2.1	Radial disgyration (RD)	34
5.2.2	Mermin-Ho (MH)	37
5.2.3	Pan-Am texture	37
5.3	Size-dependence and magnetic field effects	40
5.3.1	Size-dependence and the critical rotation speed	40
5.3.2	Magnetic field effect	41

5.4	Analysis of experiments	43
5.4.1	$R=50 \mu\text{m}$	43
5.4.2	$R=115 \mu\text{m}$	44
5.5	Summary	45
6	Superfluid ^3He in a slab	47
6.1	Quasi-classical theory and order parameter	48
6.2	System geometry and numerical methods	50
6.3	A-phase	51
6.3.1	$D = 8\xi_0$: Thin slab for A-phase	52
6.3.2	$D = 14\xi_0$: Thick slab for A-phase	54
6.4	B-phase	56
6.4.1	$D = 30\xi_0$: Thick slab for B-phase	57
6.4.2	$D = 14\xi_0$: Thin slab for B-phase	59
6.4.3	Dependence of the energy splitting on the thickness	60
6.5	Discussion	61
6.5.1	Majorana zero modes in the A- and B-phases	61
6.5.2	Stripe phase	61
6.5.3	Experimental proposal	62
6.6	Summary	63
7	p-wave resonant superfluids of Fermi atomic gases	65
7.1	Formulation	66
7.2	Preliminary considerations	68
7.3	Cigar shape trap	69
7.3.1	Stable texture at rest	69
7.3.2	Half-quantum vortex under rotation	71
7.4	Pancake shape trap	73
7.4.1	Axis symmetric texture at rest	73
7.4.2	Vortices under rotation	75
7.5	Quasi-2D trap	75
7.5.1	Possible types of axisymmetric structure and a vortex	78
7.5.2	Stability region of the singular vortex	79
7.6	Summary	84
8	Conclusion	87
8.1	Summary of this thesis	87
8.2	Future studies	88
A	Symmetry of quasi-classical Green's function	89
B	Angular momentum of the A-phase in a slab	91
B.1	Angular momentum by Matsubara Green's function	92
B.2	Angular momentum by retarded Green's function	93
C	Ginzburg-Landau functional under rotation	97
D	Bulk energy in Ginzburg-Landau functional	99

Chapter 1

Introduction

1.1 Background

Superconductivity was discovered by Kamerlingh Onnes in 1911. After decades, phenomenological Ginzburg-Landau (GL) theory and microscopic Bardeen-Cooper-Schrieffer (BCS) theory give a fundamental understanding of the conventional superconductivity.

In neutral Fermi systems, the first superfluid phase was discovered in the liquid ^3He by Osheroff *et al.* [1] The superfluid ^3He is unconventional in which Cooper pairs have the spin-triplet p -wave symmetry [2]. This understanding progressed by generalization of the BCS theory. The GL theory gives understanding of textures (spatial structures of superfluid order parameter) and exotic vortices (e.g. a half-quantum vortex). However, since the experiment of the superfluid ^3He is required low temperature of the order of mK, various assignments have remained yet. Moreover, the superfluid ^3He is one of the candidate systems in which Majorana quasi-particles (QPs) and fermions live. They are discussed also in the condensed matter physics recently [3].

Another progress of neutral Fermi superfluidity is in ultra-cold Fermi atomic gases [4]. In 1995, Bose-Einstein condensates (BECs) were realized for Bose atomic gases [5, 6, 7]. After about 10 years, BECs by molecules of Fermi atoms were observed [8, 9, 10]. Shortly after then, superfluids by Cooper pairs of Fermi atoms were also observed [11, 12]. Recently, molecules of Fermi atoms through a p -wave scattering can be create [13, 14, 15, 16, 17, 18]. In the near future, BECs by p -wave molecules and superfluids by Cooper pairs with p -wave interaction are expected. The superfluids of p -wave Fermi atomic gases involve textures, exotic vortices, and Majorana QPs and fermions. The Fermi atomic gases have the advantage of maneuverability than the superfluid ^3He .

1.2 Outline of this thesis

In this thesis, p -wave superfluids of neutral Fermi systems are discussed theoretically. This thesis has two main subjects which are textures and Majorana excitations. p -wave superfluids construct a texture by vortices or boundary conditions to lower free energy using the multi-component superfluid order parameter (OP) thoroughly. Fermi superfluids have low energy excitations at vortices and boundaries, where a superfluid gap is suppressed. Certain excitations in p -wave Fermi superfluids behave as Majorana QPs or Majorana fermions. They are discussed in connection with realistic experiments.

The general formulation of superfluidity within the mean-field theory is discussed in

Chap. 2. Starting from the BCS Hamiltonian, the Bogoliubov-de Gennes (BdG) equation is derived by the unitary transformation. By the BdG equation, we can demonstrate that certain low energy excitations in p -wave superfluids behaves as Majorana QPs or Majorana fermions. Another way from the BCS Hamiltonian is to derive the Gor'kov equation using Green's function. By quasi-classical approximation of the Gor'kov equation, we derive the Eilenberger equation and Riccati equations with quasi-classical Green's function. The Eilenberger equation and Riccati equations are used for the calculation of the QP state in Chap. 6. In the vicinity of the superfluid transition temperature, the Ginzburg-Landau (GL) theory is derived from the symmetric consideration. The GL theory is used for the discussion of textures in Chaps. 5 and 7.

In Chap. 3, we introduce the superfluid ^3He and the superfluid of p -wave resonant Fermi atomic gases, which are multi-component neutral Fermi superfluids. The superfluid ^3He is typical matter of p -wave neutral Fermi superfluids. Textures and a half-quantum vortex in the superfluid ^3He are also introduced in this chapter. The superfluid of p -wave resonant Fermi atomic gases using Feshbach resonances are expected in the near future.

Majorana QPs and Majorana fermions are introduced in Chap. 4. A zero energy excitation at a vortex with an odd integer winding number behaves as a Majorana QP in p -wave superfluids. The Majorana QPs obey non-Abelian statistics, so that they can be utilized for a topological quantum computer. The Andreev bound states at the edge of p -wave superfluids are described by field operators of the Majorana fermions. There are two kinds of edge state: The chiral edge state appears in the superfluid ^3He A-phase, and the helical edge state appears in the B-phase.

In Chap. 5, our theoretical results are compared to recent experiments for the textures of the superfluid ^3He A-phase confined in a narrow cylinder [19, 20]. Textures consist of few vortices can be observed because the rotating cryostat in ISSP, Univ. of Tokyo achieves high rotation speed. Compared to the experiments, the radial disgyration, Mermin-Ho texture, and Pan-Am texture are calculated by the GL theory. The radial disgyration is stable at rest for the cylinders by using the experiments, and the Mermin-Ho texture is stable under rotation. The results show good agreement with the experimental results.

We calculate the Majorana edge state for the superfluid ^3He in a realistic slab using the quasi-classical theory [21, 22, 23] in Chap. 6. For the A-phase, dispersion relation of the QPs at the edge constructs a Dirac valley. For the B-phase, dispersion relation of the QPs at the edge constructs a Majorana cone. The Majorana QPs exist both phases. Based on a result, we suggest experiments to observe the Majorana QPs.

In Chap. 7, textures for superfluids of p -wave atomic gases are calculated by the GL theory [24, 25]. The textures are different from the superfluid ^3He by the boundary condition, because Fermi atomic gases are confined in harmonic trap potential. In quasi-two dimensional trap potential, there is a vortex with Majorana QP [26]. This work is helpful when superfluids of p -wave Fermi atomic gases are realized in the future.

The final chapter devotes for a summary of this thesis and a view for future studies.

Chapter 2

Formulation of superfluidity

The Bardeen-Cooper-Schrieffer (BCS) Hamiltonian with fermion field operators $\psi_\alpha(\mathbf{r})$ in the Schrödinger picture is

$$\mathcal{H}_{\text{BCS}} = \sum_{\alpha\beta} \int d^3r_1 d^3r_2 \left[\psi_\alpha^\dagger(\mathbf{r}_1) K_{\alpha\beta}(\mathbf{r}_1, \mathbf{r}_2) \psi_\beta(\mathbf{r}_2) + \frac{1}{2} \sum_{\delta\gamma} V_{\alpha,\beta}^{\gamma,\delta}(r_{12}) \psi_\alpha^\dagger(\mathbf{r}_1) \psi_\beta^\dagger(\mathbf{r}_2) \psi_\gamma(\mathbf{r}_2) \psi_\delta(\mathbf{r}_1) \right], \quad (2.1)$$

where

$$K_{\alpha\beta}(\mathbf{r}_1, \mathbf{r}_2) \equiv \delta_{\alpha\beta} \delta(\mathbf{r}_1 - \mathbf{r}_2) \left[-\frac{\hbar^2 \nabla^2}{2m} - \mu \right] + \Sigma_{\alpha\beta}(\mathbf{r}_1, \mathbf{r}_2), \quad (2.2)$$

includes kinetic term, chemical potential μ , and self-energy $\Sigma_{\alpha\beta}(\mathbf{r}_1, \mathbf{r}_2)$. If the interaction $V_{\alpha,\beta}^{\gamma,\delta}(r_{12})$ is invariant under rotation in the spin space,

$$V_{\alpha,\beta}^{\gamma,\delta}(r_{12}) = V_1(r_{12}) \delta_{\alpha\delta} \delta_{\beta\gamma} + V_2(r_{12}) \boldsymbol{\sigma}_{\alpha\delta} \cdot \boldsymbol{\sigma}_{\beta\gamma}, \quad (2.3)$$

where $\hat{\boldsymbol{\sigma}}$ is the Pauli matrix in the spin-1/2 space and $r_{12} \equiv |\mathbf{r}_1 - \mathbf{r}_2|$. Here, we define the order parameter (OP) of the superfluid state as

$$\begin{aligned} \Delta_{\alpha\beta}(\mathbf{r}_1, \mathbf{r}_2) &\equiv \sum_{\gamma\delta} V_{\alpha,\beta}^{\gamma,\delta}(r_{12}) \langle \psi_\gamma(\mathbf{r}_2) \psi_\delta(\mathbf{r}_1) \rangle, \\ \Delta_{\alpha\beta}^*(\mathbf{r}_1, \mathbf{r}_2) &\equiv \sum_{\gamma\delta} V_{\delta,\gamma}^{\beta,\alpha}(r_{12}) \langle \psi_\delta^\dagger(\mathbf{r}_1) \psi_\gamma^\dagger(\mathbf{r}_2) \rangle, \end{aligned} \quad (2.4)$$

where $\langle \dots \rangle$ denotes statistical average. The statistical average of field operators is decomposed into the orbital and spin parts: $\langle \psi_\gamma(\mathbf{r}_2) \psi_\delta(\mathbf{r}_1) \rangle \equiv \chi(\mathbf{r}_1, \mathbf{r}_2) \phi(\gamma, \delta)$. Then, the spin function satisfies $\sum_{\gamma\delta} \boldsymbol{\sigma}_{\alpha\delta} \cdot \boldsymbol{\sigma}_{\beta\gamma} \phi(\gamma, \delta) = -3\phi(\beta, \alpha)$ for the spin-singlet state and $\sum_{\gamma\delta} \boldsymbol{\sigma}_{\alpha\delta} \cdot \boldsymbol{\sigma}_{\beta\gamma} \phi(\gamma, \delta) = \phi(\beta, \alpha)$ for the spin-triplet state. Hence, we find

$$\sum_{\gamma\delta} V_{\alpha,\beta}^{\gamma,\delta} \phi(\gamma, \delta) = [V_1(r_{12}) + \lambda V_2(r_{12})] \phi(\beta, \alpha) \equiv V(r_{12}) \phi(\beta, \alpha), \quad (2.5)$$

where $\lambda = -3$ for the spin-singlet state and $\lambda = 1$ for the spin-triplet state. Therefore, the definition of the OP can be rewritten as

$$\begin{aligned}\Delta_{\alpha\beta}(\mathbf{r}_1, \mathbf{r}_2) &\equiv V(r_{12}) \langle \psi_\beta(\mathbf{r}_2) \psi_\alpha(\mathbf{r}_1) \rangle, \\ \Delta_{\alpha\beta}^*(\mathbf{r}_1, \mathbf{r}_2) &\equiv V(r_{12}) \langle \psi_\alpha^\dagger(\mathbf{r}_1) \psi_\beta^\dagger(\mathbf{r}_2) \rangle.\end{aligned}\quad (2.6)$$

Here, we perform the mean-field approximation for the BCS Hamiltonian. The mean-field Hamiltonian is described by

$$\begin{aligned}\mathcal{H} = \sum_{\alpha\beta} \int d^3r_1 d^3r_2 &\left[\psi_\alpha^\dagger(\mathbf{r}_1) K_{\alpha\beta}(\mathbf{r}_1, \mathbf{r}_2) \psi_\beta(\mathbf{r}_2) \right. \\ &+ \frac{1}{2} \Delta_{\alpha\beta}^*(\mathbf{r}_1, \mathbf{r}_2) \psi_\beta(\mathbf{r}_2) \psi_\alpha(\mathbf{r}_1) + \frac{1}{2} \Delta_{\alpha\beta}(\mathbf{r}_1, \mathbf{r}_2) \psi_\alpha^\dagger(\mathbf{r}_1) \psi_\beta^\dagger(\mathbf{r}_2) \\ &\left. - \frac{1}{2} \frac{\Delta_{\alpha\beta}(\mathbf{r}_1, \mathbf{r}_2) \Delta_{\alpha\beta}^*(\mathbf{r}_1, \mathbf{r}_2)}{V(r_{12})} \right],\end{aligned}\quad (2.7)$$

where the last term can be included in c -number E_0 .

Here, we introduce the four dimensional Nambu spinor $\Psi(\mathbf{r})$ and the 4×4 matrix $\widehat{K}(\mathbf{r}_1, \mathbf{r}_2)$ and $\widehat{\Delta}(\mathbf{r}_1, \mathbf{r}_2)$ as

$$\Psi(\mathbf{r}) \equiv \left[\psi_\uparrow(\mathbf{r}), \psi_\downarrow(\mathbf{r}), \psi_\uparrow^\dagger(\mathbf{r}), \psi_\downarrow^\dagger(\mathbf{r}) \right]^T, \quad (2.8)$$

$$\begin{aligned}\widehat{K}(\mathbf{r}_1, \mathbf{r}_2) &\equiv \begin{pmatrix} \widehat{K}(\mathbf{r}_1, \mathbf{r}_2) & 0 \\ 0 & -\widehat{K}^T(\mathbf{r}_2, \mathbf{r}_1) \end{pmatrix}, \\ \widehat{K}(\mathbf{r}_1, \mathbf{r}_2) &\equiv \begin{pmatrix} \delta(\mathbf{r}_1 - \mathbf{r}_2) \left[-\frac{\nabla^2}{2m} - \mu_\uparrow \right] + \Sigma_{\uparrow\uparrow}(\mathbf{r}_1, \mathbf{r}_2) & \Sigma_{\uparrow\downarrow}(\mathbf{r}_1, \mathbf{r}_2) \\ \Sigma_{\downarrow\uparrow}(\mathbf{r}_1, \mathbf{r}_2) & \delta(\mathbf{r}_1 - \mathbf{r}_2) \left[-\frac{\nabla^2}{2m} - \mu_\downarrow \right] + \Sigma_{\downarrow\downarrow}(\mathbf{r}_1, \mathbf{r}_2) \end{pmatrix},\end{aligned}\quad (2.9)$$

$$\widehat{\Delta}(\mathbf{r}_1, \mathbf{r}_2) \equiv \begin{pmatrix} 0 & \widehat{\Delta}(\mathbf{r}_1, \mathbf{r}_2) \\ \widehat{\Delta}^\dagger(\mathbf{r}_2, \mathbf{r}_1) & 0 \end{pmatrix}, \quad \widehat{\Delta}(\mathbf{r}_1, \mathbf{r}_2) \equiv \begin{pmatrix} \Delta_{\uparrow\uparrow}(\mathbf{r}_1, \mathbf{r}_2) & \Delta_{\uparrow\downarrow}(\mathbf{r}_1, \mathbf{r}_2) \\ \Delta_{\downarrow\uparrow}(\mathbf{r}_1, \mathbf{r}_2) & \Delta_{\downarrow\downarrow}(\mathbf{r}_1, \mathbf{r}_2) \end{pmatrix}, \quad (2.10)$$

where the superscript T indicates transposed matrices and $\mu_{\uparrow,\downarrow}$ is chemical potential including local self-energy $\Sigma_{\uparrow\uparrow}(\mathbf{r}, \mathbf{r})$ or $\Sigma_{\downarrow\downarrow}(\mathbf{r}, \mathbf{r})$. The OP yields the symmetry $\Delta(\mathbf{r}_2, \mathbf{r}_1) = \pm \Delta(\mathbf{r}_1, \mathbf{r}_2)$, where the sign $+$ is for the spin-singlet state and $-$ is for the spin-triplet state. In the following, the ‘‘ordinary hat’’ indicates the 2×2 matrix in spin space and the ‘‘wide hat’’ indicates the 4×4 matrix in Nambu and spin spaces. Using the spinor and matrices, the mean-field Hamiltonian is rewritten as

$$\mathcal{H} = E_0 + \frac{1}{2} \int d^3r_1 d^3r_2 \Psi^\dagger(\mathbf{r}_1) \left[\widehat{K}(\mathbf{r}_1, \mathbf{r}_2) + \widehat{\Delta}(\mathbf{r}_1, \mathbf{r}_2) \right] \Psi(\mathbf{r}_2). \quad (2.11)$$

In this chapter, based on the mean-field Hamiltonian eq. (2.7) or eq. (2.11), we formulate equations described to the superfluid state. In Sec. 2.1, the Bogoliubov-de Gennes (BdG) equation is derived by the unitary transformation from eq. (2.11). The BdG equation is helpful to understand Majorana excitations. In Sec. 2.2, we obtain the Gor’kov equations with

Green's function from eq. (2.7). By quasi-classical approximation of the Gor'kov equations, we obtain the Eilenberger equation with quasi-classical Green's function in Sec. 2.3. From the Eilenberger equation, we obtain the Riccati equations which are convenient for analytical and numerical calculation. In Sec. 2.4, we obtain the Ginzburg-Landau (GL) free energy functional from the symmetric consideration. The GL free energy functional is also obtained from the microscopic theory. The quasi-classical theory and GL theory give main results in this thesis.

2.1 Bogoliubov-de Gennes theory

We introduce the unitary transformation, so-called the Bogoliubov transformation, which transforms the spinor $\Psi(\mathbf{r})$ to the basis composed of the quasi-particle (QP) operator γ_ν :

$$\Psi(\mathbf{r}) = \sum_{\nu} \hat{u}_{\nu}(\mathbf{r}) \gamma_{\nu}, \quad \gamma_{\nu} \equiv \left[\gamma_{\nu,\uparrow}, \gamma_{\nu,\downarrow}, \gamma_{\nu,\uparrow}^{\dagger}, \gamma_{\nu,\downarrow}^{\dagger} \right]^T, \quad (2.12)$$

where the QP operator γ_{ν} satisfies the fermion commutation relations,

$$\left\{ \gamma_{\nu,\alpha}, \gamma_{\mu,\beta}^{\dagger} \right\} = \delta_{\alpha\beta} \delta_{\nu\mu}, \quad \left\{ \gamma_{\nu,\alpha}, \gamma_{\mu,\beta} \right\} = \left\{ \gamma_{\nu,\alpha}^{\dagger}, \gamma_{\mu,\beta}^{\dagger} \right\} = 0. \quad (2.13)$$

The unitary 4×4 matrix $\hat{u}_{\nu}(\mathbf{r})$ must fulfill the orthonormal and completeness conditions,

$$\int d^3r \hat{u}_{\nu}^{\dagger}(\mathbf{r}) \hat{u}_{\mu}(\mathbf{r}) = \delta_{\nu\mu} \hat{\sigma}_0, \quad (2.14)$$

$$\sum_{\nu} \hat{u}_{\nu}^{\dagger}(\mathbf{r}_1) \hat{u}_{\nu}(\mathbf{r}_2) = \delta(\mathbf{r}_1 - \mathbf{r}_2) \hat{\sigma}_0, \quad (2.15)$$

where $\hat{\sigma}_0$ is the 4×4 unit matrix.

Using the QP basis defined in eq. (2.12), we find that the mean-field Hamiltonian in eq. (2.11) can be diagonalized as

$$\mathcal{H} = E_0 + \frac{1}{2} \sum_{\nu} \gamma_{\nu}^{\dagger} \hat{E}_{\nu} \gamma_{\nu}, \quad \hat{E}_{\nu} \equiv \text{diag} [E_{\nu,\uparrow}, E_{\nu,\downarrow}, -E_{\nu,\uparrow}, -E_{\nu,\downarrow}], \quad (2.16)$$

where $\text{diag}[\dots]$ indicates diagonal matrices. Then, the matrix \hat{u}_{ν} must fulfill the Bogoliubov-de Gennes (BdG) equation:

$$\int d^3r_2 \left[\hat{K}(\mathbf{r}_1, \mathbf{r}_2) + \hat{\Delta}(\mathbf{r}_1, \mathbf{r}_2) \right] \hat{u}_{\nu}(\mathbf{r}_2) = \hat{u}_{\nu}(\mathbf{r}_1) \hat{E}_{\nu}. \quad (2.17)$$

2.2 Gor'kov theory

Thermal Green's function is defined by

$$\begin{aligned} \hat{G}_{\alpha\beta}(r_1, r_2) &\equiv \begin{pmatrix} G_{\alpha\beta}(r_1, r_2) & F_{\alpha\beta}(r_1, r_2) \\ \underline{F}_{\alpha\beta}(r_1, r_2) & \underline{G}_{\alpha\beta}(r_1, r_2) \end{pmatrix} \\ &\equiv \begin{pmatrix} -\left\langle T_{\tau} \left[\tilde{\psi}_{\alpha}(r_1) \tilde{\psi}_{\beta}^{\dagger}(r_2) \right] \right\rangle & -\left\langle T_{\tau} \left[\tilde{\psi}_{\alpha}(r_1) \tilde{\psi}_{\beta}(r_2) \right] \right\rangle \\ -\left\langle T_{\tau} \left[\tilde{\psi}_{\alpha}^{\dagger}(r_1) \tilde{\psi}_{\beta}^{\dagger}(r_2) \right] \right\rangle & -\left\langle T_{\tau} \left[\tilde{\psi}_{\alpha}^{\dagger}(r_1) \tilde{\psi}_{\beta}(r_2) \right] \right\rangle \end{pmatrix}, \end{aligned} \quad (2.18)$$

where

$$\begin{aligned}\tilde{\psi}_\alpha(r) &= e^{\mathcal{H}\tau/\hbar}\psi_\alpha(\mathbf{r})e^{-\mathcal{H}\tau/\hbar}, \\ \tilde{\psi}_\alpha^\dagger(r) &= e^{\mathcal{H}\tau/\hbar}\psi_\alpha^\dagger(\mathbf{r})e^{-\mathcal{H}\tau/\hbar},\end{aligned}\quad (2.19)$$

are field operators in the Heisenberg picture and (r) indicates (\mathbf{r}, τ) . From eq. (2.7), the imaginary time-derivative of the field operators are

$$\begin{aligned}\hbar\frac{\partial}{\partial\tau_1}\tilde{\psi}_\alpha(r_1) &= \sum_\beta \int d^3r_2 \left[-K_{\alpha\beta}(\mathbf{r}_1, \mathbf{r}_2)\tilde{\psi}_\beta(\mathbf{r}_2, \tau_1) - \Delta_{\alpha\beta}(\mathbf{r}_1, \mathbf{r}_2)\tilde{\psi}_\beta^\dagger(\mathbf{r}_2, \tau_1) \right], \\ \hbar\frac{\partial}{\partial\tau_1}\tilde{\psi}_\alpha^\dagger(r_1) &= \sum_\beta \int d^3r_2 \left[K_{\beta\alpha}(\mathbf{r}_2, \mathbf{r}_1)\tilde{\psi}_\beta^\dagger(\mathbf{r}_2, \tau_1) - \Delta_{\beta\alpha}^*(\mathbf{r}_2, \mathbf{r}_1)\tilde{\psi}_\beta(\mathbf{r}_2, \tau_1) \right].\end{aligned}\quad (2.20)$$

Using eq. (2.20) we can calculate the imaginary time-derivative of the Green's function. The imaginary time-derivative of the Green's function gives Gor'kov equations:

$$\begin{aligned}\sum_\gamma \int d^3r_3 \begin{pmatrix} -\hbar\frac{\partial}{\partial\tau_1}\delta_{\alpha\gamma}\delta(\mathbf{r}_1 - \mathbf{r}_3) - K_{\alpha\gamma}(\mathbf{r}_1, \mathbf{r}_3) & -\Delta_{\alpha\gamma}(\mathbf{r}_1, \mathbf{r}_3) \\ -\Delta_{\gamma\alpha}^*(\mathbf{r}_3, \mathbf{r}_1) & -\hbar\frac{\partial}{\partial\tau_1}\delta_{\alpha\gamma}\delta(\mathbf{r}_1 - \mathbf{r}_3) + K_{\gamma\alpha}(\mathbf{r}_3, \mathbf{r}_1) \end{pmatrix} \\ \times \hat{G}_{\gamma\beta}(\mathbf{r}_3\tau_1, \mathbf{r}_2\tau_2) = \hbar\delta_{\alpha\beta}\delta(\mathbf{r}_1 - \mathbf{r}_2)\hat{\sigma}_0,\end{aligned}\quad (2.21)$$

$$\begin{aligned}\sum_\gamma \int d^3r_3 \hat{G}_{\alpha\gamma}(\mathbf{r}_1\tau_1, \mathbf{r}_3\tau_2) \\ \times \begin{pmatrix} \hbar\frac{\partial}{\partial\tau_2}\delta_{\gamma\beta}\delta(\mathbf{r}_3 - \mathbf{r}_2) - K_{\gamma\beta}(\mathbf{r}_3, \mathbf{r}_2) & -\Delta_{\gamma\beta}(\mathbf{r}_3, \mathbf{r}_2) \\ -\Delta_{\beta\gamma}^*(\mathbf{r}_2, \mathbf{r}_3) & \hbar\frac{\partial}{\partial\tau_2}\delta_{\gamma\beta}\delta(\mathbf{r}_3 - \mathbf{r}_2) + K_{\beta\gamma}(\mathbf{r}_2, \mathbf{r}_3) \end{pmatrix} \\ = \hbar\delta_{\alpha\beta}\delta(\mathbf{r}_1 - \mathbf{r}_2)\hat{\sigma}_0,\end{aligned}\quad (2.22)$$

where the imaginary time-derivative $\partial/\partial\tau_2$ operates the left side of the Green's function.

The Gor'kov equations are more convenient in the frequency representation. By Fourier transformation,

$$\hat{G}_{\alpha\beta}(\mathbf{r}_1\tau_1, \mathbf{r}_2\tau_2) = \frac{k_B T}{\hbar} \sum_n e^{-i\omega_n(\tau_1 - \tau_2)} \hat{G}_{\alpha\beta}(\mathbf{r}_1, \mathbf{r}_2, \omega_n),\quad (2.23)$$

$$\delta(\tau_1 - \tau_2) = \frac{k_B T}{\hbar} \sum_n e^{-i\omega_n(\tau_1 - \tau_2)},\quad (2.24)$$

where $\omega_n = (2n + 1)\pi k_B T/\hbar$ is the Matsubara frequency with integer n . The Gor'kov equations are rewritten as

$$\begin{aligned}\sum_\gamma \int d^3r_3 \begin{pmatrix} i\hbar\omega_n\delta_{\alpha\gamma}\delta(\mathbf{r}_1 - \mathbf{r}_3) - K_{\alpha\gamma}(\mathbf{r}_1, \mathbf{r}_3) & -\Delta_{\alpha\gamma}(\mathbf{r}_1, \mathbf{r}_3) \\ -\Delta_{\gamma\alpha}^*(\mathbf{r}_3, \mathbf{r}_1) & i\hbar\omega_n\delta_{\alpha\gamma}\delta(\mathbf{r}_1 - \mathbf{r}_3) + K_{\gamma\alpha}(\mathbf{r}_3, \mathbf{r}_1) \end{pmatrix} \\ \times \hat{G}_{\gamma\beta}(\mathbf{r}_3, \mathbf{r}_2, \omega_n) = \hbar\delta_{\alpha\beta}\delta(\mathbf{r}_1 - \mathbf{r}_2)\hat{\sigma}_0,\end{aligned}\quad (2.25)$$

$$\begin{aligned}\sum_\gamma \int d^3r_3 \hat{G}_{\alpha\gamma}(\mathbf{r}_1, \mathbf{r}_3, \omega_n) \\ \times \begin{pmatrix} i\hbar\omega_n\delta_{\gamma\beta}\delta(\mathbf{r}_3 - \mathbf{r}_2) - K_{\gamma\beta}(\mathbf{r}_3, \mathbf{r}_2) & -\Delta_{\gamma\beta}(\mathbf{r}_3, \mathbf{r}_2) \\ -\Delta_{\beta\gamma}^*(\mathbf{r}_2, \mathbf{r}_3) & i\hbar\omega_n\delta_{\gamma\beta}\delta(\mathbf{r}_3 - \mathbf{r}_2) + K_{\beta\gamma}(\mathbf{r}_2, \mathbf{r}_3) \end{pmatrix} \\ = \hbar\delta_{\alpha\beta}\delta(\mathbf{r}_1 - \mathbf{r}_2)\hat{\sigma}_0.\end{aligned}\quad (2.26)$$

2.3 Quasi-classical theory

We introduce the center-of-mass coordinate $\mathbf{R} = (\mathbf{r}_1 + \mathbf{r}_2)/2$ and the relative coordinate $\mathbf{r} = \mathbf{r}_1 - \mathbf{r}_2$. The Green's function is rewritten as

$$\widehat{G}_{\alpha\beta}(\mathbf{r}_1, \mathbf{r}_2, \omega_n) = \int \frac{d^3k}{(2\pi)^3} \widehat{G}_{\alpha\beta}(\mathbf{R}, \mathbf{k}, \omega_n) e^{i\mathbf{k}\cdot\mathbf{r}}, \quad (2.27)$$

where \mathbf{k} is the relative momentum.

The quasi-classical approximation is valid when $\Delta/E_F \ll 1$, or $\xi k_F \gg 1$, where Δ is superfluid gap, E_F is the Fermi energy, ξ is superfluid coherence length, and k_F is the Fermi wave number. The condition is satisfied for most superconductors and the superfluid ^3He , in which $\Delta/E_F \sim 10^{-3}$, and even for high- T_c superconductors, in which $\Delta/E_F \sim 10^{-2}$. Under the condition, the Green's function has a peak with a width of Δ at the Fermi surface. Then, k -dependence of the Green's function can be integrated by the energy $\xi_k = \hbar^2 k^2/(2m) - \mu$, and the relative momentum in the other integrand can be replaced by the Fermi momentum \mathbf{k}_F . The unimportant rapid oscillating term $\exp(i\mathbf{k}_F \cdot \mathbf{r})$ can be neglected, because we take the limit $r \rightarrow 0$ for calculation of physical quantities from the Green's function. The quasi-classical Green's function is defined in Nambu space by

$$\int d\xi_k \widehat{\sigma}_z \widehat{G}(\mathbf{R}, \mathbf{k}, \omega_n) \equiv \widehat{g}(\mathbf{R}, \mathbf{k}_F, \omega_n) \equiv -i\pi \begin{pmatrix} \widehat{g}(\mathbf{R}, \mathbf{k}_F, \omega_n) & i\widehat{f}(\mathbf{R}, \mathbf{k}_F, \omega_n) \\ -i\widehat{f}(\mathbf{R}, \mathbf{k}_F, \omega_n) & -\widehat{g}(\mathbf{R}, \mathbf{k}_F, \omega_n) \end{pmatrix}. \quad (2.28)$$

The quasi-classical Green's function satisfies a normalization condition $\widehat{g}^2 = -\pi^2 \widehat{\sigma}_0$.

2.3.1 Eilenberger equation

Using the relation $\widehat{\sigma}_z^2 = \widehat{\sigma}_0$, the Gor'kov equations (2.25) and (2.26) are rewritten as

$$\sum_{\gamma} \int d^3r_3 \left\{ \delta_{\alpha\gamma} \delta(\mathbf{r}_1 - \mathbf{r}_3) \left[i\hbar\omega_n \widehat{\sigma}_z + \left(\frac{\hbar^2 \nabla_3^2}{2m} + \mu \right) \widehat{\sigma}_0 \right] \right. \\ \left. + \begin{pmatrix} -\Sigma_{\alpha\gamma}(\mathbf{r}_1, \mathbf{r}_3) & \Delta_{\alpha\gamma}(\mathbf{r}_1, \mathbf{r}_3) \\ -\Delta_{\gamma\alpha}^*(\mathbf{r}_3, \mathbf{r}_1) & -\Sigma_{\gamma\alpha}(\mathbf{r}_3, \mathbf{r}_1) \end{pmatrix} \right\} \widehat{\sigma}_z \widehat{G}_{\gamma\beta}(\mathbf{r}_3, \mathbf{r}_2, \omega_n) = \hbar \delta_{\alpha\beta} \delta(\mathbf{r}_1 - \mathbf{r}_2) \widehat{\sigma}_0, \quad (2.29)$$

$$\sum_{\gamma} \int d^3r_3 \widehat{\sigma}_z \widehat{G}_{\alpha\gamma}(\mathbf{r}_1, \mathbf{r}_3, \omega_n) \\ \times \left\{ \delta_{\gamma\beta} \delta(\mathbf{r}_3 - \mathbf{r}_2) \left[i\hbar\omega_n \widehat{\sigma}_z + \left(\frac{\hbar^2 \nabla_3^2}{2m} + \mu \right) \widehat{\sigma}_0 \right] + \begin{pmatrix} -\Sigma_{\gamma\beta}(\mathbf{r}_3, \mathbf{r}_2) & \Delta_{\gamma\beta}(\mathbf{r}_3, \mathbf{r}_2) \\ -\Delta_{\beta\gamma}^*(\mathbf{r}_2, \mathbf{r}_3) & -\Sigma_{\beta\gamma}(\mathbf{r}_2, \mathbf{r}_3) \end{pmatrix} \right\} \\ = \hbar \delta_{\alpha\beta} \delta(\mathbf{r}_1 - \mathbf{r}_2) \widehat{\sigma}_0. \quad (2.30)$$

By subtracting eq. (2.30) from eq. (2.29),

$$\frac{\hbar^2}{2m} (\nabla_1^2 - \nabla_2^2) \widehat{\sigma}_z \widehat{G}_{\alpha\beta}(\mathbf{r}_1, \mathbf{r}_2, \omega_n) + \left[i\hbar\omega_n \widehat{\sigma}_z, \widehat{\sigma}_z \widehat{G}_{\alpha\beta}(\mathbf{r}_1, \mathbf{r}_2, \omega_n) \right] \\ + \sum_{\gamma} \int d^3r_3 \left[\begin{pmatrix} -\Sigma_{\alpha\gamma}(\mathbf{r}_1, \mathbf{r}_3) & \Delta_{\alpha\gamma}(\mathbf{r}_1, \mathbf{r}_3) \\ -\Delta_{\gamma\alpha}^*(\mathbf{r}_3, \mathbf{r}_1) & -\Sigma_{\gamma\alpha}(\mathbf{r}_3, \mathbf{r}_1) \end{pmatrix} \widehat{\sigma}_z \widehat{G}_{\gamma\beta}(\mathbf{r}_3, \mathbf{r}_2, \omega_n) \right. \\ \left. - \widehat{\sigma}_z \widehat{G}_{\alpha\gamma}(\mathbf{r}_1, \mathbf{r}_3, \omega_n) \begin{pmatrix} -\Sigma_{\gamma\beta}(\mathbf{r}_3, \mathbf{r}_2) & \Delta_{\gamma\beta}(\mathbf{r}_3, \mathbf{r}_2) \\ -\Delta_{\beta\gamma}^*(\mathbf{r}_2, \mathbf{r}_3) & -\Sigma_{\beta\gamma}(\mathbf{r}_2, \mathbf{r}_3) \end{pmatrix} \right] = 0. \quad (2.31)$$

The derivative operators can be rewritten by the center-of-mass coordinate and relative coordinate: $\nabla_1 = \nabla_R/2 + \nabla_r$ and $\nabla_2 = \nabla_R/2 - \nabla_r$. By the derivations operate the Green's function in the Fourier representation eq. (2.27),

$$\frac{\hbar^2}{2m} (\nabla_1^2 - \nabla_2^2) \hat{\sigma}_z \hat{G}_{\alpha\beta}(\mathbf{r}_1, \mathbf{r}_2, \omega_n) = \int \frac{d^3k}{(2\pi)^3} i\hbar\mathbf{v} \cdot \nabla_R \hat{\sigma}_z \hat{G}_{\alpha\beta}(\mathbf{R}, \mathbf{k}, \omega_n) e^{i\mathbf{k}\cdot\mathbf{r}}, \quad (2.32)$$

where $\mathbf{v} = \hbar\mathbf{k}/m$. Therefore, eq. (2.31) is

$$\begin{aligned} & i\hbar\mathbf{v} \cdot \nabla_R \hat{\sigma}_z \hat{G}_{\alpha\beta}(\mathbf{R}, \mathbf{k}, \omega_n) + \left[i\hbar\omega_n \hat{\sigma}_z, \hat{\sigma}_z \hat{G}_{\alpha\beta}(\mathbf{R}, \mathbf{k}, \omega_n) \right] \\ & + \sum_{\gamma} \left[\begin{pmatrix} -\Sigma_{\alpha\gamma}(\mathbf{R}, \mathbf{k}) & -\Delta_{\alpha\gamma}(\mathbf{R}, \mathbf{k}) \\ \Delta_{\gamma\alpha}^*(\mathbf{R}, \mathbf{k}) & -\Sigma_{\gamma\alpha}(\mathbf{R}, -\mathbf{k}) \end{pmatrix} \hat{\sigma}_z \hat{G}_{\gamma\beta}(\mathbf{R}, \mathbf{k}, \omega_n) \right. \\ & \left. - \hat{\sigma}_z \hat{G}_{\alpha\gamma}(\mathbf{R}, \mathbf{k}, \omega_n) \begin{pmatrix} -\Sigma_{\gamma\beta}(\mathbf{R}, \mathbf{k}) & -\Delta_{\gamma\beta}(\mathbf{R}, \mathbf{k}) \\ \Delta_{\beta\gamma}^*(\mathbf{R}, \mathbf{k}) & -\Sigma_{\beta\gamma}(\mathbf{R}, -\mathbf{k}) \end{pmatrix} \right] = 0. \end{aligned} \quad (2.33)$$

Here, we use the quasi-classical approximation, i.e. the Green's function is integrated by the energy ξ_k and the other relative momentum is replaced by the Fermi momentum \mathbf{k}_F . Then, we obtain the Eilenberger equation with the quasi-classical Green's function [27]:

$$i\hbar\mathbf{v}_F \cdot \nabla_R \hat{g}(\mathbf{R}, \mathbf{k}_F, \omega_n) + \left[i\hbar\omega_n \hat{\sigma}_z - \hat{\Delta}(\mathbf{R}, \mathbf{k}_F) - \hat{\Sigma}(\mathbf{R}, \mathbf{k}_F), \hat{g}(\mathbf{R}, \mathbf{k}_F, \omega_n) \right] = 0, \quad (2.34)$$

where \mathbf{v}_F is the Fermi velocity. The matrices are defined

$$\hat{\Delta}(\mathbf{R}, \mathbf{k}_F) \equiv \begin{pmatrix} 0 & \hat{\Delta}(\mathbf{R}, \mathbf{k}_F) \\ -\hat{\Delta}^\dagger(\mathbf{R}, \mathbf{k}_F) & 0 \end{pmatrix}, \quad \hat{\Sigma}(\mathbf{R}, \mathbf{k}_F) \equiv \begin{pmatrix} \hat{\Sigma}(\mathbf{R}, \mathbf{k}_F) & 0 \\ 0 & \hat{\Sigma}^T(\mathbf{R}, -\mathbf{k}_F) \end{pmatrix}. \quad (2.35)$$

2.3.2 Riccati equations

We solve Eilenberger equation (2.34) by the Riccati method [28, 29]. We introduce projection matrices:

$$\hat{P}_{\pm} \equiv \frac{1}{2} \left(\hat{\sigma}_0 \mp \frac{i}{\pi} \hat{g} \right). \quad (2.36)$$

The matrices satisfy the following relations:

$$\hat{P}_{\pm} \hat{P}_{\pm} = \hat{P}_{\pm}, \quad (2.37)$$

$$\hat{P}_+ \hat{P}_- = \hat{P}_- \hat{P}_+ = 0, \quad (2.38)$$

$$\hat{P}_+ + \hat{P}_- = \hat{\sigma}_0, \quad (2.39)$$

$$\hat{P}_- - \hat{P}_+ = \frac{i}{\pi} \hat{g}. \quad (2.40)$$

The projection matrices satisfy the Eilenberger equation (2.34):

$$i\hbar\mathbf{v}_F \cdot \nabla \hat{P}_{\pm} + \left[i\hbar\omega_n \hat{\sigma}_z - \hat{\Delta} - \hat{\Sigma}, \hat{P}_{\pm} \right] = 0. \quad (2.41)$$

Here, we introduce Riccati amplitude \hat{a} and \hat{b} as

$$\begin{aligned}\hat{P}_+ &= \begin{pmatrix} \hat{\sigma}_0 \\ -i\hat{b} \end{pmatrix} (\hat{\sigma}_0 + \hat{a}\hat{b})^{-1} (\hat{\sigma}_0 \quad i\hat{a}), \\ \hat{P}_- &= \begin{pmatrix} -i\hat{a} \\ \hat{\sigma}_0 \end{pmatrix} (\hat{\sigma}_0 + \hat{b}\hat{a})^{-1} (i\hat{b} \quad \hat{\sigma}_0).\end{aligned}\tag{2.42}$$

The projection matrices satisfy the relations (2.37) and (2.38). By substitution eqs. (2.42) for eq. (2.41), we obtain Riccati equations:

$$\begin{aligned}\hbar\mathbf{v}_F \cdot \nabla_R \hat{a}(\mathbf{R}, \mathbf{k}_F, \omega_n) \\ = \hat{\Delta}(\mathbf{R}, \mathbf{k}_F) - \hat{a}(\mathbf{R}, \mathbf{k}_F, \omega_n) \hat{\Delta}^\dagger(\mathbf{R}, \mathbf{k}_F) \hat{a}(\mathbf{R}, \mathbf{k}_F, \omega_n) - 2\hbar\omega_n \hat{a}(\mathbf{R}, \mathbf{k}_F, \omega_n),\end{aligned}\tag{2.43}$$

$$\begin{aligned}-\hbar\mathbf{v}_F \cdot \nabla_R \hat{b}(\mathbf{R}, \mathbf{k}_F, \omega_n) \\ = \hat{\Delta}^\dagger(\mathbf{R}, \mathbf{k}_F) - \hat{b}(\mathbf{R}, \mathbf{k}_F, \omega_n) \hat{\Delta}(\mathbf{R}, \mathbf{k}_F) \hat{b}(\mathbf{R}, \mathbf{k}_F, \omega_n) - 2\hbar\omega_n \hat{b}(\mathbf{R}, \mathbf{k}_F, \omega_n).\end{aligned}\tag{2.44}$$

The equations are solved by integration toward \mathbf{k}_F for $\hat{a}(\mathbf{R}, \mathbf{k}_F, \omega_n)$ and toward $-\mathbf{k}_F$ for $\hat{b}(\mathbf{R}, \mathbf{k}_F, \omega_n)$. From the relations (2.39) and (2.40), the quasi-classical Green's function is given as

$$\hat{g} = -i\pi \begin{pmatrix} (\hat{\sigma}_0 + \hat{a}\hat{b})^{-1} & 0 \\ 0 & (\hat{\sigma}_0 + \hat{b}\hat{a})^{-1} \end{pmatrix} \begin{pmatrix} \hat{\sigma}_0 - \hat{a}\hat{b} & 2i\hat{a} \\ -2i\hat{b} & -(\hat{\sigma}_0 - \hat{b}\hat{a}) \end{pmatrix}.\tag{2.45}$$

2.4 Ginzburg-Landau theory

Since the OP is small in the vicinity of the superfluid transition temperature, difference of the free energy between the superfluid state F_S and normal state F_N can be expanded by the OP. The difference of the free energy is

$$\begin{aligned}F_S - F_N &= \int d^3R \left\langle \alpha \text{Tr} \left[\hat{\Delta}^\dagger(\mathbf{R}, \mathbf{k}_F) \hat{\Delta}(\mathbf{R}, \mathbf{k}_F) \right] \right. \\ &\quad + \beta \text{Tr} \left[\hat{\Delta}^\dagger(\mathbf{R}, \mathbf{k}_F) \hat{\Delta}(\mathbf{R}, \mathbf{k}_F) \hat{\Delta}^\dagger(\mathbf{R}, \mathbf{k}_F) \hat{\Delta}(\mathbf{R}, \mathbf{k}_F) \right] \\ &\quad + K \text{Tr} \left[\left\{ \mathbf{k}_F \cdot \nabla_R \hat{\Delta}^\dagger(\mathbf{R}, \mathbf{k}_F) \right\} \left\{ \mathbf{k}_F \cdot \nabla_R \hat{\Delta}(\mathbf{R}, \mathbf{k}_F) \right\} \right] \\ &\quad \left. + \text{Tr} \left[\hat{\Delta}^\dagger(\mathbf{R}, \mathbf{k}_F) \hat{V}(\mathbf{R}, \mathbf{k}_F) \hat{\Delta}(\mathbf{R}, \mathbf{k}_F) \right] \right\rangle_{\mathbf{k}_F} \\ &\equiv \int d^3R \left\langle f(\mathbf{R}, \mathbf{k}_F) + \text{Tr} \left[\hat{\Delta}^\dagger(\mathbf{R}, \mathbf{k}_F) \hat{V}(\mathbf{R}, \mathbf{k}_F) \hat{\Delta}(\mathbf{R}, \mathbf{k}_F) \right] \right\rangle_{\mathbf{k}_F},\end{aligned}\tag{2.46}$$

where $\hat{V}(\mathbf{R}, \mathbf{k}_F)$ is external potential. This Ginzburg-Landau (GL) theory is valid in $T_c - T \ll T_c$, where T_c is the transition temperature. The GL free energy functional $f(\mathbf{R}, \mathbf{k}_F)$ has the gauge symmetry and rotational symmetry in the momentum space and spin space. Since $\text{Tr}[\dots]$ in GL free energy functional is positive, signs of the coefficients α , β , and K are fixed. The coefficient α for the quadratic term of the OP changes a sign at the transition temperature, namely, $\alpha > 0$ in $T > T_c$ and $\alpha < 0$ in $T < T_c$, according to $\alpha \propto T - T_c$. Therefore, the OP is finite below T_c and vanishes above T_c . The quartic coefficient β is

positive so that the finite OP gives the free energy minimum. The coefficient K for the gradient term is also positive so that the stationary OP gives the free energy minimum.

The OP for the l -wave paring state can be expanded as

$$\hat{\Delta}(\mathbf{r}, \mathbf{k}) = i\hat{\sigma}_y A_{ij\dots l}(\mathbf{r})k_i k_j \cdots k_l, \quad (2.47)$$

for the spin-singlet state, and

$$\hat{\Delta}(\mathbf{r}, \mathbf{k}) = i\hat{\sigma}_\mu \hat{\sigma}_y A_{\mu ij\dots l}(\mathbf{r})k_i k_j \cdots k_l, \quad (2.48)$$

for the spin-triplet state, where repeated indexes implies summation over x , y , and z . A is rank- l totally symmetric traceless tensor in the orbital space for the spin-singlet state [30, 31], and direct product of the tensor in the orbital space and rank-1 tensor in the spin space for the spin-triplet state. Using features of the tensor A , the quadratic term in GL free energy functional can be expanded into one term with A . The quartic term can be expanded into $l + 1$ terms for the spin-singlet state and $3l + 2$ terms for the spin-triplet state [32]. The gradient term can be expanded into three terms except for the s -wave paring state [33].

In this section, GL free energy functional is mentioned from symmetric consideration; however, that is obtained from microscopic theory.

Chapter 3

Multi-component neutral Fermi superfluids

The order parameter (OP) of the superfluid state for the s -wave pairing state is

$$\Delta_{\uparrow\downarrow}(\mathbf{r}) = -\Delta_{\downarrow\uparrow}(\mathbf{r}) = \Delta(\mathbf{r}), \quad (3.1)$$

for the p -wave is

$$\hat{\Delta}(\mathbf{r}, \mathbf{k}) = \sum_{\mu i} i\hat{\sigma}_\mu \hat{\sigma}_y A_{\mu i}(\mathbf{r}) k_i, \quad (3.2)$$

and for the d -wave is

$$\Delta_{\uparrow\downarrow}(\mathbf{r}, \mathbf{k}) = -\Delta_{\downarrow\uparrow}(\mathbf{r}, \mathbf{k}) = \sum_{ij} B_{ij}(\mathbf{r}) k_i k_j, \quad (3.3)$$

where $A_{\mu i}$ is rank-2 tensor [2] and B_{ij} is rank-2 symmetric traceless tensor [30]. The superfluids with non-zero angular momentum are so-called multi-component superfluids. In this thesis, we discuss the spin-triplet p -wave superfluid, i.e. the superfluid ${}^3\text{He}$, and the spinless p -wave superfluid of Fermi atomic gases.

3.1 Superfluid ${}^3\text{He}$

The superfluid ${}^3\text{He}$ consists of spin-triplet p -wave Cooper pairs, which is no doubt on its identification [34]. There are three stable phases, A-, B-, and A_1 -phases, for the superfluid ${}^3\text{He}$ in a bulk (Fig. 3.1 [35]). The A-phase is stabilized in a narrow region at high temperature and high pressure without a magnetic field, while the B-phase is stabilized in another wide region within the superfluid phase. Under a magnetic field, the region of the A-phase becomes wide and that of the B-phase becomes narrow. Moreover, the A_1 -phase appears near the transition temperature of the superfluid phase.

The superfluid ${}^3\text{He}$ in the A-phase is in the Anderson-Brinkman-Morel (ABM) state [36, 37]. The ABM state has the orbital angular momentum $L_z = 1$ and the spin angular momentum $S_z = 0$. The OP in the ABM state is described by

$$A_{\mu i} = \Delta_A \hat{d}_\mu (\hat{\mathbf{m}} + i\hat{\mathbf{n}})_i, \quad (3.4)$$

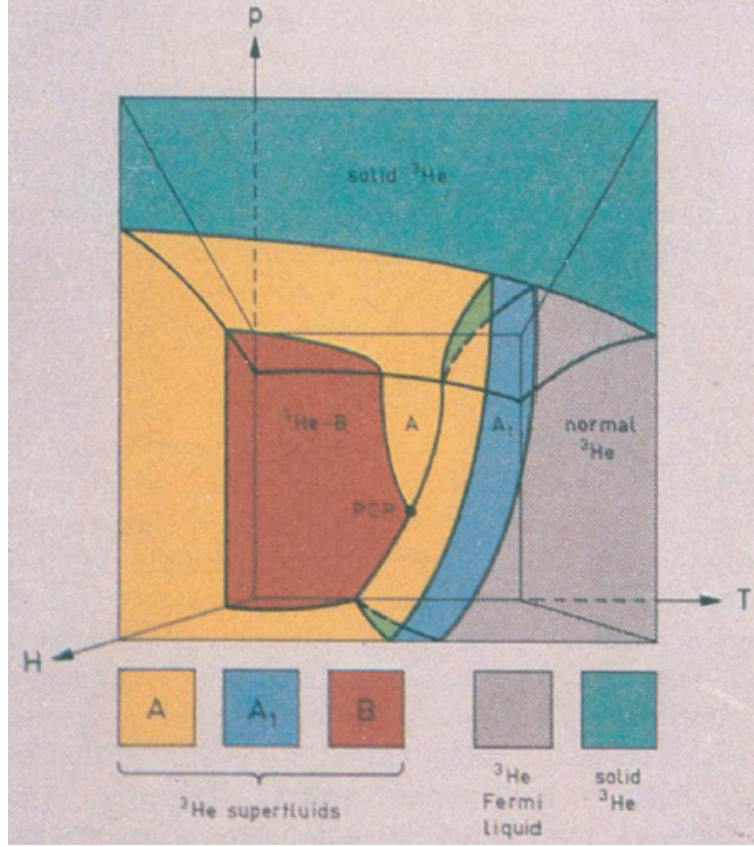


Figure 3.1: Taken from Salomaa and Volovik [35]. Phase diagram of the superfluid ${}^3\text{He}$ with temperature, pressure, and magnetic field. A region of the A-phase becomes wide and that of the B-phase becomes narrow under a magnetic field. The A_1 -phase also appears under a magnetic field.

where Δ_A is amplitude of the OP toward the antinode direction. $\hat{\mathbf{m}}$ and $\hat{\mathbf{n}}$ are orthogonal, and l -vector ($\hat{\mathbf{l}}$) is defined by them as

$$\hat{\mathbf{l}} \equiv \hat{\mathbf{m}} \times \hat{\mathbf{n}}. \quad (3.5)$$

l -vector signifies the direction of the orbital angular momentum, or orbital chirality, and points to a point node (Fig. 3.2). d -vector ($\hat{\mathbf{d}}$) is perpendicular to the spin \mathbf{S} of a Cooper pair, namely, $\hat{\mathbf{d}} \cdot \mathbf{S} = 0$.

The superfluid ${}^3\text{He}$ in the B-phase is in the Balian-Werthamer (BW) state [38]. The BW state has the total angular momentum $\mathbf{J} = \mathbf{L} + \mathbf{S} = \mathbf{0}$. The OP in the BW state is described by

$$A_{\mu i} = \Delta_B R_{\mu i}(\hat{\mathbf{n}}, \theta), \quad (3.6)$$

where $R_{\mu i}(\hat{\mathbf{n}}, \theta)$ is a rotation matrix with a rotation axis $\hat{\mathbf{n}}$ and a rotation angle θ about $\hat{\mathbf{n}}$. The rotation matrix gives the relative angle between the orbital momentum and d -vector. The BW state has an isotropic full gap with amplitude Δ_B .

The superfluid ${}^3\text{He}$ in the A_1 -phase is in the spin polarized state by a magnetic field. The orbital state is the same as that in the ABM state.

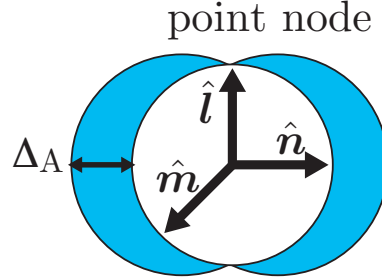


Figure 3.2: Relation between l -vector and a point node of the OP in the ABM state, where Δ_A is amplitude of the OP toward the antinode direction.

3.1.1 Texture

Spatial structure of the OP, namely texture, is fully characterized by l -vector and d -vector for the A-phase, and n -vector and θ -angle for the B-phase. The texture is constructed by vortices or boundary conditions in the restricted geometry, such as cylindrical geometry or slab (parallel plate) geometry.

For the A-phase, l -vector must be perpendicular to the boundary of the geometry to prevent motion of Cooper pairs toward the boundary. In other words, a point node is touched to the boundary to minimize loss of the condensation energy at the boundary. Relation between l -vector and d -vector is fixed by dipole-dipole interaction. The dipole-dipole interaction works l -vector and d -vector into parallel, where the characteristic length of spatial variation is the dipole coherence length $\xi_d \sim 10 \mu\text{m}$. Under a magnetic field, d -vector tends to be perpendicular to the magnetic field. The interaction by a magnetic field and the dipole-dipole interaction are comparable under a magnetic field $\sim 2 \text{ mT}$.

For the B-phase, n -vector is perpendicular to the boundary of the geometry and θ -angle is fixed to Leggett angle, namely $\theta = \theta_L \equiv \cos^{-1}(-1/4) \approx 104^\circ$, by dipole-dipole interaction in the absence of a magnetic field. Under a magnetic field, the OP amplitude toward the magnetic field is suppressed. In this situation, n -vector is parallel to a magnetic field and θ -angle is fixed to

$$\theta = \cos^{-1} \left(-\frac{1}{4} \frac{\Delta_{\parallel}}{\Delta_{\perp}} \right), \quad (3.7)$$

where Δ_{\parallel} and Δ_{\perp} are parallel and perpendicular components of the OP amplitude for the magnetic field, respectively. The parallel component Δ_{\parallel} is suppressed by a magnetic field. If Δ_{\parallel} vanishes by a high magnetic field, the superfluid ^3He is in the planar state.

3.1.2 Half-quantum vortex

When the superfluid ^3He A-phase is confined in slab geometry with a magnetic field $\gtrsim 2 \text{ mT}$ perpendicular to the slab, l -vector is perpendicular to the slab and d -vector is parallel to the slab. In this situation, it is possible to form half-quantum vortices (HQVs) [39, 40]. The HQV has a phase winding number $1/2$, namely the phase of the OP changes from 0 to π , with π -rotation of d -vector around the vortex core (Fig. 3.3).

The OP for the A-phase in the slab geometry on the x - y plane with a high magnetic field

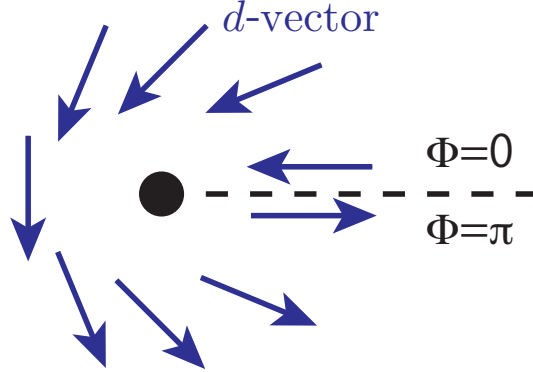


Figure 3.3: Variation of the OP around a HQV core. The phase of the OP changes from 0 to π and d -vector rotates π .

toward the z -axis is described by

$$\hat{\Delta}(\mathbf{r}, \mathbf{k}) = \begin{pmatrix} \Delta_A(r)e^{i\Phi}\hat{d}_{\uparrow\uparrow}(\mathbf{r}) (\hat{k}_x + i\hat{k}_y) & 0 \\ 0 & \Delta_A(r)e^{i\Phi}\hat{d}_{\downarrow\downarrow}(\mathbf{r}) (\hat{k}_x + i\hat{k}_y) \end{pmatrix}, \quad (3.8)$$

where $\hat{d}_{\uparrow\uparrow} = -\hat{d}_x(\mathbf{r}) + i\hat{d}_y(\mathbf{r})$, $\hat{d}_{\downarrow\downarrow} = \hat{d}_x(\mathbf{r}) + i\hat{d}_y(\mathbf{r})$, and Φ is the phase of the OP. The OP of the HQV can be described by $\Phi = \theta/2$ and $\hat{\mathbf{d}} = \hat{\mathbf{x}} \cos(\theta/2) - \hat{\mathbf{y}} \sin(\theta/2)$ in Eq. (3.8) with the polar coordinates (r, θ) . Then, the OP is written as

$$\Delta_{\uparrow\uparrow}(\mathbf{r}, \mathbf{k}) = -\Delta_A(r)e^{i\theta} (\hat{k}_x + i\hat{k}_y), \quad \Delta_{\downarrow\downarrow}(\mathbf{r}, \mathbf{k}) = \Delta_A(r) (\hat{k}_x + i\hat{k}_y). \quad (3.9)$$

Therefore, HQV can be regarded as that a spin polarized state has a phase winding number 1 [41, 42, 43].

Although the exotic HQV has been investigated, obvious evidence of the HQV has not been observed yet [44]. That remains as an important problem for the superfluid ^3He .

3.2 Fermi atomic gases

In 1995, Bose-Einstein condensates (BECs) were realized in trapped Bose atomic gases of ^{87}Rb [5], ^{23}Na [6], and ^7Li [7]. Atomic gases are trapped and cooled to very low temperature, typically ~ 100 nK, using techniques, such as magnetic or optical trap, laser cooling, evaporative cooling, etc. In ultracold atomic gases, almost atoms are in the condensed state. That is different from the superfluid ^4He , where the density of particles in the condensate is only about 10% or less of the total density.

In related development, the superfluids of trapped Fermi atomic gases were also realized. The superfluids are BECs by molecules of the Fermi atoms [8, 9, 10] or Bardeen-Cooper-Schrieffer (BCS) superfluids by Cooper pairs of the Fermi atoms [11, 12]. The transition temperature of the BCS superfluid is $T_c \sim 0.1T_F$, where T_F is the Fermi temperature. It is higher than conventional superconductors, the superfluid ^3He , in which $\sim 10^{-3}T_F$, and even high- T_c superconductors, in which $\sim 10^{-2}T_F$. Note that a typical value of the Fermi temperature for Fermi atomic gases is sub- μK .

Another superfluid with multi-component OP is a spinor BEC [45, 46, 47, 48] in ultracold Bose atomic gases with ^{23}Na or ^{87}Rb . Spinor BECs have internal degrees of freedom, namely hyperfine spin, which appears as coupling of nuclear spin and electronic spin. Such system can be realized under optical traps; otherwise the hyperfine spin is polarized under magnetic traps. The OP is composed of $2F + 1$ -component spinor owing to the hyperfine spin F .

3.2.1 Feshbach resonance

A great advantage of the atomic gases is that interparticle interaction, or scattering length, can be tuned efficiently by Feshbach resonance. We explain the mechanism of the Feshbach resonance according to Ref. [4].

Feshbach resonance appears when total energy in an open channel matches the energy of a bound state in a closed channel. Two particles in an initial open channel can be scattered to an intermediate state in a closed channel, which subsequently decays to two particles in an open channel. From perturbation theory, we can expect that scattering length a has the form of a sum of terms of the type

$$a = \sum_E \frac{C}{E - E_{\text{res}}}, \quad (3.10)$$

where E is energy of the particles in the open channel, E_{res} is the energy of a state in the closed channels, and C is a positive constant. Consequently, there will be large effects if the energy E of the two particles in the entrance channel is close to the energy of a bound state in a closed channel. As we would expect from second-order perturbation theory for energy shifts, coupling between channels gives rise to a repulsive interaction if the energy of the scattering particles is greater than that of the bound state, and an attractive one if it is less. The closer the energy of the bound state is to the energy of the incoming particles in the open channels, the larger the effect on the scattering. Then, energy summation of the right hand side of eq. (3.10) is

$$a = a_{\text{nr}} + \frac{C}{E_{\text{th}} - E_{\text{res}}}, \quad (3.11)$$

where a_{nr} is a non-resonant scattering length and $E_{\text{th}} = \epsilon_\alpha + \epsilon_\beta$ is a threshold energy of resonant open channels with internal energy ϵ_α and ϵ_β of atoms in the channels α and β , respectively.

Since the energies of states depend on external parameters, such as the magnetic field, these resonances make it possible to tune the effective interaction between atoms. We imagine that the energy denominator in the second term of eq. (3.11) vanishes for a particular value of the magnetic field, $B = B_0$. Expanding the energy denominator about this value of the magnetic field, we find

$$E_{\text{th}} - E_{\text{res}} \approx (\mu_{\text{res}} - \mu_\alpha - \mu_\beta)(B - B_0), \quad (3.12)$$

where $\mu_\alpha = -\partial\epsilon_\alpha/\partial B$ and $\mu_\beta = -\partial\epsilon_\beta/\partial B$ are the magnetic moments of the two atoms in the open channel, and $\mu_{\text{res}} = -\partial E_{\text{res}}/\partial B$ is the magnetic moment of the molecular bound state. The scattering length is therefore given by

$$a = a_{\text{nr}} \left(1 - \frac{\Delta B}{B - B_0} \right), \quad (3.13)$$

where ΔB is the width parameter of the resonance. A typical experimental result is shown in Fig. 3.4 [49].

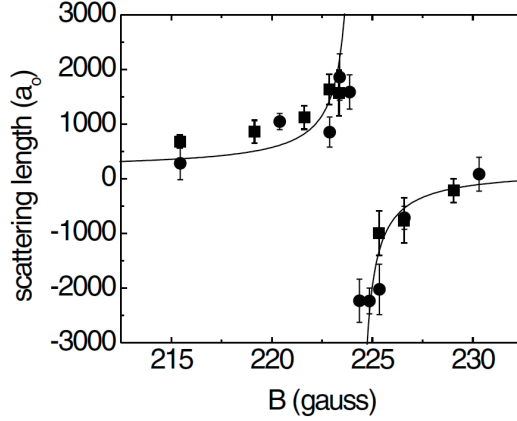


Figure 3.4: Taken from Regal and Jin [49]. Scattering length versus magnetic field near the peak of Feshbach resonance for ^{40}K . Amplitude of scattering length varies according to $(B - B_0)^{-1}$ and the sign of it changes at B_0 .

3.2.2 p -wave resonant Fermi atomic gases

By using magnetic Feshbach resonance, when p -wave interaction in a closed channel can be enhanced, we expect BCS superfluids by p -wave interactive Cooper pairs. In fact, there are vigorous activities toward realizing p -wave resonant superfluids in ^6Li [13, 14, 15] and ^{40}K [16, 17, 18] recently. p -wave Feshbach resonance occurs at a different magnetic field in each hyperfine spin state of atoms, shown in Fig. 3.5 [13]. Since the spin state of superfluidity is fixed by the external magnetic field, the spin degrees of freedom are frozen, and hence only the orbital degrees of freedom are active. Here, the OP is characterized only by A_i , described as

$$\Delta(\mathbf{r}, \mathbf{k}) = \sum_i A_i(\mathbf{r}) k_i. \quad (3.14)$$

In a sense, the p -wave resonant superfluid is analogous to the “spinless” superfluid ^3He A-phase.

Symmetry of the orbital state of superfluidity is broken by dipole-dipole interaction. The dipole-dipole interaction between two alkaline atoms has the form

$$H_{ss} = -\alpha^2 \frac{3(\hat{\mathbf{R}} \cdot \hat{\mathbf{s}}_1)(\hat{\mathbf{R}} \cdot \hat{\mathbf{s}}_2) - \hat{\mathbf{s}}_1 \cdot \hat{\mathbf{s}}_2}{R^3}, \quad (3.15)$$

where α is the fine structure constant, $\hat{\mathbf{s}}_i$ is the spin of the valence electron on an alkaline atom i , R is the interatomic separation, and $\hat{\mathbf{R}}$ is the unit vector defining the interatomic axis. When two dipoles are aligned head to tail they are in an attractive configuration, corresponding to $\hat{\mathbf{R}} \cdot \hat{\mathbf{s}}_i = 1$. In contrast, when the dipoles are side by side they are in a repulsive configuration, corresponding to $\hat{\mathbf{R}} \cdot \hat{\mathbf{s}}_i = 0$. Then, the dipole-dipole interaction acts to split the relative orbital state of two particles, depending on the projections of the orbital angular momentum, either $m_l = \pm 1$ or $m_l = 0$, shown in Fig 3.6 [17]. This results in breaking of the degeneracy between

$$\hat{k}_{\pm} = \mp \frac{1}{\sqrt{2}}(\hat{k}_x \pm i\hat{k}_y) \quad \text{and} \quad \hat{k}_0 = \hat{k}_z. \quad (3.16)$$

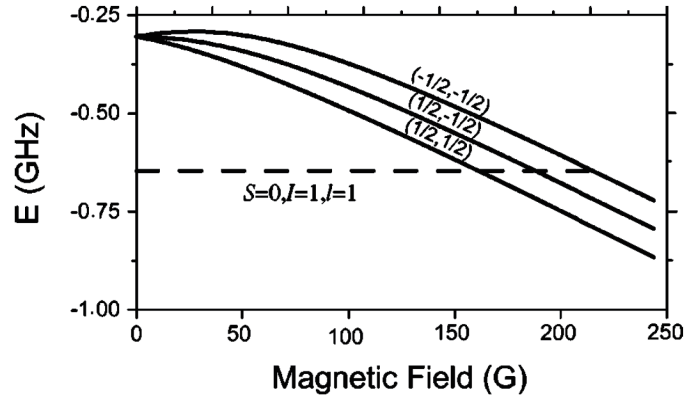


Figure 3.5: Taken from Zhang *et al.* [13]. Solid line: Threshold energy E_{th} for the combination of the projections of the hyperfine spin state for incident atoms as $(m_{f1}, m_{f2}) = (-1/2, -1/2)$, $(1/2, -1/2)$, and $(1/2, 1/2)$. Dashed line: Resonant energy E_{res} for a closed channel with p -wave ($l = 1$) interaction. Feshbach resonance occurs at magnetic fields where the solid line intersects with the dashed line.

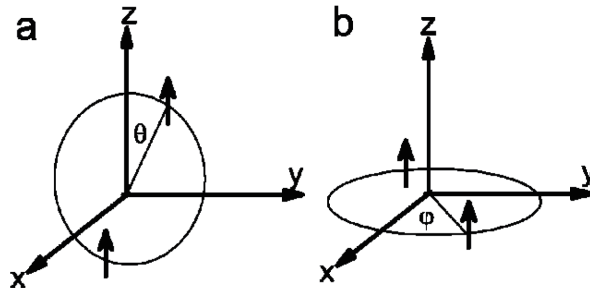


Figure 3.6: Taken from Ticknor *et al.* [17]. Schematic representation of classical dipoles interacting in different circular orbit. (a) An orbit with $m_l = 0$. The dipole-dipole interaction changes between attraction and repulsion. (b) An orbit with $m_l = \pm 1$. The dipole-dipole interaction always repels one another.

This split was estimated to be large for ^{40}K by Cheng and Yip [50, 51] from the clear difference in magnetic fields when Feshbach resonance occurs (splitting field is 0.47 ± 0.08 G [17]). For ^6Li , the split may be small, because an experiment conducted in a magnetic field of $H = 158.5(7)$ G shows no clear resonance splitting [15].

A critical difference between the superfluid ^3He and the p -wave resonant superfluid of atomic gases lies in the boundary conditions. In the superfluid ^3He A-phase, l -vector is always perpendicular to the boundary to minimize loss of the condensation energy at the boundary. On the other hand, since atomic gases are confined in a three-dimensional harmonic trap potential, where density of the condensation energy gradually decreases toward the outer region, l -vector tends to align parallel to the circumference [24, 25]. This orientation is advantageous because the condensation energy is maximally gained by allowing the point nodes to move out from the inner region. Moreover, shapes of the trap potential is easily controlled, such as cigar and pancake shapes. Textures for the p -wave resonant superfluid of atomic gases are discussed in Cap. 7.

Chapter 4

Majorana excitations

Recently, Majorana quasi-particles (QPs) and Majorana fermions have attracted much attention in the condensed matter physics [3] and for the application to topological quantum computations [52]. The Majorana QP and Majorana fermionic operator are defined by $\gamma^\dagger = \gamma$ and $\Psi^\dagger = \Psi$, respectively, which imply that the particle and antiparticle are identical. It has been proposed that the Majorana QPs bring non-Abelian statistics of vortices in chiral superfluids [41].

Candidate systems that exist the Majorana excitations are quite rare, e.g. spin-triplet superconductors or superfluids, fractional quantum Hall systems with the 5/2 filling [53, 54], interfaces between a topological insulator and an s -wave superconductor [55], and s -wave superfluids with particular spin-orbit interactions [56]. Majorana excitations appear at a vortex or a surface, where QPs have the Andreev bound states. In this chapter, we introduce the Majorana excitations, namely $\gamma^\dagger = \gamma$ in a vortex and $\Psi^\dagger = \Psi$ at a surface, for spin-triplet superconductors or superfluids.

4.1 Majorana quasi-particle in vortex

If the self-energy in eq. (2.17) satisfies $\hat{\Sigma}^\dagger(\mathbf{r}_2, \mathbf{r}_1) = \hat{\Sigma}(\mathbf{r}_1, \mathbf{r}_2)$, the following part of the Bogoliubov-de Gennes (BdG) equation has the symmetry:

$$-\hat{\sigma}_x \left[\hat{K}(\mathbf{r}_1, \mathbf{r}_2) + \hat{\Delta}(\mathbf{r}_1, \mathbf{r}_2) \right]^* \hat{\sigma}_x = \left[\hat{K}(\mathbf{r}_1, \mathbf{r}_2) + \hat{\Delta}(\mathbf{r}_1, \mathbf{r}_2) \right]. \quad (4.1)$$

By using the symmetry, the matrix $\hat{u}_\nu(\mathbf{r})$ is

$$\hat{u}_\nu(\mathbf{r}) = \begin{pmatrix} \hat{u}_\nu(\mathbf{r}) & \hat{v}_\nu^*(\mathbf{r}) \\ \hat{v}_\nu(\mathbf{r}) & \hat{u}_\nu^*(\mathbf{r}) \end{pmatrix}. \quad (4.2)$$

Then, the BdG equation (2.17) can be reduced as

$$\int d^3r_2 \left[\hat{K}(\mathbf{r}_1, \mathbf{r}_2) + \hat{\Delta}(\mathbf{r}_1, \mathbf{r}_2) \right] \begin{pmatrix} \hat{u}_\nu(\mathbf{r}_2) \\ \hat{v}_\nu(\mathbf{r}_2) \end{pmatrix} = \begin{pmatrix} \hat{u}_\nu(\mathbf{r}_1) \\ \hat{v}_\nu(\mathbf{r}_1) \end{pmatrix} \hat{E}_\nu, \quad (4.3)$$

where $\hat{E}_\nu \equiv \text{diag}[E_{\nu,\uparrow}, E_{\nu,\downarrow}]$. If we consider the energy for a spin, eq. (4.3) can be reduced as

$$\int d^3r_2 \left[\hat{K}(\mathbf{r}_1, \mathbf{r}_2) + \hat{\Delta}(\mathbf{r}_1, \mathbf{r}_2) \right] \varphi_\nu(\mathbf{r}_2) = E_\nu \varphi_\nu(\mathbf{r}_1), \quad (4.4)$$

where $\varphi_\nu \equiv [u_{\nu,1}, u_{\nu,2}, v_{\nu,1}, v_{\nu,2}]^T$. By using the symmetry of eq. (4.1), BdG equation is derived another form:

$$\int d^3r_2 \left[\widehat{K}(\mathbf{r}_1, \mathbf{r}_2) + \widehat{\Delta}(\mathbf{r}_1, \mathbf{r}_2) \right] \widehat{\sigma}_x \varphi_\nu^*(\mathbf{r}_2) = -E_\nu \widehat{\sigma}_x \varphi_\nu^*(\mathbf{r}_1). \quad (4.5)$$

By comparing eqs. (4.4) and (4.5), we have one-to-one mapping between positive energy states φ_E and negative energy states $\varphi_{-E} = \widehat{\sigma}_x \varphi_E^*$. Bogoliubov QP operators are derived by eqs. (2.12) and (2.14):

$$\begin{aligned} \gamma_E &= \int d^3r \varphi_E^\dagger(\mathbf{r}) \Psi(\mathbf{r}) \\ &= \int d^3r \left[u_{E,1}^*(\mathbf{r}) \psi_\uparrow(\mathbf{r}) + u_{E,2}^*(\mathbf{r}) \psi_\downarrow(\mathbf{r}) + v_{E,1}^*(\mathbf{r}) \psi_\uparrow^\dagger(\mathbf{r}) + v_{E,2}^*(\mathbf{r}) \psi_\downarrow^\dagger(\mathbf{r}) \right], \end{aligned} \quad (4.6)$$

$$\begin{aligned} \gamma_{-E} &= \int d^3r \varphi_{-E}^\dagger(\mathbf{r}) \Psi(\mathbf{r}) = \int d^3r [\widehat{\sigma}_x \varphi_E^*(\mathbf{r})]^\dagger \Psi(\mathbf{r}) \\ &= \int d^3r \left[v_{E,1}(\mathbf{r}) \psi_\uparrow(\mathbf{r}) + v_{E,2}(\mathbf{r}) \psi_\downarrow(\mathbf{r}) + u_{E,1}(\mathbf{r}) \psi_\uparrow^\dagger(\mathbf{r}) + u_{E,2}(\mathbf{r}) \psi_\downarrow^\dagger(\mathbf{r}) \right]. \end{aligned} \quad (4.7)$$

Therefore, we lead to the relation of the Bogoliubov QP operators $\gamma_E = \gamma_{-E}^\dagger$. The Bogoliubov QP with the zero energy is the Majorana QP, $\gamma_0^\dagger = \gamma_0$.

Chiral p -wave superfluids have nontrivial Caroli-de Gennes-Matricon (CdGM) states [57] at a vortex. It is possible for the CdGM states to have exact zero energy states [58, 59, 60, 61, 54]. We demonstrate it according to Ref. [60]. From now on, we disregard the self-energy. Then, the BdG equation (4.4) is

$$\int d^3r_2 \begin{pmatrix} \delta(\mathbf{r}_1 - \mathbf{r}_2) \left[-\frac{\hbar^2 \nabla^2}{2m} - \mu \right] \widehat{\sigma}_0 & \widehat{\Delta}(\mathbf{r}_1, \mathbf{r}_2) \\ \widehat{\Delta}^\dagger(\mathbf{r}_2, \mathbf{r}_1) & -\delta(\mathbf{r}_1 - \mathbf{r}_2) \left[-\frac{\hbar^2 \nabla^2}{2m} - \mu \right] \widehat{\sigma}_0 \end{pmatrix} \varphi_\nu(\mathbf{r}_2) = E_\nu \varphi_\nu(\mathbf{r}_1). \quad (4.8)$$

By the Fourier transformation,

$$\begin{pmatrix} \left[-\frac{\hbar^2 \nabla^2}{2m} - \mu \right] \widehat{\sigma}_0 & \widehat{\Delta}(\mathbf{r}, \mathbf{k}) \\ \widehat{\Delta}^\dagger(\mathbf{r}, \mathbf{k}) & -\left[-\frac{\hbar^2 \nabla^2}{2m} - \mu \right] \widehat{\sigma}_0 \end{pmatrix} \varphi_{\nu, \mathbf{k}}(\mathbf{r}) = E_{\nu, \mathbf{k}} \varphi_{\nu, \mathbf{k}}(\mathbf{r}). \quad (4.9)$$

In weak-coupling case $\Delta \ll E_F$, since we can use quasi-classical approximation,

$$\begin{pmatrix} -i\hbar \mathbf{v}_F \cdot \nabla \widehat{\sigma}_0 & \widehat{\Delta}(\mathbf{r}, \mathbf{k}) \\ \widehat{\Delta}^\dagger(\mathbf{r}, \mathbf{k}) & i\hbar \mathbf{v}_F \cdot \nabla \widehat{\sigma}_0 \end{pmatrix} \tilde{\varphi}_{\nu, \mathbf{k}}(\mathbf{r}) = E_{\nu, \mathbf{k}} \tilde{\varphi}_{\nu, \mathbf{k}}(\mathbf{r}), \quad (4.10)$$

where $\varphi_{\nu, \mathbf{k}}(\mathbf{r}) = \tilde{\varphi}_{\nu, \mathbf{k}}(\mathbf{r}) e^{i\mathbf{k} \cdot \mathbf{r}}$.

Since many properties of the low energy excitation modes do not depend on the exact structure of the OP and vortex core, we consider for simplicity the following pairing states. For spin-singlet pairing,

$$\widehat{\Delta}(\mathbf{r}, \mathbf{k}) = i\widehat{\sigma}_y \Delta(\mathbf{r}) (k_x + ik_y)^N k_z^{l-N}, \quad (l : \text{even}), \quad (4.11)$$

and for spin-triplet pairing,

$$\widehat{\Delta}(\mathbf{r}, \mathbf{k}) = i\widehat{\sigma}_z \widehat{\sigma}_y \Delta(\mathbf{r}) (k_x + ik_y)^N k_z^{l-N}, \quad (l : \text{odd}), \quad (4.12)$$

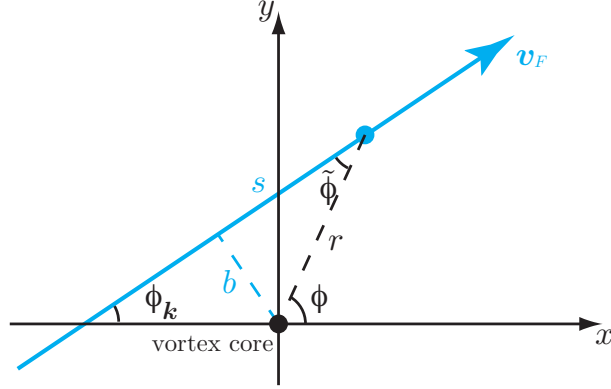


Figure 4.1: Coordinate along the trajectory $s = r \cos \tilde{\phi}$ and the impact parameter $b = r \sin \tilde{\phi}$.

where l is the projection of the orbital angular momentum of the Cooper pair along the z -axis and $0 \leq N \leq l$ is integer. The chiral superfluids are characterized by the nonzero value of the index N . We consider the vortex state as the OP

$$\Delta(\mathbf{r}) = \Delta(r)e^{im\phi}, \quad (4.13)$$

where we take a cylindrical coordinate $\mathbf{r} = (r, \phi, z)$ and m is integer. We omit the spin states, since they are not important for the low energy excitation modes. Then, eq. (4.10) can be reduced as

$$\begin{pmatrix} -i\hbar\mathbf{v}_F \cdot \nabla & \Delta(r)e^{i(N\phi_{\mathbf{k}}+m\phi)} \\ \Delta(r)e^{-i(N\phi_{\mathbf{k}}+m\phi)} & i\hbar\mathbf{v}_F \cdot \nabla \end{pmatrix} \Phi_{\nu, \mathbf{k}}(\mathbf{r}) = E_{\nu, \mathbf{k}} \Phi_{\nu, \mathbf{k}}(\mathbf{r}), \quad (4.14)$$

where $k_x = \cos \phi_{\mathbf{k}}$ and $k_y = \sin \phi_{\mathbf{k}}$.

Since the spatial derivative is along the trajectory, it is convenient to choose the following coordinate: the coordinate consists of $s = r \cos(\phi - \phi_{\mathbf{k}})$ along the trajectory and the impact parameter $b = r \sin(\phi - \phi_{\mathbf{k}})$, shown in Fig. 4.1. In this coordinate, eq. (4.14) is

$$\begin{pmatrix} -i\hbar v_F \partial_s & \Delta(\sqrt{s^2 + b^2})e^{i[m\tilde{\phi} + (m+N)\phi_{\mathbf{k}}]} \\ \Delta(\sqrt{s^2 + b^2})e^{-i[m\tilde{\phi} + (m+N)\phi_{\mathbf{k}}]} & i\hbar v_F \partial_s \end{pmatrix} \Phi_{\nu, \mathbf{k}}(s, b) = E_{\nu, \mathbf{k}} \Phi_{\nu, \mathbf{k}}(s, b), \quad (4.15)$$

where $\tilde{\phi} \equiv \phi - \phi_{\mathbf{k}}$ and $\tan \tilde{\phi} = b/s$.

The state with the lowest energy corresponds to trajectories which cross the center of the vortex, namely $b = 0$. Along this trajectory, $\sin \tilde{\phi} = 0$ and $\cos \tilde{\phi} = \text{sign}(s)$, where $\text{sign}(x) \equiv x/|x|$. For odd integer m , eq. (4.15) is

$$\begin{pmatrix} -i\hbar v_F \partial_s & \Delta(|s|)\text{sign}(s)e^{i(m+N)\phi_{\mathbf{k}}} \\ \Delta(|s|)\text{sign}(s)e^{-i(m+N)\phi_{\mathbf{k}}} & i\hbar v_F \partial_s \end{pmatrix} \Phi_{\nu, \mathbf{k}}(s, b=0) = E_{\nu, \mathbf{k}} \Phi_{\nu, \mathbf{k}}(s, b=0). \quad (4.16)$$

The eigenfunction of eq. (4.16) is

$$\Phi_{\nu, \mathbf{k}}(s, b=0) \propto e^{i(m+N)\frac{\phi_{\mathbf{k}}}{2}\hat{\sigma}_z} \begin{pmatrix} 1 \\ -i \end{pmatrix} \Phi_0(s), \quad (4.17)$$

with the zero energy, where

$$\Phi_0(s) \equiv \exp \left[- \int^s ds' \text{sign}(s') \frac{\Delta(|s'|)}{\hbar v_F} \right]. \quad (4.18)$$

Here, $\exp[-(m+N)\phi_{\mathbf{k}}\hat{\sigma}_y]$ in the Hamiltonian of eq. (4.16) gives only the boundary condition of the eigenfunction:

$$\Phi_\nu(\phi_{\mathbf{k}} + 2\pi) = (-1)^{m+N} \Phi_\nu(\phi_{\mathbf{k}}). \quad (4.19)$$

When b is small, the contribution of b can be treated as perturbation. Since $\sin \tilde{\phi} \approx b/|s|$, the perturbation Hamiltonian is

$$\hat{\mathcal{H}}' = -bm \frac{\Delta(|s|)}{|s|} \hat{\sigma}_y. \quad (4.20)$$

The perturbation energy with angular momentum $L_z = -k_F b$ is

$$E(L_z) = \frac{\int ds \Phi_{\nu, \mathbf{k}}^\dagger(s, b=0) \hat{\mathcal{H}}' \Phi_{\nu, \mathbf{k}}(s, b=0)}{\int ds \Phi_{\nu, \mathbf{k}}^\dagger(s, b=0) \Phi_{\nu, \mathbf{k}}(s, b=0)} = -m L_z \omega_0, \quad (4.21)$$

where

$$\omega_0 \equiv \frac{\int ds |\Phi_0(s)|^2 \frac{\Delta(|s|)}{k_F |s|}}{\int ds |\Phi_0(s)|^2} \sim \frac{1}{\hbar} \frac{\Delta^2}{E_F}. \quad (4.22)$$

We should consider L_z as an operator in quantum mechanics. Then, the Hamiltonian corresponding to energy in eq. (4.21) is

$$\mathcal{H}(\phi_{\mathbf{k}}) = im\hbar\omega_0 \partial_{\phi_{\mathbf{k}}}. \quad (4.23)$$

The Hamiltonian has the eigenfunctions

$$\Phi_{n, \mathbf{k}} = \exp \left(-i \frac{E_n \phi_{\mathbf{k}}}{m\hbar\omega_0} \right). \quad (4.24)$$

From the boundary condition in eq. (4.19), the energy is discretized as

$$E_n = nm\hbar\omega_0, \quad (N : \text{odd}), \quad (4.25)$$

and

$$E_n = \left(n + \frac{1}{2} \right) m\hbar\omega_0, \quad (N : \text{even}), \quad (4.26)$$

with integer n and odd integer m . Therefore, chiral p -wave superfluids ($N = 1$) have the exact zero energy excitation, namely Majorana QP $\gamma_0^\dagger = \gamma_0$, in the vortex with an odd winding number.

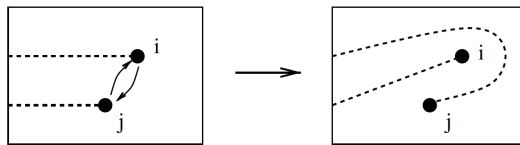


Figure 4.2: Taken from Ivanov [41]. Permutation of neighboring vortices. Dashed lines denote branch cuts of the phase jumping by 2π .

4.1.1 Non-Abelian statistics

A pair of conventional fermionic creation and annihilation operators span a 2D Hilbert space because their square vanishes. This is not true for the Majorana operators because $\gamma_i^2 = \gamma_i \gamma_i^\dagger \neq 0$. Thus, to avoid the problem when two Majorana QPs are present, we can construct “conventional” complex fermionic creation and annihilation operators, $\psi^\dagger = (\gamma_1 - i\gamma_2)/2$ and $\psi = (\gamma_1 + i\gamma_2)/2$, respectively, where the normalization is chosen as $\gamma_i^2 = 1$. These operators satisfy $\psi^2 = \psi^{\dagger 2} = 0$ and thus span a 2D subspace of degenerate ground states associated with these operators [52].

Since a Majorana QP exists in a vortex with an odd winding number for chiral p -wave superfluid, a pair of the vortices can construct the “conventional” complex fermionic operators. Then, the vortices with a Majorana QP obey the non-Abelian statistics [54, 41], because the fermionic operators are defined in a pair of isolated vortices. These nontrivial properties can be utilized for a topological quantum computer [62]. Candidates of the non-Abelian vortex are a half-quantum vortex in the superfluid ^3He A-phase and a singular vortex in a “spinless” p -wave resonant superfluid of Fermi atomic gases.

We can show the non-Abelian statistics of braiding for the vortices with a Majorana QP according to Ref. [41]. We consider a system with $2n$ vortices, far from each other. If the vortices move adiabatically slowly so that we can neglect transitions between subgap levels, the only possible effect of such vortex motion is a unitary evolution in the space of ground states. We consider a permutation of vortices which returns vortices to their original positions. By the permutation of vortices, we disregard the multiparticle state which acquires the overall phase in order to note the change of the bound state in the vortex.

When we permute the neighboring vortices with a winding number $m = 1$, shown in Fig. 4.2 [41], γ_i acquires a phase 2π , where a subscript of a Majorana QP operator indexes a host vortex. Since the wave function of the bound state in the vortex is proportional to $e^{i\frac{\phi}{2}\hat{\sigma}_z}$, the permutation of the vortices transforms γ_i and γ_j into $-\gamma_j$ and γ_i , respectively. Therefore, the action of T_i on Majorana QPs is defined as

$$T_i : \begin{cases} \gamma_i & \rightarrow \gamma_{i+1}, \\ \gamma_{i+1} & \rightarrow -\gamma_i, \\ \gamma_j & \rightarrow \gamma_j, \end{cases} \quad (4.27)$$

where $j \neq i$ and $j \neq i + 1$. T_i obeys the relation:

$$\begin{aligned} T_i T_j &= T_j T_i, & |i - j| > 1, \\ T_i T_j T_i &= T_j T_i T_j, & |i - j| = 1, \end{aligned} \quad (4.28)$$

shown in Fig. 4.3 [41]. The braiding statistics is defined by the unitary operators in the space of ground states representing the braid operations of B_{2n} . Since we disregard the multiparticle

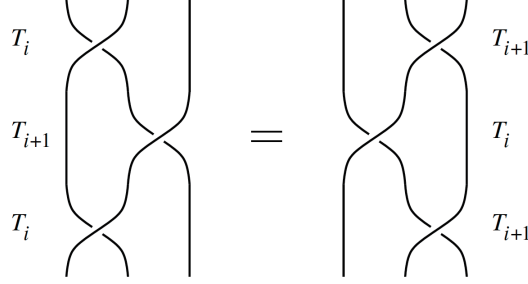


Figure 4.3: Taken from Ivanov [41]. Defining relation for the braid group: $T_i T_{i+1} T_i = T_{i+1} T_i T_{i+1}$. The manner of crossings is important.

state, the permutation of the vortices with a Majorana QP is projected from the braid group B_{2n} . The explicit formulas for this representation may be written in terms of fermionic operators. For the purpose, we need to construct operators $\tau(T_i)$ obeying $\tau(T_i)\gamma_j[\tau(T_i)]^{-1} = T_i(\gamma_j)$, where $T_i(\gamma_j)$ is defined by (4.27). The expression for $\tau(T_i)$ is

$$\tau(T_i) = \exp\left(\frac{\pi}{4}\gamma_{i+1}\gamma_i\right) = \frac{1}{\sqrt{2}}(1 + \gamma_{i+1}\gamma_i). \quad (4.29)$$

The operators are utilized for considering operation of a topological quantum computer [52]. A topological vortex qubit is defined through two pairs of vortices because the fermionic number is fixed to be even or odd [63].

4.2 Majorana edge fermion

In this section, we assume that the OP is uniform for simplicity. Then, eq. (4.10) is

$$\begin{pmatrix} -i\hbar v_{\perp}\partial_{\perp}\hat{\sigma}_0 & \hat{\Delta}(\mathbf{k}) \\ \hat{\Delta}^{\dagger}(\mathbf{k}) & i\hbar v_{\perp}\partial_{\perp}\hat{\sigma}_0 \end{pmatrix} \tilde{\varphi}_{\mathbf{k}_{\parallel}}(r_{\perp}) = E_{\mathbf{k}_{\parallel}}\tilde{\varphi}_{\mathbf{k}_{\parallel}}(r_{\perp}), \quad (4.30)$$

where subscripts \perp and \parallel indicate perpendicular and parallel components to a surface, respectively.

4.2.1 Chiral edge state

The chiral edge state is realized when the superfluid ^3He A-phase is confined in a slab [64, 21, 22, 23]. If there is the surface at $x = 0$ and l -vector and d -vector point to the z -direction, eq. (4.30) is described by

$$\begin{pmatrix} \epsilon(\mathbf{k}) & 0 & 0 & \Delta e^{i\phi_{\mathbf{k}}}\sin\theta_{\mathbf{k}} \\ 0 & \epsilon(\mathbf{k}) & \Delta e^{i\phi_{\mathbf{k}}}\sin\theta_{\mathbf{k}} & 0 \\ 0 & \Delta e^{-i\phi_{\mathbf{k}}}\sin\theta_{\mathbf{k}} & -\epsilon(\mathbf{k}) & 0 \\ \Delta e^{-i\phi_{\mathbf{k}}}\sin\theta_{\mathbf{k}} & 0 & 0 & -\epsilon(\mathbf{k}) \end{pmatrix} \tilde{\varphi}_{\mathbf{k}_{\parallel}}(x) = E_{\mathbf{k}_{\parallel}}\tilde{\varphi}_{\mathbf{k}_{\parallel}}(x), \quad (4.31)$$

where Δ can be taken as real, $\mathbf{k}_{\parallel} = (k_y, k_z)$, $\phi_{\mathbf{k}}$ and $\theta_{\mathbf{k}}$ are the polar angle such that $k_x = k_F \cos\phi_{\mathbf{k}}\sin\theta_{\mathbf{k}}$, $k_y = k_F \sin\phi_{\mathbf{k}}\sin\theta_{\mathbf{k}}$, and $k_z = k_F \cos\theta_{\mathbf{k}}$, and $\epsilon(\mathbf{k}) = -i\hbar v_F \cos\phi_{\mathbf{k}}\sin\theta_{\mathbf{k}}\partial_x$.

By the boundary condition $\varphi_{\mathbf{k}_{\parallel}}(x=0) = 0$, the wave function is

$$\varphi_{\mathbf{k}_{\parallel}}(\mathbf{r}) = \tilde{\varphi}_{\mathbf{k}_{\parallel}}(x) e^{i\mathbf{k}_{\parallel} \cdot \mathbf{r}_{\parallel}} \sin(k_x x), \quad (4.32)$$

where $\mathbf{r}_{\parallel} = (y, z)$. Then, eq. (4.31) can be reduced as one-dimensional Dirac equation

$$\begin{pmatrix} -i\hbar v_F \cos \phi_{\mathbf{k}} \sin \theta_{\mathbf{k}} \partial_x & \Delta e^{i\phi_{\mathbf{k}}} \sin \theta_{\mathbf{k}} \\ \Delta e^{-i\phi_{\mathbf{k}}} \sin \theta_{\mathbf{k}} & i\hbar v_F \cos \phi_{\mathbf{k}} \sin \theta_{\mathbf{k}} \partial_x \end{pmatrix} \tilde{\Phi}_{\mathbf{k}_{\parallel}}(x) = E_{\mathbf{k}_{\parallel}} \tilde{\Phi}_{\mathbf{k}_{\parallel}}(x). \quad (4.33)$$

The eigenfunction of eq. (4.33) is

$$\tilde{\Phi}_{\mathbf{k}_{\parallel}}(x) \propto \exp\left(-\frac{\Delta x}{\hbar v_F}\right) \begin{pmatrix} 1 \\ -i \end{pmatrix}, \quad (4.34)$$

with energy

$$E_{\mathbf{k}_{\parallel}} = \Delta \frac{k_y}{k_F}. \quad (4.35)$$

Therefore,

$$\Phi_{\mathbf{k}_{\parallel}}(\mathbf{r}) = u_{k_x} e^{i\mathbf{k}_{\parallel} \cdot \mathbf{r}_{\parallel}} \sin(k_x x) \exp\left(-\frac{\Delta x}{\hbar v_F}\right) \begin{pmatrix} 1 \\ -i \end{pmatrix}, \quad (4.36)$$

where the normalization constant u_{k_x} satisfies

$$2|u_{k_x}|^2 \int_0^{\infty} dx \sin^2(k_x x) \exp\left(-\frac{2\Delta x}{\hbar v_F}\right) = 1. \quad (4.37)$$

From eq. (2.12), field operators are expanded in terms of Bogoliubov operators $\gamma_{\mathbf{k}_{\parallel}, \sigma}$ as

$$\begin{pmatrix} \psi_{\sigma}(\mathbf{r}) \\ \psi_{\sigma}^{\dagger}(\mathbf{r}) \end{pmatrix} = u_{k_x} \sin(k_x x) \exp\left(-\frac{\Delta x}{\hbar v_F}\right) \sum_{\mathbf{k}_{\parallel}, \sigma'} \left[\gamma_{\mathbf{k}_{\parallel}, \sigma'} e^{i\mathbf{k}_{\parallel} \cdot \mathbf{r}_{\parallel}} \begin{pmatrix} 1 \\ -i \end{pmatrix} + \gamma_{\mathbf{k}_{\parallel}, \sigma'}^{\dagger} e^{-i\mathbf{k}_{\parallel} \cdot \mathbf{r}_{\parallel}} \begin{pmatrix} i \\ 1 \end{pmatrix} \right] + \Psi_{\text{bulk}}, \quad (4.38)$$

where Ψ_{bulk} denotes the contribution from the bulk excitations. Although Ψ_{bulk} contains the low energy states due to point nodes, their contributions are negligible if $T \ll T_c$ is considered [21]. Therefore, the chiral edge state has the Majorana fermion $\psi_{\sigma} = i\psi_{\sigma}^{\dagger}$ for $T \ll T_c$.

4.2.2 Helical edge state

The helical edge state is realized for the superfluid ^3He B-phase [65, 66, 67, 68]. We consider that there is the surface at $x=0$ and the rotation matrix of the OP is $\hat{R}(\hat{\mathbf{x}}, \theta_L)$. If we rotate the spin coordinate by the Leggett angle θ_L around the x -axis, the OP is described by

$$\hat{\Delta}(\mathbf{k}) = \begin{pmatrix} \Delta(-\cos \theta_{\mathbf{k}} + i \cos \phi_{\mathbf{k}} \sin \theta_{\mathbf{k}}) & \Delta \sin \phi_{\mathbf{k}} \sin \theta_{\mathbf{k}} \\ \Delta \sin \phi_{\mathbf{k}} \sin \theta_{\mathbf{k}} & \Delta(\cos \theta_{\mathbf{k}} + i \cos \phi_{\mathbf{k}} \sin \theta_{\mathbf{k}}) \end{pmatrix}, \quad (4.39)$$

where $k_x = k_F \cos \theta_{\mathbf{k}}$, $k_y = k_F \cos \phi_{\mathbf{k}} \sin \theta_{\mathbf{k}}$, and $k_z = k_F \sin \phi_{\mathbf{k}} \sin \theta_{\mathbf{k}}$ with $-\pi/2 \leq \theta_{\mathbf{k}} \leq \pi/2$. Then, eq. (4.30) is described by

$$\begin{pmatrix} \epsilon(\mathbf{k}) \hat{\sigma}_0 & \hat{\Delta}(\mathbf{k}) \\ \hat{\Delta}^{\dagger}(\mathbf{k}) & -\epsilon(\mathbf{k}) \hat{\sigma}_0 \end{pmatrix} \tilde{\varphi}_{\mathbf{k}_{\parallel}}(x) = E_{\mathbf{k}_{\parallel}} \tilde{\varphi}_{\mathbf{k}_{\parallel}}(x), \quad (4.40)$$

where $\epsilon(\mathbf{k}) = -i\hbar v_F \cos \theta_{\mathbf{k}} \partial_x$. By the boundary condition $\varphi_{\mathbf{k}_{\parallel}}(x=0) = 0$, the wave function is

$$\varphi_{\mathbf{k}_{\parallel}}(\mathbf{r}) = \tilde{\varphi}_{\mathbf{k}_{\parallel}}(x) e^{i\mathbf{k}_{\parallel} \cdot \mathbf{r}_{\parallel}} \sin(k_x x). \quad (4.41)$$

For energy eigenvalue of the up-spin state

$$E_{\mathbf{k}_{\parallel}, \uparrow} = -\Delta \sin \theta_{\mathbf{k}}, \quad (4.42)$$

the eigenfunction is given by

$$\tilde{\varphi}_{\mathbf{k}_{\parallel}, \uparrow}(x) \propto \exp\left(-\frac{\Delta x}{\hbar v_F}\right) \begin{pmatrix} \sin \frac{\phi_{\mathbf{k}} + \pi}{2} \\ i \cos \frac{\phi_{\mathbf{k}} + \pi}{2} \\ i \sin \frac{\phi_{\mathbf{k}} + \pi}{2} \\ \cos \frac{\phi_{\mathbf{k}} + \pi}{2} \end{pmatrix}. \quad (4.43)$$

For the energy eigenvalue of the down-spin state

$$E_{\mathbf{k}_{\parallel}, \downarrow} = \Delta \sin \theta_{\mathbf{k}}, \quad (4.44)$$

the eigenfunction is given by

$$\tilde{\varphi}_{\mathbf{k}_{\parallel}, \downarrow}(x) \propto \exp\left(-\frac{\Delta x}{\hbar v_F}\right) \begin{pmatrix} \cos \frac{\phi_{\mathbf{k}} + \pi}{2} \\ -i \sin \frac{\phi_{\mathbf{k}} + \pi}{2} \\ i \cos \frac{\phi_{\mathbf{k}} + \pi}{2} \\ -\sin \frac{\phi_{\mathbf{k}} + \pi}{2} \end{pmatrix}. \quad (4.45)$$

Therefore,

$$\varphi_{\mathbf{k}_{\parallel}, \uparrow}(\mathbf{r}) = u_{k_x} e^{i\mathbf{k}_{\parallel} \cdot \mathbf{r}_{\parallel}} \sin(k_x x) \exp\left(-\frac{\Delta x}{\hbar v_F}\right) \begin{pmatrix} \sin \frac{\phi_{\mathbf{k}} + \pi}{2} \\ i \cos \frac{\phi_{\mathbf{k}} + \pi}{2} \\ i \sin \frac{\phi_{\mathbf{k}} + \pi}{2} \\ \cos \frac{\phi_{\mathbf{k}} + \pi}{2} \end{pmatrix}, \quad (4.46)$$

and

$$\varphi_{\mathbf{k}_{\parallel}, \downarrow}(\mathbf{r}) = u_{k_x} e^{i\mathbf{k}_{\parallel} \cdot \mathbf{r}_{\parallel}} \sin(k_x x) \exp\left(-\frac{\Delta x}{\hbar v_F}\right) \begin{pmatrix} \cos \frac{\phi_{\mathbf{k}} + \pi}{2} \\ -i \sin \frac{\phi_{\mathbf{k}} + \pi}{2} \\ i \cos \frac{\phi_{\mathbf{k}} + \pi}{2} \\ -\sin \frac{\phi_{\mathbf{k}} + \pi}{2} \end{pmatrix}. \quad (4.47)$$

From eq. (2.12), field operators are expanded in terms of Bogoliubov operators $\gamma_{\mathbf{k}_{\parallel},\sigma}$ as

$$\begin{aligned}
\begin{pmatrix} \psi_{\uparrow}(\mathbf{r}) \\ \psi_{\downarrow}(\mathbf{r}) \\ \psi_{\uparrow}^{\dagger}(\mathbf{r}) \\ \psi_{\downarrow}^{\dagger}(\mathbf{r}) \end{pmatrix} &= u_{k_x} \sin(k_x x) \exp\left(-\frac{\Delta x}{\hbar v_F}\right) \\
&\times \sum_{\mathbf{k}_{\parallel}} \left\{ e^{i\mathbf{k}_{\parallel} \cdot \mathbf{r}_{\parallel}} \left[\gamma_{\mathbf{k}_{\parallel},\uparrow} \begin{pmatrix} \sin \frac{\phi_{\mathbf{k}+\pi}}{2} \\ i \cos \frac{\phi_{\mathbf{k}+\pi}}{2} \\ i \sin \frac{\phi_{\mathbf{k}+\pi}}{2} \\ \cos \frac{\phi_{\mathbf{k}+\pi}}{2} \end{pmatrix} + \gamma_{\mathbf{k}_{\parallel},\downarrow} \begin{pmatrix} \cos \frac{\phi_{\mathbf{k}+\pi}}{2} \\ -i \sin \frac{\phi_{\mathbf{k}+\pi}}{2} \\ i \cos \frac{\phi_{\mathbf{k}+\pi}}{2} \\ -\sin \frac{\phi_{\mathbf{k}+\pi}}{2} \end{pmatrix} \right] \right. \\
&+ \left. e^{-i\mathbf{k}_{\parallel} \cdot \mathbf{r}_{\parallel}} \left[\gamma_{\mathbf{k}_{\parallel},\uparrow}^{\dagger} \begin{pmatrix} -i \sin \frac{\phi_{\mathbf{k}+\pi}}{2} \\ \cos \frac{\phi_{\mathbf{k}+\pi}}{2} \\ \sin \frac{\phi_{\mathbf{k}+\pi}}{2} \\ -i \cos \frac{\phi_{\mathbf{k}+\pi}}{2} \end{pmatrix} + \gamma_{\mathbf{k}_{\parallel},\downarrow}^{\dagger} \begin{pmatrix} -i \cos \frac{\phi_{\mathbf{k}+\pi}}{2} \\ -\sin \frac{\phi_{\mathbf{k}+\pi}}{2} \\ \cos \frac{\phi_{\mathbf{k}+\pi}}{2} \\ i \sin \frac{\phi_{\mathbf{k}+\pi}}{2} \end{pmatrix} \right] \right\} + \Psi_{\text{bulk}}. \quad (4.48)
\end{aligned}$$

We can disregard gapped modes from a bulk, where energy is greater than Δ , when $T \ll T_c$. Therefore, the helical edge state has the Majorana fermion $\psi_{\uparrow} = -i\psi_{\uparrow}^{\dagger}$ and $\psi_{\downarrow} = i\psi_{\downarrow}^{\dagger}$ for $T \ll T_c$.

Chapter 5

Superfluid ^3He in a cylinder

In this chapter, we discuss the textures of the superfluid ^3He A-phase confined in a narrow cylinder [19, 20]. It is known that in the absence of field, the Mermin-Ho (MH) texture [69, 70] is stable under confined geometries at rest where spontaneous mass current flows along the boundary wall. This MH texture is so generic and stable topologically, thus characteristic to multi-component order parameter (OP) superfluids. It exists even in the spinor BEC [71, 72, 73, 74]. However, as the confining system becomes smaller and comparable to their characteristic length scale $\sim \xi_d$ ($\simeq 10 \mu\text{m}$), the texture formation becomes difficult due to the kinetic energy penalty, leading to destabilization of MH. Similarly MH becomes unstable under magnetic fields whose order is H_d ($\simeq 2 \text{ mT}$) [75, 76]. It is not known theoretically and experimentally what exactly condition is needed for that and what kind of texture is stabilized in such a situation.

Here we are going to solve this problem in connection with the on-going experiments performed in ISSP, Univ. of Tokyo. They use two narrow cylinders with radii $R=50 \mu\text{m}$ and $115 \mu\text{m}$ filled with ^3He A-phase. These two kinds of cylinders are rotated up to the maximum rotation speed $\Omega=11.5 \text{ rad/s}$ under a field applied along the rotation axis z and pressure $P=3.2 \text{ MPa}$. They monitor the NMR spectrum to characterize textures created in a sample. So far the following facts are found [77, 78, 79, 80, 81]:

- (1) At rest an un-identified texture is seen for both samples with $R=50 \mu\text{m}$ and $115 \mu\text{m}$. The texture, which has a characteristic resonance spectrum, persists down to the lowest temperature $T/T_c=0.7$, below which the B-phase starts to appear, from the onset temperature $T_c=2.3 \text{ mK}$. Thus the ground state in those narrow cylinders is this un-identified texture.
- (2) Upon increasing Ω this texture is eventually changed into the MH texture which was identified before for $R=115 \mu\text{m}$ by the same NMR experiment [79]. The critical rotation speed $\Omega_c \sim 0.5 \text{ rad/s}$, which is identified as a sudden intensity change of the main peak in the resonance spectrum.
- (3) With further increasing Ω the so-called continuous unlocked vortex (CUV) are identified for $R=115 \mu\text{m}$ sample. The successive transitions from the MH to one CUV, two CUVs, etc., in high rotation regions are explained basically by Takagi [82] who solves the same GL functional as in this chapter. However, the calculations are assumed to be the A-phase in the whole region. Thus the following calculation is consistent with those by Takagi [82]. Those successive transitions are absent in $R=50 \mu\text{m}$ sample because the estimated critical Ω for CUV exceeds the maximum rotation speed 11.5 rad/s in the rotating cryostat in ISSP.
- (4) The un-identified texture for $R=115 \mu\text{m}$ sample stable at rest and under low rotations exhibits a hysteretic behavior about $\pm\Omega$ rotation sense [78], meaning that this texture with

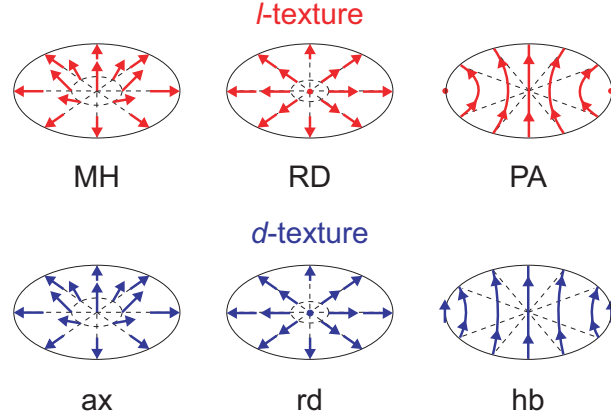


Figure 5.1: The possible textures of the l -vectors (upper) and d -vectors (lower) are shown schematically. The Mermin-Ho (MH), radial disgyration (RD) and Pan-Am (PA) are for the l -vector textures (upper panel). The axial type (ax), radial disgyration (rd) and hyperbolic type (hb) are for the d -vector textures (lower panel). The points in MH, PA and rd-type denote positions of singularity.

$\Omega > 0$ differs from that with $\Omega < 0$, namely, this texture has polarity. These textures with $\pm\Omega$ cannot continuously deform to each other. This feature is completely absent for the texture for $R=50 \mu\text{m}$ sample because the NMR spectra for $\pm\Omega$ are identical [81]. Thus we have to distinguish two kinds of the texture which are stable at rest and under low rotations for $R=50 \mu\text{m}$ and $115 \mu\text{m}$. Before going into the detailed calculations, we introduce here the possible textures to be examined in the following: The texture consists of the orbital and spin parts, each of which is characterized by l -vector and d -vector respectively. Thus the total order parameter, or the texture is fully characterized by the combination of the l -texture and d -texture. In Fig. 5.1 we schematically show the possible l -textures and d -textures, where MH l -vector and ax-type d -vector change smoothly and flare out towards the wall. In contrast, the RD [83, 84] and the rd-type have a singularity at the center. l -vector in PA [85] and d -vector in hb-type show a hyperbolic like spatial structure. In the following we examine the four textures, MH-ax, MH-hb, RD-ax and RD-hb, which turn out to be relevant and compete energetically with each other in the present situations.

The arrangement of this chapter is as follows: After giving the Ginzburg-Landau (GL) free energy functional, we set up the GL parameters appropriate for the present experimental situation in Sec. 5.1. Here the boundary condition which is essential for the present narrow cylinders is examined. We explain also our numerics to evaluate various possible textures. In Sec. 5.2 we list up possible l -vector and d -vector textures both at rest and under rotation. In Sec. 5.3 we identify the ground state texture by comparing the GL free energy for various radii R of the cylinder, rotation speeds Ω and magnetic fields H . We critically examine the on-going experiments at ISSP by using the rotating cryostat in the light of the above calculations in Sec. 5.4. The final section is devoted to a summary.

5.1 Formulation

5.1.1 Ginzburg-Landau functional for the superfluid ^3He

The OP of the superfluid ^3He is given by [2]

$$\hat{\Delta}(\mathbf{r}, \mathbf{k}) = (i\hat{\sigma}\hat{\sigma}_y) \cdot \mathbf{\Delta}(\mathbf{r}, \mathbf{k}), \quad (5.1)$$

with the Pauli matrix $\hat{\sigma}$ in spin space. The $\mathbf{\Delta}$ can be expanded in orbital momentum directions,

$$\Delta_\mu(\mathbf{r}, \mathbf{k}) = A_{\mu i}(\mathbf{r})k_i, \quad (5.2)$$

where $A_{\mu i}(\mathbf{r})$ is a complex 3×3 matrix with a spin index μ and an orbital index i . The repeated index implies summation over x , y , and z . Thus superfluid ^3He is characterized rank-2 tensor components $A_{\mu i}$ inherent in the p -wave pairing ($L = 1$) with spin $S = 1$, where μ and i denote cartesian coordinates of the spin and orbital spaces, respectively.

In order to understand the stable texture at rest and lower rotations, we examine the standard GL functional, which was written down in the 1970's. The parameters in the functional are well established thanks to the intensive theoretical and experimental studies over thirty years [86, 87, 88, 89, 90]. Namely, we start with the following GL form written in terms of the tensor A forming OP of p -wave pairing. The most general GL functional density f_{bulk} for the bulk condensation energy up to fourth order is written as

$$\begin{aligned} f_{\text{bulk}} = & -\alpha A_{\mu i}^* A_{\mu i} + \beta_1 A_{\mu i}^* A_{\mu i}^* A_{\nu j} A_{\nu j} + \beta_2 A_{\mu i}^* A_{\mu i} A_{\nu j}^* A_{\nu j} + \beta_3 A_{\mu i}^* A_{\nu i}^* A_{\mu j} A_{\nu j} \\ & + \beta_4 A_{\mu i}^* A_{\nu i} A_{\nu j}^* A_{\mu j} + \beta_5 A_{\mu i}^* A_{\nu i} A_{\nu j} A_{\mu j}^*, \end{aligned} \quad (5.3)$$

which is invariant under spin and real space rotations in addition to the gauge invariance $U(1) \times SO^{(S)}(3) \times SO^{(L)}(3)$. The coefficient $\alpha(T)$ of the second order invariant is T -dependent as usual, and the fourth order terms have five invariants with coefficients β_j in general. The gradient energy consisting of the three independent terms is given by

$$f_{\text{grad}} = K_1(\partial_i^* A_{\mu j}^*)(\partial_i A_{\mu j}) + K_2(\partial_i^* A_{\mu j}^*)(\partial_j A_{\mu i}) + K_3(\partial_i^* A_{\mu i}^*)(\partial_j A_{\mu j}). \quad (5.4)$$

where $\partial_i = \nabla_i - i(2m_3/\hbar)(\mathbf{\Omega} \times \mathbf{r})_i$ with the angular velocity $\mathbf{\Omega} \parallel \mathbf{z}$, which is parallel to the cylinder long axis and $\mathbf{\Omega} > 0$ means the counter clock-wise rotation. In addition, there are the dipole and magnetic field energies:

$$f_{\text{dipole}} = g_d \left(A_{\mu\mu}^* A_{\nu\nu} + A_{\mu\nu}^* A_{\nu\mu} - \frac{2}{3} A_{\mu\nu}^* A_{\mu\nu} \right), \quad (5.5)$$

$$f_{\text{field}} = g_m H_\mu A_{\mu i}^* H_\nu A_{\nu i}. \quad (5.6)$$

In the A-phase the spin and orbital parts of the OP are factorized, i.e. $A_{\mu i} = \hat{d}_\mu A_i$, where the spin part is denoted by \hat{d}_μ and the orbital part by A_i . The $\hat{\mathbf{d}}$ is a unit vector. We can describe the Anderson-Brinkman-Morel (ABM) and polar state under this notation. Now, eqs. (5.3) – (5.6) are rewritten as

$$f_{\text{bulk}} = -\alpha A_i^* A_i + \beta_{13} A_i^* A_i^* A_j A_j + \beta_{245} A_i^* A_j^* A_i A_j, \quad (5.7)$$

$$f_{\text{grad}} = K_1(\partial_i^* \hat{d}_\mu A_j^*)(\partial_i \hat{d}_\mu A_j) + K_2(\partial_i^* \hat{d}_\mu A_j^*)(\partial_j \hat{d}_\mu A_i) + K_3(\partial_i^* \hat{d}_\mu A_i^*)(\partial_j \hat{d}_\mu A_j), \quad (5.8)$$

$$f_{\text{dipole}} = g_d \left[\hat{d}_\mu \hat{d}_\nu (A_\mu^* A_\nu + A_\nu^* A_\mu) - \frac{2}{3} A_\nu^* A_\nu \right], \quad (5.9)$$

$$f_{\text{field}} = g_m A_i^* A_i (\hat{\mathbf{d}} \cdot \mathbf{H})^2, \quad (5.10)$$

where $\beta_{13} = \beta_1 + \beta_3$, and $\beta_{245} = \beta_2 + \beta_4 + \beta_5$.

The coefficients α , β_j , K_j , g_m , and g_d are determined by Thuneberg [91] and Kita [92] as follows. The weak-coupling theory gives

$$\alpha = \frac{N(0)}{3} \left(1 - \frac{T}{T_c}\right) \equiv \alpha_0 \left(1 - \frac{T}{T_c}\right), \quad (5.11)$$

$$-2\beta_1^{WC} = \beta_2^{WC} = \beta_3^{WC} = \beta_4^{WC} = -\beta_5^{WC} = \frac{7\zeta(3)N(0)}{120(\pi k_B T_c)^2}, \quad (5.12)$$

$$K_1 = K_2 = K_3 = \frac{7\zeta(3)N(0)(\hbar v_F)^2}{240(\pi k_B T_c)^2} \equiv K, \quad (5.13)$$

where $N(0)$ and v_F are the density of states per spin and the Fermi velocity, respectively. The coefficients α_0 and K are estimated by eqs. (5.11) and (5.13) by using the values of $N(0)$, T_c and v_F which are determined experimentally by Greywall [88] within the weak-coupling theory. It is known that strong-coupling corrections for β_j are needed to stabilize A-phase, and we use the β_j values estimated by Sauls and Serene [87] theoretically. The strong-coupling corrections of β_{13} and β_{245} which are coefficients in Eq. (5.7) have good agreement with the corrections evaluated from experimental data [90]. The value of g_d is [89]

$$g_d = \frac{\mu_0}{40} \left(\gamma \hbar N(0) \ln \frac{1.1339 \times 0.45 T_F}{T_c} \right)^2, \quad (5.14)$$

where μ_0 and γ denote the permeability of vacuum and the gyromagnetic ratio, respectively, and T_F is the Fermi temperature defined by $T_F \equiv 3n/4N(0)k_B$ with the density n . Finally, g_m is given within the weak-coupling expression by

$$g_m = \frac{7\zeta(3)N(0)(\gamma \hbar)^2}{48[(1 + F_0^a)\pi k_B T_c]^2}, \quad (5.15)$$

with F_0^a the Landau parameter taken from Wheatley [86] but corrected for the newly determined effective mass [88].

We set all the GL parameters to correspond to the above experimental pressure $P=3.2$ MPa, which are summarized as

$$\begin{aligned} \alpha_0 &= \frac{N(0)}{3} = 3.81 \times 10^{50} \text{J}^{-1} \text{m}^{-3}, \\ \beta_1 &= -3.75 \times 10^{99} \text{J}^{-3} \text{m}^{-3}, \\ \beta_2 &= 6.65 \times 10^{99} \text{J}^{-3} \text{m}^{-3}, \\ \beta_3 &= 6.56 \times 10^{99} \text{J}^{-3} \text{m}^{-3}, \\ \beta_4 &= 5.99 \times 10^{99} \text{J}^{-3} \text{m}^{-3}, \\ \beta_5 &= -8.53 \times 10^{99} \text{J}^{-3} \text{m}^{-3}, \\ K &= 4.19 \times 10^{34} \text{J}^{-1} \text{m}^{-1}, \\ g_d &= 5.61 \times 10^{44} \text{J}^{-1} \text{m}^{-3}, \\ g_m &= 1.35 \times 10^{44} \text{J}^{-1} \text{m}^{-3} (\text{mT})^{-2}, \\ \frac{2m_3}{\hbar} &= 9.51 \times 10^7 \text{m}^{-2} \text{s}. \end{aligned}$$

Corresponding to these parameters, the dipole field is estimated as $H_d = \sqrt{g_d/g_m} \sim 2$ mT, which is a characteristic magnetic field where the dipole and magnetic field energies become same order.

The stable texture can be found by minimizing total free energy,

$$F = \int d^3r f(\mathbf{r}) = \int d^3r (f_{\text{bulk}} + f_{\text{grad}} + f_{\text{dipole}} + f_{\text{field}}). \quad (5.16)$$

We have identified stationary solutions by numerically solving the variational equations: $\delta f(\mathbf{r})/\delta \hat{d}_\mu(\mathbf{r}) = 0$, $\delta f(\mathbf{r})/\delta A_i(\mathbf{r}) = 0$ in cylindrical systems, assuming the uniformity towards the z direction. The height of the cylinders used in ISSP experiments are ~ 3 mm, which allows us to adopt this assumption. Thus we obtain the stable d -textures and l -textures. Namely, we solve the coupled GL equations in two dimensions. The l -vector is defined as

$$l_i \equiv -i\epsilon_{ijk} \frac{A_j^* A_k}{|\Delta|^2}, \quad (5.17)$$

where ϵ_{ijk} is totally antisymmetric tensor and $|\Delta|^2 = A_i^* A_i$ is the squared amplitude of OP. The mass current is given by

$$j_i \equiv \frac{4m_3 K}{\hbar} \text{Im}(A_j^* \nabla_i A_j + A_j^* \nabla_j A_i + A_i^* \nabla_j A_j). \quad (5.18)$$

Here we expand the orbital part of the OP in the basis of spherical harmonics Y_{lm} ($l = 1, m = -1, 0, 1$) for ease to express the initial configuration of the l -textures;

$$A(\hat{\mathbf{p}}) = A_+ \hat{p}_+ + A_0 \hat{p}_0 + A_- \hat{p}_-, \quad (5.19)$$

where $\hat{p}_\pm = \mp(\hat{p}_x \pm i\hat{p}_y)/\sqrt{2}$, $\hat{p}_0 = \hat{p}_z$ and $A_\pm = \mp(A_x \mp iA_y)/\sqrt{2}$, $A_0 = A_z$.

It is noted that the characteristic length associated with the dipole energy is given by $\xi_d = \sqrt{K/g_d}$, which is estimated to be an order of $10 \mu\text{m}$. In contrast, the usual coherence length is $\xi = \sqrt{K/\alpha} = \xi_0/\sqrt{1-T/T_c}$, where the coherence length at zero temperature $\xi_0 \sim 0.01 \mu\text{m}$. These two length scales differ by three orders of magnitude which causes great difficulty to handle the problem involved both scales simultaneously. This is indeed our problem. The radial disgyration (RD) has a phase singularity at the center where the l -vector vanishes around ξ -scale region while MH has no singularity and l -vector is non-vanishing everywhere whose spatial variation is characterized by ξ_d . In order to compare two energies, we need to handle two scales simultaneously. Since at the boundary l -vector is constrained such that it is always perpendicular to the wall, thus RD and MH exhibit a similar l -vector texture, differing only around the center of a cylinder. We evaluate possible l -textures RD and MH in combination with d -textures; axial type (ax) and hyperbolic type (hb). The radial disgyration of d -texture (rd) is neglected since it has a singularity where superfluidity is broken. Namely, we mainly examine four kinds of texture, RD-ax, RD-hb, MH-ax and MH-hb in addition to the Pan-Am (PA) only for smaller systems in this paper. Those textures, we believe, exhausts all relevant stable textures. There is no other texture known in literature [2].

5.1.2 Numerics and boundary condition

The numerical computations have been done by using polar coordinates (r, θ) . The radial direction r is discretized into 1000 meshes for $R=50 \mu\text{m}$ system and 2300 meshes for $R=115$

μm while the azimuthal angle θ is discretized in 180 points. Thus the total lattice points are 1000×180 and 2300×180 in (r, θ) coordinate system for $R=50 \mu\text{m}$ and $R=115 \mu\text{m}$ respectively. The average lattice spacing is an order of $5\xi_0$ for both cases, which is fine enough to accurately describe a singular core in RD. Note that we are considering high temperature region, $\xi(T = 0.95T_c) \sim 4.5\xi_0 \sim 45 \text{ nm}$ while our lattice spacing is 50 nm . The advantages of using (r, θ) coordinate system over the rectangular (x, y) system are (1) we can reduce the total lattice points, keeping the numerical accuracy and (2) it is easy to take into account the boundary condition at the wall where the l -vector orients along the perpendicular direction to the wall, namely the radial direction \mathbf{r} . The disadvantage is that we cannot describe the Pan-Am (PA) type configuration for the l -vector.

On each lattice points the nine variational parameters are assigned, coming from the complex variable $A_i (i = x, y, z)$ and the real three dimensional vector $d_\mu (\mu = x, y, z)$. These nine parameters are determined iteratively and self-consistently by solving the coupled GL equations. One solution needs ~ 7 days for $R=50 \mu\text{m}$ system and ~ 20 days for $R=115 \mu\text{m}$ system by using OpenMP programming on a XEON 8 core machine. The applied field $H=21.6 \text{ mT}$ is taken for all calculation except for subsection 5.3.2.

In this chapter, we assume a specular boundary wall. At the wall, the components of the OP having momentum parallel to the wall are not affected, whereas the perpendicular component to the wall is suppressed completely. Realistic walls may be diffusive boundaries where the parallel components may be also reduced. However, since it is difficult to accurately estimate the reductions of OP, we apply the specular boundary condition in this chapter. The diffusive boundary condition is favorable for the PA texture over the RD, since the condensation energy which is cost by singularities at the wall decreases. For small radius cases $R \leq 20 \mu\text{m}$, we confirm that the PA texture is not stable compared to the RD (see subsection 5.2.3 for detail). For large radius cases, we examine the PA texture by considering the actual experimental results, because the numerical calculation for the PA texture is difficult.

5.2 Stable textures

In order to help identifying the possible texture realized in narrow cylinders ($R=50 \mu\text{m}$ and $115 \mu\text{m}$) both at rest and under rotation, we first examine the detailed spatial structures for each texture, which consists of the l -vector and d -vector before discussing the relative stability among them under actual experimental setups.

5.2.1 Radial disgyration (RD)

The RD is characterized by having a singularity at the center where $A_\pm(r=0) = 0$ and $A_0(r=0) \neq 0$. Thus the vortex core is filled by A_0 component, namely it is a polar core vortex [93]. The associated d -vector texture could be either hb-type or ax-type. The l -vector texture can be obtained by starting with an initial configuration:

$$\begin{aligned} A_+(r, \theta) &= \frac{\Delta A}{2} \tanh\left(\frac{r}{\xi}\right) e^{-i\theta}, \\ A_0(r, \theta) &= \frac{\Delta A}{\sqrt{2}}, \\ A_-(r, \theta) &= \frac{\Delta A}{2} \tanh\left(\frac{r}{\xi}\right) e^{i\theta}, \end{aligned} \tag{5.20}$$

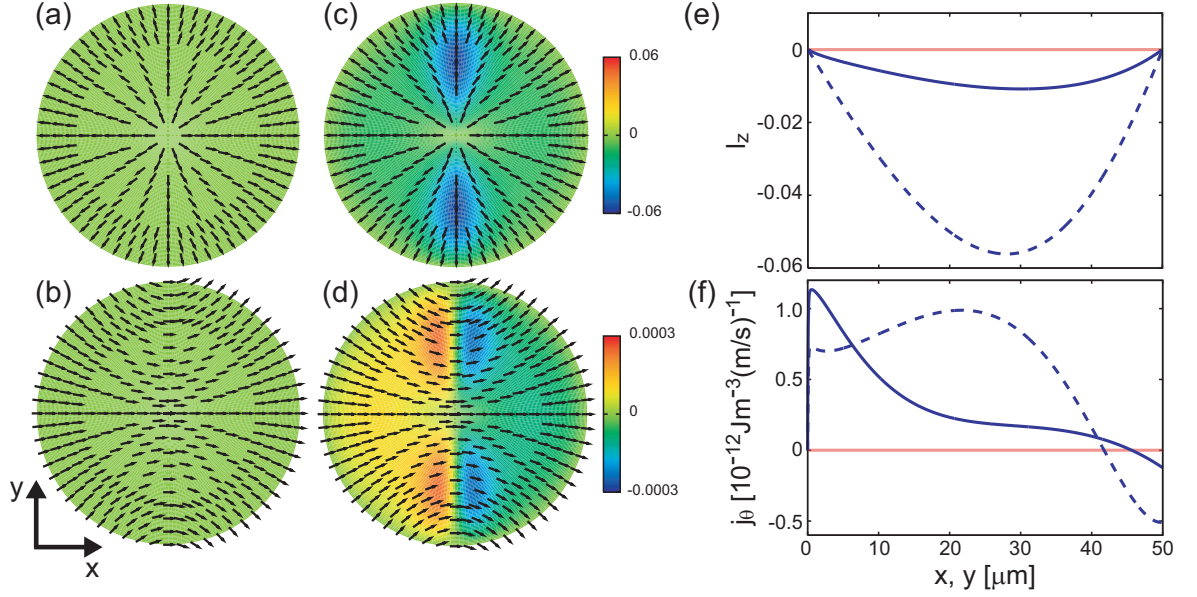


Figure 5.2: Stable textures and current for RD-hb under $R=50 \mu\text{m}$ and $T/T_c = 0.95$. (a) l -vector textures at rest. (b) d -vector textures at rest. (c) l -vector textures at $\Omega=3$ rad/s. (d) d -vector textures at $\Omega=3$ rad/s. The arrows indicate the x - y component and color codes denote its z component. (e) The z component of the l -vector and (f) the current j_θ along the radial direction r from the center. The red lines are at rest and blue lines are $\Omega=3$ rad/s. The solid (dashed) lines are along x - (y -)axis.

where Δ_A is the amplitude of OP in the bulk region far away from the center and boundary. The combination of the winding number in RD is $(w_+, w_0, w_-) = (-1, 0, 1)$, where w_+ , w_0 and w_- are the winding numbers for A_+ , A_0 and A_- respectively. The A_\pm components are suppressed over ξ distance from the center while the A_0 component is larger in the center. Since at the center only the A_0 component is non-vanishing, the polar state is realized there as mentioned before. It is seen from eq. (5.17) that in this RD form $l_z = 0$ because of $|A_+| = |A_-|$.

In Fig. 5.2 we show the results of the stable RD-hb textures for $R=50 \mu\text{m}$, where Figs. 5.2(a) and 5.2(b) at rest and Figs. 5.2(c) and 5.2(d) at $\Omega=3$ rad/s. It is seen that l -vectors flare out from the center and point perpendicular to the wall (Fig. 5.2(a)). The d -vectors point almost to the horizontal direction (the x -axis), and curve near the wall (Fig. 5.2(b)), because the dipole interaction tends to align the d -vector parallel to the l -vector direction. We call it “hyperbolic” (hb). The l -vectors do not point completely to the radial direction, but are twisted slightly due to the dipole interaction. Since the l -vectors are strongly constrained by the boundary condition, they should be perpendicular to the wall so as to suppress the perpendicular motion of the Cooper pair. In other words, point nodes which locate to the l -vector direction should direct to the wall, thus saving the condensation energy loss. Note that there is no z -components for both \mathbf{l} and \mathbf{d} in RD-hb at rest. It will be soon shown that this RD texture is most stable at rest and lower rotations in narrow cylinders.

Once the rotation is turned on, the l -vectors and d -vectors now acquire the z components. It is seen from Fig. 5.2(c) that the l -vectors tend to point the negative z direction, recognized

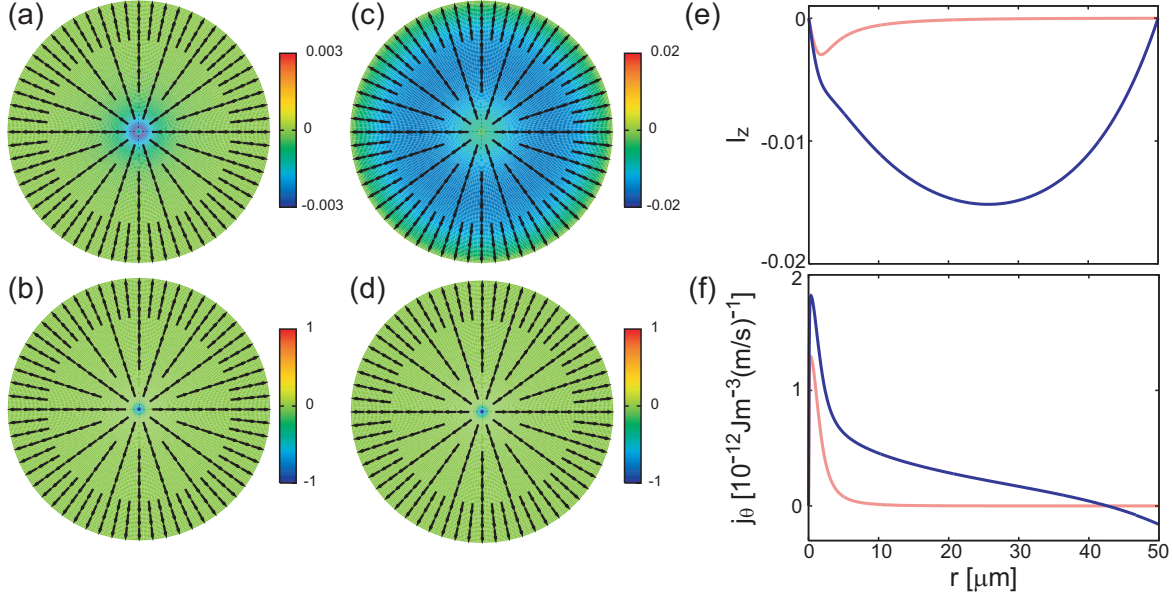


Figure 5.3: Textures and current for RD-ax under $R=50 \mu\text{m}$ and $T/T_c = 0.95$. (a) l -vector textures at rest. (b) d -vector textures at rest. (c) l -vector textures at $\Omega=3$ rad/s. (d) d -vector textures at $\Omega=3$ rad/s. The arrows indicate the x - y component and color codes denote its z component. (e) The z component of the l -vector and (f) the current j_θ along the radial direction r from the center. The red lines are at rest and blue lines are at $\Omega=3$ rad/s.

as the color changes and also seen from Fig. 5.2(e). That region is confined along the y -axis where the dipole interaction, which tend to $\mathbf{l} \parallel \mathbf{d}$, is not effective compared with other regions. In Fig. 5.2(e) the cross sections of l_z component are displayed. It is clear that l_z component is mainly induced along the y -axis. Simultaneously, as shown in Fig. 5.2(d) the d -vectors point to $\pm z$ directions whose boundary occurs along the vertical direction, that is, the y -axis. As shown in Fig. 5.2(f) the variation of the l -vectors produces the in-plane mass current. The $j_\theta(x, y)$ distributions in the x - y plane are anisotropic. Along the radial direction the j_θ changes the sign, namely, it is the same direction as the external rotation in the central region while opposite in the outer region.

As for RD-ax, which is displayed in Fig. 5.3. The l -vector and d -vector textures at rest are shown in Figs. 5.3(a) and 5.3(b), respectively. These textures are seen to be cylindrically symmetric. The d -vectors around the center point to the negative z direction (Fig. 5.3(b)). The area is characterized by magnetic coherence length $\xi_h \equiv \sqrt{K/g_m H^2}$, which is estimated to be an order of $1 \mu\text{m}$ in $H=21.6$ mT. This length scale is larger than ξ , but smaller than ξ_d . Through the dipole interaction the z component of the l -vector is induced in that area (see Fig. 5.3(a) and red line in Fig. 5.3(e)). The mass current flows even at rest exclusively around the center (see the red line in Fig. 5.3(f)). Under rotation the z component of the l -vector in RD-ax acquires more negative component in the whole region (Fig. 5.3(c) and blue line in Fig. 5.3(e)), so that the mass current increases further (blue line in Fig. 5.3(f)). The d -texture almost remains unchanged (Fig. 5.3(d)).

5.2.2 Mermin-Ho (MH)

The MH texture does not include singularities, being the ABM state throughout the system. The l -vector is directed to the z -axis at the center, avoiding singularities. An initial configuration for the l -vector texture is

$$\begin{aligned} A_+(r, \theta) &= \frac{\Delta_A}{2} [1 + \cos \beta(r)], \\ A_0(r, \theta) &= \frac{\Delta_A}{\sqrt{2}} \sin \beta(r) e^{i\theta}, \\ A_-(r, \theta) &= \frac{\Delta_A}{2} [1 - \cos \beta(r)] e^{2i\theta}, \end{aligned} \quad (5.21)$$

where $\beta(r) = \pi r/2R$ varies linearly from 0 at the center to $\pi/2$ at the wall. Thus the l -vector points towards the z direction at the center and the radial direction at the wall. The d -vector texture could be either hb-type or ax-type.

The MH-hb is shown in Fig. 5.4 both at rest and under rotation. At rest the z component of the l -vectors is non-vanishing around the center in an anisotropic manner (as seen from Fig. 5.4(a)). The anisotropy of the l_z component in the x - y plane is understood in terms of the dipole interaction, which is shown in Fig. 5.4(c). The correlation between the l -texture and d -texture produces the anisotropic arrangements in each textural configuration. The elongated l_z component along the y direction is already explained in the previous subsection. The length scales of the l_z variation towards the x and y directions are characterized by ξ_d and R respectively. The l -vector and the associated d -vector variations along the x -axis at $y = 0$ around the center are shown schematically in Fig. 5.5. It is seen that since the l -vectors (red arrows) flare out from the center, the z component of the d -vector (blue arrows) changes the sign at $x = 0$. This configuration embedded in the hyperbolic d -texture is most advantageous by increasing the parallel portion ($\mathbf{l} \parallel \mathbf{d}$) due to the dipole interaction. Since this structure is characterized by the winding number combination $(w_+, w_0, w_-) = (0, 1, 2)$, it yields the spontaneous mass current at rest (red lines in Fig. 5.4(d)). Thus MH has polarity which breaks the symmetry for $\pm \Omega$ under rotation, and $j_\theta(x, y = 0)$ is larger than $j_\theta(x = 0, y)$ around the center, and this relation is reversed in the outer region. Under rotation the overall configuration of the l -vector and d -vector textures are not much changed compared with those at rest. The small changes of the l_z component and j_θ are shown in Figs. 5.4(c) and 5.4(d).

As for MH-ax shown in Fig. 5.6, the overall textures for l -vector and d -vector have cylindrical symmetry. Note that the winding number combination $(0, 1, 2)$ is the same as before. The l -vectors and d -vectors around the center whose length scales are characterized by ξ_d and ξ_h , respectively. These two length scales also appear in j_θ as clearly seen from Fig. 5.6(d), where the sharp rise corresponds to ξ_h and the maximum position to ξ_d . The l_z component in Fig. 5.6(c) shows gradual changes characterized by ξ_d . The external rotation hardly changes these features.

5.2.3 Pan-Am texture

The l -texture in Pan-Am (PA) is characterized by the two singularities at the wall as shown schematically in Fig. 5.1. In order to stabilize the PA we start with the initial configuration

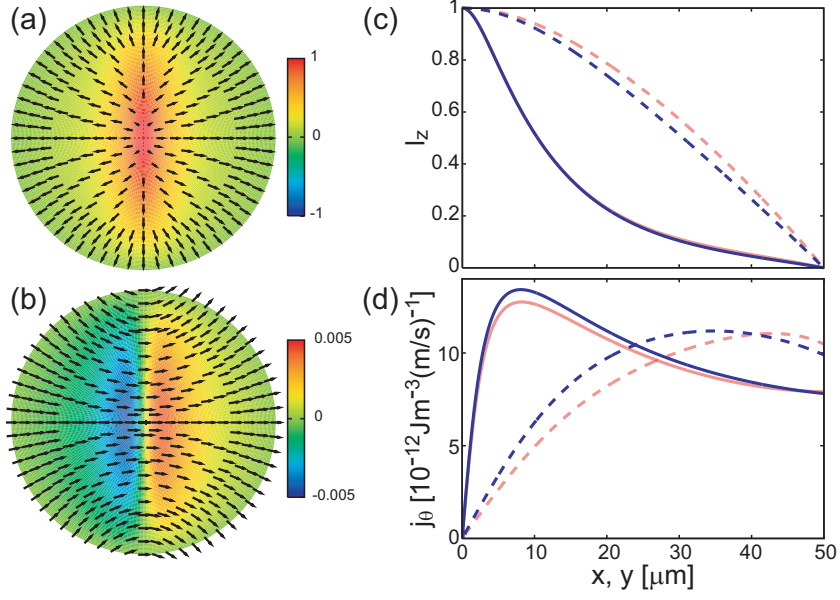


Figure 5.4: Stable textures and current for MH-hb under $R=50 \mu\text{m}$ and $T/T_c = 0.95$. (a) l -vector and (b) d -vector textures at rest. The arrows indicate the x - y component and color codes denote its z component. (c) The z component of the l -vector and (d) the current j_θ along the radial direction r from the center. The red lines are at rest and blue lines are $\Omega=3 \text{ rad/s}$. The solid (dashed) lines are along x - (y -)axis.

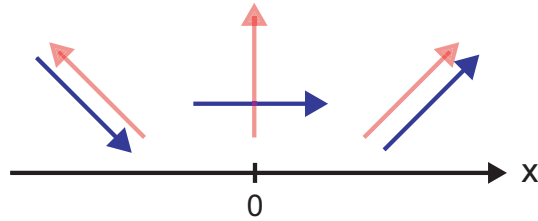


Figure 5.5: Arrangements of the l -vectors (red arrows) and d -vectors (blue arrows) for the MH-hb are shown schematically. The three pairs of arrows show schematically the variations along the x -axis around the center. Note that the angle between the d -vectors and the x -axis is exaggerated.

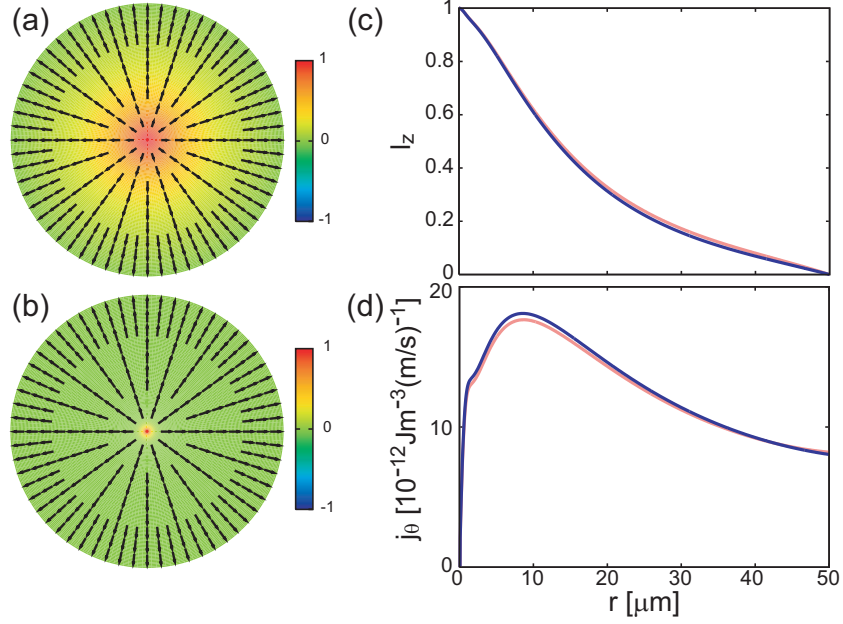


Figure 5.6: Textures and current for MH-ax under $R=50 \mu\text{m}$ and $T/T_c = 0.95$. (a) l -vector and (b) d -vector textures at rest. The arrows indicate the x - y component and color codes denote its z component. (c) The z component of the l -vector and (d) the current j_θ along the radial direction r from the center. The red lines are at rest and blue lines are $\Omega=3 \text{ rad/s}$.

given by

$$\begin{aligned}
 A_+(r, \theta) &= -\frac{\Delta A}{2}(\sin \alpha - i \cos \alpha), \\
 A_0(r, \theta) &= i \frac{\Delta A}{\sqrt{2}}, \\
 A_-(r, \theta) &= \frac{\Delta A}{2}(\sin \alpha + i \cos \alpha),
 \end{aligned} \tag{5.22}$$

with

$$\tan \alpha(r, \theta) = -\frac{r^2 \sin 2\theta}{R^2 + r^2 \cos 2\theta},$$

where R is the radius of the system. The angle $\tan \alpha$ diverges at $(r, \theta) = (R, \pm\pi/2)$. At those positions the OP amplitudes A_\pm must be zero so that those are avoided. Around those points the phase windings are $(w_+, w_0, w_-) = (-1, 0, 1)$. Therefore those are analogous to the RD in the phase structure because the singularity at the center in RD is regarded to be split into two in PA.

We show here the stabilized PA structure for small size system $R=20 \mu\text{m}$ in Fig. 5.7 where the l -vector and d -vector structures are displayed. From Fig. 5.7(a) the l -vectors tend to curve near the wall to satisfy the boundary condition, which causes the curving of the d -vectors shown in Fig. 5.7(b), otherwise they are straight pointing to the x direction. We notice that the energy of this PA is higher than the previous four kinds of the textures mentioned above. This is also true for smaller systems with different R 's.

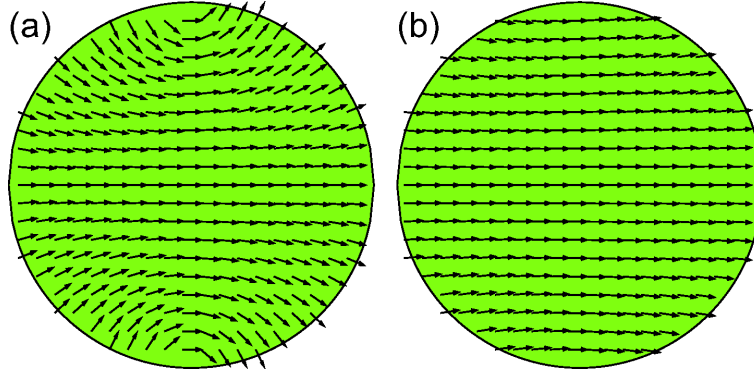


Figure 5.7: (a) l -vector and (b) d -vector textures at rest for PA-hb under $R=20 \mu\text{m}$ and $T/T_c = 0.95$. The arrows indicate the x - y component.

5.3 Size-dependence and magnetic field effects

5.3.1 Size-dependence and the critical rotation speed

We show the free energy of four textures, which are RD-hb (solid line), RD-ax (dotted line), MH-hb (dashed line) and MH-ax (dot-dash line), in Fig. 5.8 for $R=50 \mu\text{m}$, $R=115 \mu\text{m}$ and intermediate radius systems at rest.

The most stable texture for the $R=50 \mu\text{m}$ system is the RD-hb. The reasons are understood by the following. First we compare the free energy of the RD-hb with the MH-hb. The RD-hb is advantageous from the view point of the dipole energy because the l -vectors lie in the x - y plane together with the d -vectors. The winding numbers of the RD-hb are $(w_+, w_0, w_-) = (-1, 0, 1)$, so that the superflow velocity due to the phase gradient of the plus and the minus components is canceled. In contrast, since the winding numbers of the MH-hb are $(w_+, w_0, w_-) = (0, 1, 2)$, the MH-hb has the spontaneous current comprising of the superflow velocity. Consequently the MH-hb costs the gradient energy at rest. On the other hand, the RD-hb costs the condensation energy because the polar core with the radius ξ exists at the center of the cylinder. Nevertheless, since the polar core is small enough compared with the system size, the RD-hb is more stable than the MH-hb.

Next we compare the free energy of the RD-hb with the RD-ax. The gradient energy is favorable for the RD-hb since the d -vectors are almost uniform except near the wall. In addition, the magnetic field energy is gained because the d -vectors lie in the x - y plane on application of the magnetic field toward z direction. On the other hand, the RD-ax is gained by the dipole energy because the d -vectors are parallel to the l -vectors except with the radius ξ_h around the center of the cylinder. Nevertheless, since the dipole-unlocked (the l -vectors do not parallel the d -vectors) regions are small for the RD-hb, as well, the RD-hb is more stable than the RD-ax. For the same reason, the MH-hb is more stable than the MH-ax, and also the RD-hb is more stable than the MH-ax. Therefore the RD-hb is the most stable texture for the $R=50 \mu\text{m}$ system at rest.

The most stable texture becomes the RD-ax for the $R=115 \mu\text{m}$ system. The reason is that the dipole-unlocked regions enlarge by increasing the system size for the RD-hb, whereas the regions of the RD-ax characterized by the magnetic coherence length ξ_h are almost constant. That is, the RD-ax is stabilized by the dipole energy for larger systems. Similarly the stability between the MH-ax and the MH-hb is interchanged.

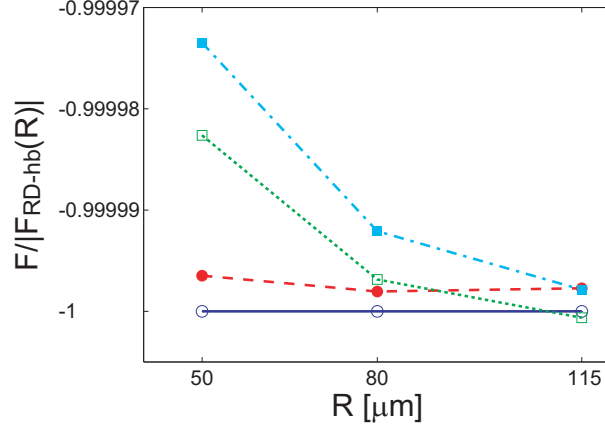


Figure 5.8: Size dependences of the free energies for various textures at rest. For $R=50 \mu\text{m}$ RD-hb (solid line) is stable while for $R=115 \mu\text{m}$ RD-ax (dotted line) becomes stable. The other lines show MH-hb (dashed line) and MH-ax (dot-dash line).

Under rotation, the MH textures are stable because they have the spontaneous current and they are tolerable under rotation compared with the RD textures which have very little spontaneous current. The external rotation drives the RD-hb into the MH-hb for the $R=50 \mu\text{m}$ system. Similarly the most stable texture RD-ax for the $R=115 \mu\text{m}$ system at rest changes into MH-hb by the rotation. Therefore l -texture and d -texture change at the critical rotation speed.

The rotational speed changing the most stable l -texture from the RD to the MH is defined as critical rotation speed Ω_c . The Ω_c obtained from the numerical calculations for the systems with the various radii R is shown as solid circles in Fig. 5.9. The RD is the most stable l -texture from the $R=5 \mu\text{m}$ to the $R=115 \mu\text{m}$ systems at rest, and the MH-hb is the most stable texture under rotation. The Ω_c decreases with increasing the radius of the systems. The numerical results of the Ω_c curve upward compared with the dashed line, which is proportional to $R^{-2.5}$. Therefore it is concluded that the RD is the most stable texture up to the $R \rightarrow \infty$ systems at rest. Note that the results are obtained under the high magnetic field. It has been pointed out by Buchholtz and Fetter [75, 76] that the RD is more favorable when the radius R of the systems becomes large.

5.3.2 Magnetic field effect

So far we have fixed the magnetic field at $H=21.6 \text{ mT}$, which is selected by experiments at ISSP because the NMR signals are best resolved. From the theoretical point of view it is interesting to know in what weaker field MH is realized over RD. We show the result in Fig. 5.10 where various textures are compared as a function of H for $R=50 \mu\text{m}$ and $T/T_c=0.95$. It is found that at $H=2 \text{ mT}$ MH-ax becomes stable over RD-hb beyond which RD-hb is always stable. Below the dipole magnetic field MH is expected to be stable over RD although it might be difficult to obtain good NMR signals in such a weak field. Thus for feasible magnetic field region around $H=21.6 \text{ mT}$ where sensible NMR signal is detectable, RD-hb is always stable in the narrow cylinders.

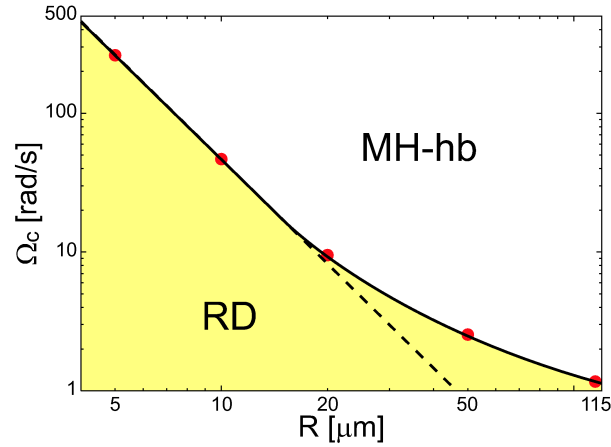


Figure 5.9: Critical rotation speed Ω_c [rad/s] versus R [μm] between RD and MH. The dashed line is proportional to $R^{-2.5}$. RD is more stable than MH at rest and low rotations for various system sizes, including $R=50 \mu\text{m}$ and $115 \mu\text{m}$.

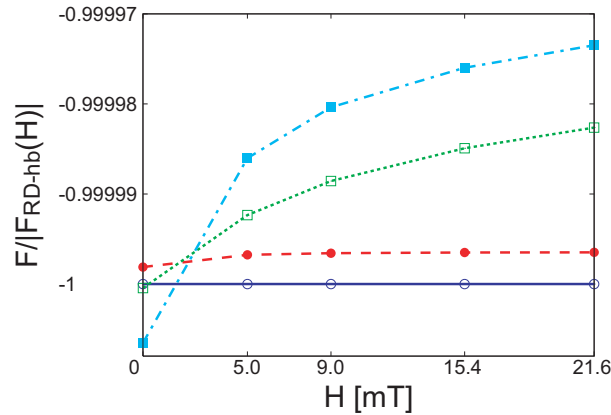


Figure 5.10: Comparison of various texture free energies as a function of the magnetic field H . The switching between RD-hb (solid line) and MH-ax (dot-dash line) occurs at $H=2$ mT. The other lines show RD-ax (dotted line) and MH-hb (dashed line).

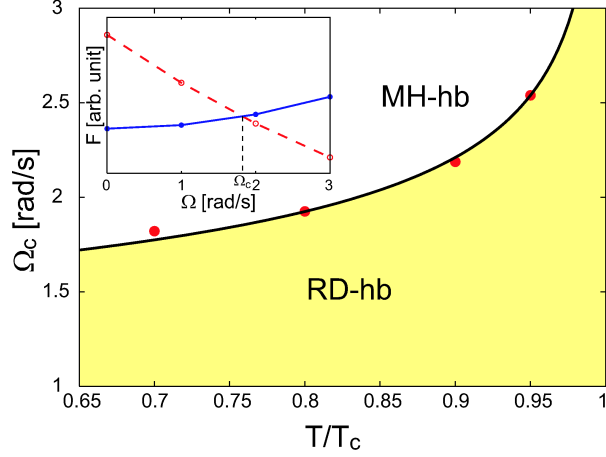


Figure 5.11: Phase diagram of critical rotation speed Ω_c (boundary line) and T/T_c ($R=50 \mu\text{m}$). At rest RD-hb is always stable. The inset shows an example of the energy crossing between RD-hb (solid line) and MH-hb (dashed line) at $T/T_c = 0.7$, showing $\Omega_c=1.8 \text{ rad/s}$.

5.4 Analysis of experiments

5.4.1 $R=50 \mu\text{m}$

In Fig. 5.11 we plot the critical rotation speed Ω_c as a function of temperature T/T_c for $R=50 \mu\text{m}$ case. At rest RD-hb is always stable over MH-hb. Upon increasing Ω , MH-hb becomes stable at Ω_c , which is an increasing function of T/T_c because the gradient energy outside the core $\sim \ln R/\xi$ becomes lower as approaching T_c where ξ is longer. The reason why MH-hb is advantageous over RD-hb under rotation is that MH-hb has the spontaneous current, in contrast, RD-hb has no spontaneous current. These characteristics are seen in the inset of Fig. 5.11.

NMR spectroscopy can be used to identify different topological objects of rotating superfluid ^3He A-phase [94], namely it can be used to identify texture in a narrow cylinder. The dipole-locked ($\mathbf{l} \parallel \mathbf{d}$) and $\mathbf{d} \perp \mathbf{H}$ regions occupying most of the condensates in the cylinder yields the main peak of NMR spectra. In the high field limit its frequency is given by [95, 34, 2]

$$\omega_t^2 = \omega_L^2 + \omega_l^2. \quad (5.23)$$

where $\omega_L = \gamma H$ is the Larmor frequency and ω_l is the longitudinal resonance frequency of the ^3He A-phase. The regions where the \mathbf{d} -vectors are dipole-unlocked and deviate from the perpendicular direction to the field, generate the small satellite peaks. The resonance frequency of a satellite is expressed in terms of a relative frequency shift R_t^2 , defined by the equation

$$\omega_t^2 = \omega_L^2 + R_t^2 \omega_l^2. \quad (5.24)$$

Therefore the texture in a narrow cylinder is identified by finding R_t^2 .

In experiment of the NMR spectroscopy for various temperatures a satellite peak with $R_t^2 \simeq 0.8$ is observed at rest [80]. The value of R_t^2 corresponds approximately to that by the

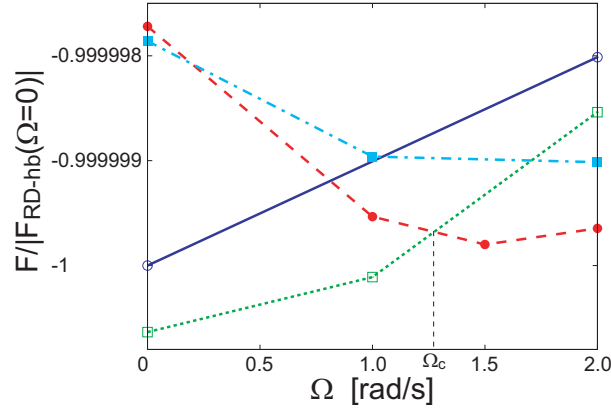


Figure 5.12: Free energy comparison of various textures for $R=115 \mu\text{m}$. RD-ax (dotted line) changes to MH-hb (dashed line) at $\Omega_c=1.3 \text{ rad/s}$. The other lines show RD-hb (solid line) and MH-ax (dot-dash line).

RD-hb [96]. In the case of PA-hb, since the radius of the cylinder is much larger than the dipole coherence length, the d -vector should be parallel to the l -vector whose region occupies the large part of the cylinder. Therefore, PA-hb shows $R_t^2 \simeq 1.0$. We also notice that RD-ax gives $R_t^2 \simeq 1.0$ because a small area around the center of the cylinder with a radius ξ_h contributes to satellite peaks. Consequently, the realized texture is definitely RD-hb, neither PA-hb nor RD-ax. Upon increasing Ω , RD-hb changes into MH-hb. This texture has been identified previously by Takagi [82] who has calculated $R_t^2 \simeq 0.3$ for MH-hb.

The precise determination of the temperature dependence of $\Omega_c(T)$ is under way experimentally. Thus it is unable to check our prediction shown in Fig. 5.11 at this time. We emphasize here, however, that the NMR spectra at low Ω and high Ω are distinctively different, therefore it is clear that the phase transition between two textures RD-hb and MH-hb occurs.

Experimentally [81] there is no hysteresis for $\pm\Omega$, indicating that the texture at rest has no polarity to the direction of rotation. This is in agreement with our identification of RD-hb for $R=50 \mu\text{m}$, which has no polarity.

5.4.2 $R=115 \mu\text{m}$

As shown in previous section, for the system size $R=115 \mu\text{m}$ the ground state texture at rest is RD-ax which is stabler than MH-hb. The critical rotation speed $\Omega_c=1.3 \text{ rad/s}$ at $T/T_c=0.95$ is calculated as shown in Fig. 5.12. The value of Ω_c roughly coincides with the ISSP experiment [79].

Experimentally there is a large hysteresis behavior about $\pm\Omega$ centered at $\Omega=0$ [78], which is contrasted with $R=50 \mu\text{m}$ case mentioned above. This is understood because RD-ax has polarity where l -vectors and d -vectors point to one of the directions $\pm z$ -axis around the center which breaks $\pm\Omega$ symmetry. We notice that PA-hb has no polarity.

As for the NMR spectrum at rest, they observe no distinctive satellite feature for $R=115 \mu\text{m}$ [80]. These facts do not contradict our identification of RD-ax, which is $R_t^2 \sim 1.0$. Thus we expect no satellite feature for RD-ax.

5.5 Summary

Let us discuss the experimental facts (1)-(4) introduced in the first of this chapter.

(1) We have identified the unknown texture as RD-hb for 50 μm sample and RD-ax for 115 μm sample at rest and lower rotations by finding the most stable texture in those conditions.

(2) Upon increasing the rotation, we found that RD changes into MH where MH was identified before by NMR resonance shape unambiguously [78] for 115 μm sample under rotations. This is confirmed by the present calculation. Namely, we precisely determined the critical rotation speed Ω_c from RD to MH for two samples.

(3) Under further higher rotation speeds multiple MH texture is expected to appear, that is, CUV. The estimated $\Omega \sim 16$ rad/sec for $R=50$ μm [77] is too high to attain in the present rotation cryostat in ISSP, whose maximum speed is 11.5 rad/s.

(4) Our identifications of RD-hb for $R=50$ μm and RD-ax for $R=115$ μm are perfectly matched with the experimental facts that in the former (latter) there does not exist (do exist) the hysteresis under the $\pm\Omega$ rotations, namely, the former texture RD-hb has no polarity and can change continuously under the reversal of the rotation sense. In contrast, RD-ax has a definite polarity because the d -vectors point to the negative z direction for the counter clock-wise rotation, which never continuously change into the positive z direction when the rotation sense is reversed, leading to a hysteresis phenomenon.

As for the possibility of the PA texture which has not been calculated for the same sizes with the experimental systems, the PA texture is not realized by the following reasons: (a) For the $R=50$ μm system the satellite position $R_t^2 \simeq 1.0$ for the PA texture differs from the observed one $R_t^2 \simeq 0.8$ [80]. (b) For the $R=115$ μm system the polarity is observed [78] while the PA texture has no polarity.

Here we have adopted the specular boundary condition, assuming that the parallel components of the quasi-particle momentum to the wall are not affected at the wall. This may not be the realistic experimental situation. However, we should point out that, experimentally, the coating the wall with ^4He atoms does not change the experimental results mentioned above [80]. Theoretically, the competition between RD and MH textures does not depend on the choice of the boundary conditions, either specular or diffusive, because near the wall two textures have the same OP structures.

Because of these facts, we conclude that the un-identified texture at rest and lower rotations confined in narrow cylinders is RD texture. Physically RD texture with the polar core at the center confined in a narrow cylinder under fields becomes energetically advantageous over MH, which is characterized by having the A-phase everywhere. In order to confirm our identification, we point out several experiments:

(A) The most important prediction is the critical rotation $\Omega_c(T)$ shown in Fig. 5.11 for $R=50$ μm . As for $R=115$ μm , $\Omega_c=1.3$ rad/s at $T/T_c = 0.95$ shown in Fig. 5.12. This can be detected by the change of NMR spectrum because RD and MH exhibit different spectral features [94].

(B) It might be quite interesting to control the texture by tuning the magnetic field H as shown in Fig. 5.10. By lowering H , MH becomes stable at rest. This controllability by H should be utilized to identify textures, and furthermore be used for realization of exotic and unexplored physics associated with multi-component superfluidity, such as Majorana particle in parallel plates [97, 42].

(C) l -vectors in RD-hb and MH-hb, which do not point perfectly to the radial direction, exhibit a distortion or in-plane twisting as seen from Figs. 5.2(a) and 5.4(a). This ultimately leads to the mass current along the rotation axis; the z -direction. This non-trivial bending current ($\propto \nabla \times \mathbf{l}$) should be tested in a future experiment.

Chapter 6

Superfluid ^3He in a slab

In this chapter, we discuss the Majorana excitations in the superfluid ^3He A- and B-phases confined in a slab. In the slab geometry, both the A- and B-phases are stabilized by changing thickness and temperature even at zero pressure [98, 99]. Therefore, we can deal with the A- and B-phases by the quasi-classical theory within the weak-coupling limit. Here, we introduce several systems of the slab geometry. By Bennett *et al.*, [100] the superfluid ^3He is confined in a thin slab box with a thickness $D = 0.6 \mu\text{m}$ and an area of the base $10 \text{ mm} \times 7 \text{ mm}$. The thickness is of the order of $10\xi_0$ at $P = 0$, where ξ_0 is the coherence length at $T = 0$. At ISSP, University of Tokyo [44], sample disks with a thickness $D = 12.5 \mu\text{m}$, which is of the order of the dipole coherence length, and a diameter 3 mm are used. The ISSP group can rotate the sample disks with the highest speed in the world and investigates half-quantum vortices. At RIKEN [101], the inter-digitated capacitors are used for making a film of the superfluid ^3He . The group can control thicknesses of the film from 0.3 to $4 \mu\text{m}$.

Our aim is to propose a concrete experimental design to detect the Majorana excitations based on quantitative calculations and understand systematically how to observe the Majorana excitations in the superfluid ^3He A- and B-phases. The quantitative calculations are performed by quasi-classical theory which yields information of quasi-particles (QPs). The quasi-classical theory is valid when $\Delta/E_F \ll 1$, where Δ is superfluid gap and E_F is the Fermi energy. Since $\Delta/E_F \sim 10^{-3}$, the theory is appropriate for the superfluid ^3He [102]. The quasi-classical framework is well established within the weak-coupling limit. The superfluid ^3He at the lower pressure can be described within the weak-coupling scheme [88] without delicate strong-coupling corrections.

Under those experimental situations, we consider the surface states from not only the upper and lower surfaces in a slab but also the side edges including the corners and evaluate the dependence of the Majorana state on the thickness of a slab. By the quasi-classical calculation, we show the “Dirac valley” (Fig. 6.1(a)) for the A-phase at the side edges. In the B-phase, several groups have demonstrated that the Majorana fermion surface state has the dispersion of $E = (\Delta/k_F) |\mathbf{k}_\parallel|$ with the surface perpendicular to the z -axis [65, 66, 68], where k_F is the Fermi wave number and $\mathbf{k}_\parallel = (k_x, k_y)$. This implies that the surface state consists of a single Majorana cone. We show the Majorana cone (Fig. 6.1(b)) by the quasi-classical calculation for a thick slab and investigate the variation of the dispersion by the thickness of a slab (Fig. 6.1(c)). The zero energy state at the corner is also discussed.

The arrangement of this chapter is as follows: In Sec. 6.1, we formulate the quasi-classical theory based on the quasi-classical Green’s function which gives quantitative information of QPs. We explain numerical methods in Sec. 6.2, which is supplemented by the symmetry

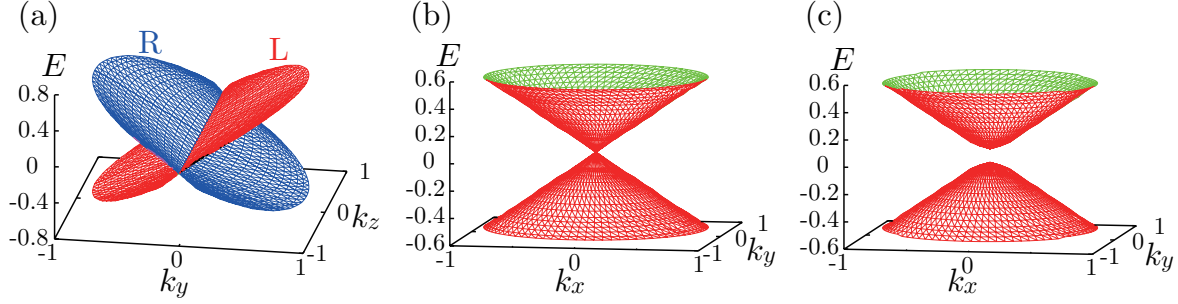


Figure 6.1: Stereographic views of typical dispersion relation. (a) Dirac valley for the A-phase in a thin slab $D = 8\xi_0$ at the left side edge “L” and the right side edge “R”. (b) Majorana cone for the B-phase in a thick slab $D = 30\xi_0$ at the upper or lower surface. (c) Split Majorana cone for the B-phase in a thin slab $D = 14\xi_0$ at the upper or lower surface. The units of energy and wave length are $\pi k_B T_c$ and k_F , respectively.

considerations of the quasi-classical Green’s function given in Appendix A. In Secs. 6.3 and 6.4 for the A- and B-phases, we show results of the spatial structures of the order parameter (OP), the current distribution, and the local density of states (LDOS) for QPs which relates to the Majorana modes. In Sec. 6.5, we discuss difference of the Majorana zero modes in the A- and B-phase and propose several experimental designs to observe the Majorana nature. In addition, we discuss the Majorana zero mode in the stripe phase. The final section is devoted to a summary.

6.1 Quasi-classical theory and order parameter

We start with the quasi-classical spinful Eilenberger equation [27], which has been used for studies of the superfluid ${}^3\text{He}$ [103, 104, 99]. The low energy excitation modes at the surface are discretized in the order of $\Delta/(k_F L)$ [64], where L is a length of the system. If L is a macroscopic length, which is much larger than k_F^{-1} , the low energy excitation modes at the surface can be regarded as continuous spectra. Because there is the exact zero energy excitation at the surface of the superfluid ${}^3\text{He}$ A-phase [64, 21] and B-phase [65, 66, 68], the quasi-classical theory can be used to discuss the Majorana QP.

The quasi-classical Green’s function $\hat{g}(\mathbf{r}, \mathbf{k}, \omega_n)$ is calculated using the Eilenberger equation

$$-i\hbar v(\mathbf{k}) \cdot \nabla \hat{g}(\mathbf{r}, \mathbf{k}, \omega_n) = \left[\begin{pmatrix} i\omega_n \hat{1} & -\hat{\Delta}(\mathbf{r}, \mathbf{k}) \\ \hat{\Delta}(\mathbf{r}, \mathbf{k})^\dagger & -i\omega_n \hat{1} \end{pmatrix}, \hat{g}(\mathbf{r}, \mathbf{k}, \omega_n) \right], \quad (6.1)$$

where the “ordinary hat” indicates the 2×2 matrix in spin space and the “wide hat” indicates the 4×4 matrix in Nambu and spin spaces. The quasi-classical Green’s function is described in Nambu space by

$$\hat{g}(\mathbf{r}, \mathbf{k}, \omega_n) = -i\pi \begin{pmatrix} \hat{g}(\mathbf{r}, \mathbf{k}, \omega_n) & i\hat{f}(\mathbf{r}, \mathbf{k}, \omega_n) \\ -i\hat{f}(\mathbf{r}, \mathbf{k}, \omega_n) & -\hat{g}(\mathbf{r}, \mathbf{k}, \omega_n) \end{pmatrix}, \quad (6.2)$$

with the direction of the relative momentum of a Cooper pair \mathbf{k} , the center-of-mass coordinate of a Cooper pair \mathbf{r} , and the Matsubara frequency $\omega_n = (2n + 1)\pi k_B T$. The quasi-classical

Green's function satisfies a normalization condition $\hat{g}^2 = -\pi^2 \hat{1}$. The Fermi velocity is given as $\mathbf{v}(\mathbf{k}) = v_F \mathbf{k}$ on the three dimensional Fermi sphere.

We solve Eq. (6.1) by the Riccati method [29, 28, 99]. We introduce Riccati amplitude $\hat{a} = (\hat{1} + \hat{g})^{-1} \hat{f}$ and $\hat{b} = (\hat{1} + \hat{g})^{-1} \hat{f}$ related to particle- and hole-like projections of the off-diagonal propagators, respectively. Equation (6.1) can be rewritten as Riccati equations

$$\begin{aligned} \hbar \mathbf{v}(\mathbf{k}) \cdot \nabla \hat{a}(\mathbf{r}, \mathbf{k}, \omega_n) &= \hat{\Delta}(\mathbf{r}, \mathbf{k}) - \hat{a}(\mathbf{r}, \mathbf{k}, \omega_n) \hat{\Delta}(\mathbf{r}, \mathbf{k})^\dagger \hat{a}(\mathbf{r}, \mathbf{k}, \omega_n) - 2\omega_n \hat{a}(\mathbf{r}, \mathbf{k}, \omega_n), \\ -\hbar \mathbf{v}(\mathbf{k}) \cdot \nabla \hat{b}(\mathbf{r}, \mathbf{k}, \omega_n) &= \hat{\Delta}(\mathbf{r}, \mathbf{k})^\dagger - \hat{b}(\mathbf{r}, \mathbf{k}, \omega_n) \hat{\Delta}(\mathbf{r}, \mathbf{k}) \hat{b}(\mathbf{r}, \mathbf{k}, \omega_n) - 2\omega_n \hat{b}(\mathbf{r}, \mathbf{k}, \omega_n). \end{aligned} \quad (6.3)$$

The equations are solved by integration toward \mathbf{k} for $\hat{a}(\mathbf{r}, \mathbf{k}, \omega_n)$ and toward $-\mathbf{k}$ for $\hat{b}(\mathbf{r}, \mathbf{k}, \omega_n)$. From the Riccati amplitude, the quasi-classical Green's function is given as

$$\hat{g} = -i\pi \begin{pmatrix} (\hat{1} + \hat{a}\hat{b})^{-1} & 0 \\ 0 & (\hat{1} + \hat{b}\hat{a})^{-1} \end{pmatrix} \begin{pmatrix} \hat{1} - \hat{a}\hat{b} & 2i\hat{a} \\ -2i\hat{b} & -(\hat{1} - \hat{b}\hat{a}) \end{pmatrix}. \quad (6.4)$$

The self-consistent condition for the pair potential $\hat{\Delta}(\mathbf{r}, \mathbf{k})$ is given as

$$\hat{\Delta}(\mathbf{r}, \mathbf{k}) = N_0 \pi k_B T \sum_{-\omega_c \leq \omega_n \leq \omega_c} \left\langle V(\mathbf{k}, \mathbf{k}') \hat{f}(\mathbf{r}, \mathbf{k}', \omega_n) \right\rangle_{\mathbf{k}'}, \quad (6.5)$$

where N_0 is the density of states in the normal state, ω_c is a cutoff energy setting $\omega_c = 40\pi k_B T_c$ with the transition temperature T_c in a bulk, and $\langle \dots \rangle_{\mathbf{k}}$ indicates the Fermi surface average. The pairing interaction $V(\mathbf{k}, \mathbf{k}') = 3g_1 \mathbf{k} \cdot \mathbf{k}'$ for Cooper pairs with an orbital angular momentum $L = 1$, where g_1 is a coupling constant. In our calculation, we use a relation

$$\frac{1}{g_1 N_0} = \ln \frac{T}{T_c} + 2\pi k_B T \sum_{0 \leq \omega_n \leq \omega_c} \frac{1}{\omega_n}. \quad (6.6)$$

Spin-triplet OP is defined by a vectorial notation

$$\hat{\Delta}(\mathbf{r}, \mathbf{k}) = (i\hat{\sigma} \hat{\sigma}_y) \cdot \mathbf{\Delta}(\mathbf{r}, \mathbf{k}), \quad (6.7)$$

with the Pauli matrix $\hat{\sigma}$ in spin space. The complex vector $\mathbf{\Delta}$ is perpendicular to the spin \mathbf{S} of a Cooper pair, namely, $\mathbf{\Delta} \cdot \mathbf{S} = 0$. The $\mathbf{\Delta}$ can be expanded in orbital momentum directions,

$$\Delta_\mu(\mathbf{r}, \mathbf{k}) = A_{\mu i}(\mathbf{r}) k_i, \quad (6.8)$$

where $A_{\mu i}(\mathbf{r})$ is a complex 3×3 matrix with a spin index μ and an orbital index i . The repeated index implies summation over x , y , and z .

In this chapter, we discuss the chiral state in the A-phase, polar state, B-phase, and planar state. Symbolic descriptions of the OP in their state are the following: For the chiral state,

$$\mathbf{\Delta} = d_z(k_x + ik_y), \quad (6.9)$$

for the polar state,

$$\mathbf{\Delta} = d_z k_x, \quad (6.10)$$

for the B-phase,

$$\Delta = d_x k_x + d_y k_y + d_z k_z, \quad (6.11)$$

and for the planar state,

$$\Delta = d_x k_x + d_y k_y, \quad (6.12)$$

where d -vector is perpendicular to the spin of a Cooper pair. d -vector and the momentum direction are permitted to rotate spherically in the spin and momentum space, respectively.

By using the self-consistent quasi-classical Green's function, the mass and spin currents are calculated by

$$\mathbf{j}(\mathbf{r}) = mN_0\pi k_B T \sum_{-\omega_c \leq \omega_n \leq \omega_c} \langle \mathbf{v}(\mathbf{k}) \text{Im} [g_0(\mathbf{r}, \mathbf{k}, \omega_n)] \rangle_{\mathbf{k}}, \quad (6.13)$$

$$\mathbf{j}_s^\mu(\mathbf{r}) = \frac{\hbar}{2} N_0 \pi k_B T \sum_{-\omega_c \leq \omega_n \leq \omega_c} \langle \mathbf{v}(\mathbf{k}) \text{Im} [g_\mu(\mathbf{r}, \mathbf{k}, \omega_n)] \rangle_{\mathbf{k}}, \quad (6.14)$$

respectively, where m is the mass of the ^3He atom and g_μ is a component of the quasi-classical Green's function \hat{g} in spin space, namely,

$$\hat{g} = \begin{pmatrix} g_0 + g_z & g_x - ig_y \\ g_x + ig_y & g_0 - g_z \end{pmatrix}. \quad (6.15)$$

LDOS for energy E is given by

$$\begin{aligned} N(E, \mathbf{r}) &= \langle N(E, \mathbf{r}, \mathbf{k}) \rangle_{\mathbf{k}} \\ &= N_0 \langle \text{Re} [g_0(\mathbf{r}, \mathbf{k}, \omega_n)|_{i\omega_n \rightarrow E+i\eta}] \rangle_{\mathbf{k}}, \end{aligned} \quad (6.16)$$

where η is a positive infinitesimal constant and $N(E, \mathbf{r}, \mathbf{k})$ is angle-resolved LDOS. Typically, we choose $\eta = 0.003\pi k_B T_c$. For obtaining $g_0(\mathbf{r}, \mathbf{k}, \omega_n)|_{i\omega_n \rightarrow E+i\eta}$, we solve Eqs. (6.3) with $\eta - iE$ instead of ω_n under the pair potential obtained self-consistently.

6.2 System geometry and numerical methods

We consider a cross-section A of a slab with a thickness of D along the z -direction and a macroscopic length of L along the x -direction, shown in Fig. 6.2(a). It is assumed that the quasi-classical Green's function and OP are homogeneous along the y -direction. We also assume that the surfaces of the slab are specular, where specularity is controlled by coating the surface with ^4He atoms [105]. Under the boundary condition, the quasi-classical Green's function or the Riccati amplitude changes only the direction of the relative momentum by mirror reflection at a surface \mathbf{R}_{surf} , namely, $\hat{g}(\mathbf{R}_{\text{surf}}, \mathbf{k}, \omega_n) = \hat{g}(\mathbf{R}_{\text{surf}}, \underline{\mathbf{k}}, \omega_n)$ or $\hat{a}(\mathbf{R}_{\text{surf}}, \mathbf{k}, \omega_n) = \hat{a}(\mathbf{R}_{\text{surf}}, \underline{\mathbf{k}}, \omega_n)$ and $\hat{b}(\mathbf{R}_{\text{surf}}, \mathbf{k}, \omega_n) = \hat{b}(\mathbf{R}_{\text{surf}}, \underline{\mathbf{k}}, \omega_n)$, where $\underline{\mathbf{k}} = \mathbf{k} - 2\mathbf{n}(\mathbf{n} \cdot \mathbf{k})$ with a unit vector \mathbf{n} which is perpendicular to the surface.

We solve Eqs. (6.3) by the numerical integration toward the \mathbf{k} -direction for \hat{a} and toward the $-\mathbf{k}$ -direction for \hat{b} from the surface to the position \mathbf{r} . Since $\hat{a}(\mathbf{R}_{\text{surf}}, \mathbf{k}, \omega_n) = \hat{a}(\mathbf{R}_{\text{surf}}, \underline{\mathbf{k}}, \omega_n)$, the initial value of \hat{a} at a surface \mathbf{R}_{surf} is determined by the numerical integration toward the $\underline{\mathbf{k}}$ -direction from the other surface to \mathbf{R}_{surf} . Eventually, we have to solve the numerical integration along the sufficiently long path by changing the direction from \mathbf{k}

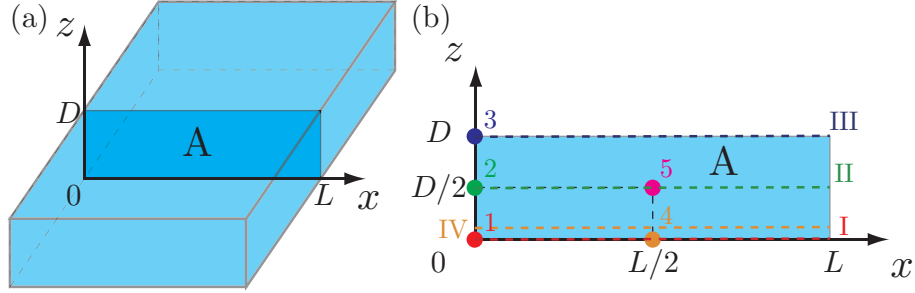


Figure 6.2: (a) A schematic configuration of a slab with a thickness of D along the z -direction and a macroscopic length of L along the x -direction. We consider a cross-section A ($0 \leq x \leq L, 0 \leq z \leq D$). (b) Indexes of positions in the cross-section A. We label $(x, z) = (0, 0), (0, D/2), (0, D), (L/2, 0),$ and $(L/2, D/2)$ as “1”, “2”, “3”, “4”, and “5”. Paths $z = 0, z = D/2, z = D,$ and $z = 0.5\xi_0$ along the x -axis are labeled as “I”, “II”, “III”, and “IV”.

to \underline{k} at the surface so that the integration path gives the same value of \hat{a} under arbitrary initial values, and also \hat{b} . Since the integration path changes the direction at the surface, simple calculation is difficult. For overcoming the difficulty, we exploit that the change in the direction of the integration path from \underline{k} to \underline{k} can be regarded as the change in the relative momentum of the pair potential from \underline{k} to \underline{k} . For example, we can substitute $-A_{\mu x}$ for $A_{\mu x}$ in the pair potential instead of the reflection of the integration paths at a surface $x = 0$. Similarly for the other surfaces, we can integrate Eqs. (6.3) along the straight long paths in the region connected to the antiperiodic pair potential infinitely.

We calculate the quasi-classical Green’s function in a range $-L/2 \leq x \leq L/2$ and $-D/2 \leq z \leq D/2$ instead of a cross-section A ($0 \leq x \leq L, 0 \leq z \leq D$) to reduce computational time. We show the reduction method in Appendix A in addition to other reduction methods with the symmetry of the quasi-classical Green’s function.

6.3 A-phase

We discuss here the situation in which the thickness of a slab D is changed, where the A- and B-phases are stable in thin and thick slabs, respectively. [99] We present the calculated results of OP, LDOS, and mass current for the A-phase and spin current for the B-phase at $T = 0.2T_c$. In each phase, the results depend on the thickness D . The length of the cross-section A is taken as $L = 40\xi_0$ throughout the paper where the OP is recovered to the bulk value at the center of the system. Note that the following results are unchanged for the length L longer than $40\xi_0$. In addition, we consider the low pressure limit $P \rightarrow 0$ within the weak-coupling limit. The spatial positions of the results are indicated by the indexes in Fig. 6.2(b). In this section and next section, we use the units $\xi_0 = \hbar v_F / 2\pi k_B T_c$, $\pi k_B T_c$, and N_0 for length, energy, and LDOS, respectively.

The bulk of the A-phase is in the chiral state. The OP in the chiral state is described by [2]

$$A_{\mu i} = d_{\mu}(\mathbf{m} + i\mathbf{n})_i,$$

where m -vector and n -vector are perpendicular to each other. l -vector, which signifies the

orbital chirality, is defined as $\mathbf{l} \equiv \mathbf{m} \times \mathbf{n}$. At the edge of a slab, since the normal orbital component to the edge vanishes, the polar state will be realized. The OP in the polar state is described by [2]

$$A_{\mu i} = d_{\mu} m_i,$$

where we regard n -vector as perpendicular to the edge.

In a slab cell used by Bennett *et al.* [100] where the thickness is $0.6 \mu\text{m} \approx 8\xi_0$, it is expected that the A-phase is stable at $T = 0.2T_c$ [106]. Since the thickness D is much shorter than the dipole coherence length $\sim 1000\xi_0$, d -vector, which characterizes the spin state of the OP in the A-phase, points to the z -direction in the absence of a magnetic field as long as l -vector is parallel to the z -axis. l -vector is parallel to the z -axis everywhere except near the side edges at $x = 0$ and $x = L$ in the slab shown in Fig. 6.2. The length scale of the spatial variation of l -vector is short, whose order is the coherence length. On the other hand, d -vector can not vary spatially since the order of the length scale is the dipole coherence length. d -vector is spatially uniform even under a magnetic field [107]. In this chapter, we fix the direction of d -vector to the z -axis.

6.3.1 $D = 8\xi_0$: Thin slab for A-phase

For $D = 8$, the OP is described by $\Delta_z(x, \mathbf{k}) = A_{zx}(x)k_x + A_{zy}(x)k_y$, where the relative phase between A_{zx} and A_{zy} is $\pi/2$. The OP is uniform along the z -direction and varies along only the x -direction. Since the slab is thin, the k_z -component of the OP is suppressed. Note that the uniformness along the z -direction and the suppression of the k_z -component are not suppositions, but results by the self-consistent calculation. The profile of the OP along the x -axis is shown in Fig. 6.3(a). Because of the specular boundary condition, the k_x -component perpendicular to the edge becomes zero at $x = 0$ and $x = L$. In contrast, the parallel k_y -component is enhanced by compensating for the loss of the k_x -component at the edge, where the polar state is realized. The k_x -component increases and the k_y -component decreases toward the bulk region around $x = L/2$; thus, the chiral state with $k_x + ik_y$ is attained. We can construct l -vector as $l_i \equiv -i\epsilon_{ijk}A_{zj}^*A_{zk}/|\Delta|^2$, where ϵ_{ijk} is the totally antisymmetric tensor and $|\Delta|^2 = A_{zi}^*A_{zi}$ is the squared amplitude of the OP. l -vector points to the z -direction in the bulk region and vanishes at the edge. Since the chiral state is realized except at the edge, the Majorana fermion edge state $\Psi^\dagger = \Psi$ exists at side edges [54, 64].

The mass current $j_y(x)$ is shown in Fig. 6.3(b). The mass current flows circularly along the side edge of the slab. Experimental values [88] are used as coefficients of Eq. (6.13) so that a quantitative value of the mass current is obtained. By applying a magnetic field perpendicular to a slab, we can produce a spin imbalance due to the Zeeman shift between the up-up spin pairs and the down-down spin pairs. This results in a net spin current in addition to the mass current.

Figure 6.3(c) shows LDOS at the edge $x = 0$ (the position “2” in Fig. 6.2) and the bulk $x = L/2$ (“5”). It is clearly seen from the line “2” for $x = 0$ that the LDOS with a substantial weight appears at a zero energy, corresponding to the Majorana edge mode, because the distance L between the edges is macroscopic [54, 64]. This implies that the LDOS is expressed as $N(E, x = 0) = N(E = 0, x = 0) + \alpha E^2$ in the vicinity of $E = 0$. The first term comes from the Majorana edge mode, and the second term comes from the point node of the chiral state in the bulk A-phase. The peak at $E \approx 0.65$ comes from the gap of the chiral state in the bulk and the peak at $E \approx 0.8$ comes from the gap of the polar state at the edge. The LDOS at $x = L/2$ (the line “5”) shows a typical behavior of the point node

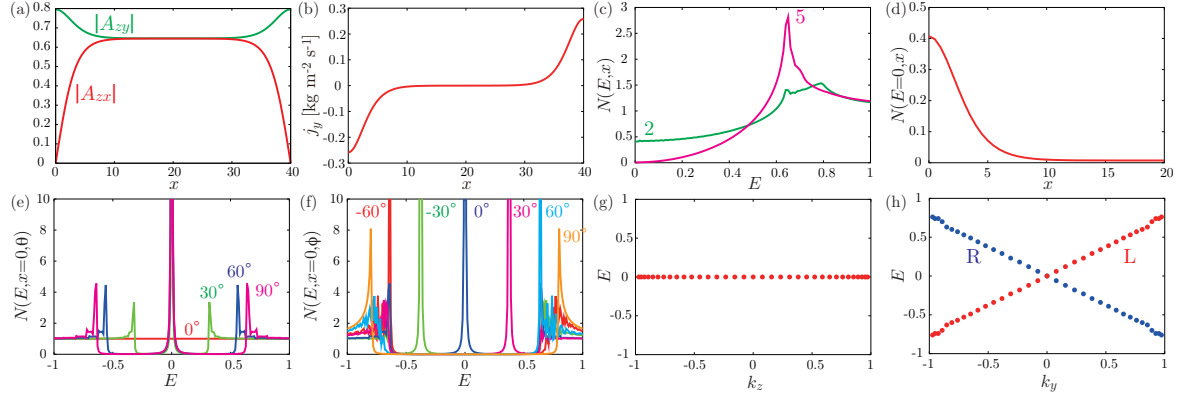


Figure 6.3: Calculated results for the A-phase with $D = 8$. Profiles of OP (a), and mass current j_y (b) along the x -axis. (c) LDOS $N(E, x)$ at “2”, and “5” defined in Fig. 6.2(b). (d) Zero energy LDOS $N(E = 0, x)$ from the edge at $x = 0$ to the bulk at $x = L/2$. Angle-resolved LDOS $N(E, x = 0, \theta)$ with $\phi = 0^\circ$ (e), and $N(E, x = 0, \phi)$ with $\theta = 90^\circ$ (f). The peak energy of angle-resolved LDOS at the side edges as a function of k_z for $k_y = 0$ (g), and as a function of k_y for $k_z = 0$ (h), where “L” (“R”) is for the left (right) edge. In this and the following figures, the units of length, energy and $A_{\mu i}$, LDOS, and wave length are ξ_0 , $\pi k_B T_c$, N_0 , and k_F , respectively.

spectrum, namely, $N(E, x = L/2) \propto E^2$. In Fig. 6.3(d) we show the extent of the Majorana edge mode at $E = 0$ toward the bulk from the edge at $x = 0$, which spreads over the order of $5\xi_0$. The spectrum of the edge gradually changes into the bulk spectrum.

The LDOS $N(E, \mathbf{r})$ is obtained by averaging the angle-resolved LDOS $N(E, \mathbf{r}, \mathbf{k})$ on the Fermi surface, which has the peak at the energy of the surface Andreev bound state. The dispersion relation of the surface Andreev bound state can be evaluated by following the peak in each momentum direction. The angle-resolved LDOS $N(E, x = 0, \theta)$ with $\phi = 0^\circ$ and $N(E, x = 0, \phi)$ with $\theta = 90^\circ$ are shown in Figs. 6.3(e) and 6.3(f), respectively, where θ is the polar angle from the k_z -axis and ϕ is the azimuthal angle from the k_x -axis on the three-dimensional Fermi sphere. The angles and momentum directions have the relations: $\tan \theta = \sqrt{k_x^2 + k_y^2}/k_z$ and $\tan \phi = k_y/k_x$. The angle-resolved LDOS is symmetric between $0^\circ \leq \theta \leq 90^\circ$ and $180^\circ \geq \theta \geq 90^\circ$, and between $-90^\circ \leq \phi \leq 90^\circ$ and $270^\circ \geq \phi \geq 90^\circ$. The zero energy peaks of the angle-resolved LDOS appear if $\phi = 0^\circ$ except for $\theta = 0^\circ$. The zero energy peaks come from the zero energy Andreev bound state of QPs at the edge. The QPs without the k_y -component have the zero energy Andreev bound state because they feel the π -phase shift of the pair potential for the relative momentum from $(k_x, k_y = 0, k_z)$ to $(-k_x, k_y = 0, k_z)$. This is clear from the Eilenberger equation (6.1) since the quasi-classical Green’s function $\hat{g}(\mathbf{k})$ depends on only the \mathbf{k} -component of the pair potential $k_x + ik_y$. The angle-resolved LDOS is asymmetric with respect to $E = 0$ (Fig. 6.3(f)) because the superfluid state in the A-phase has the chirality [61]. The asymmetric angle-resolved LDOS is related to the mass current.

The peak energy of angle-resolved LDOS at the side edges as a function of k_z for $k_y = 0$ and as a function of k_y for $k_z = 0$ is shown in Figs. 6.3(g) and 6.3(h), respectively. It is found that the energy is dispersionless along the k_z -axis and two linear dispersions appear near $E = 0$ along the k_y -axis, where each dispersion comes from the left ($x = 0$) and right ($x = L$)

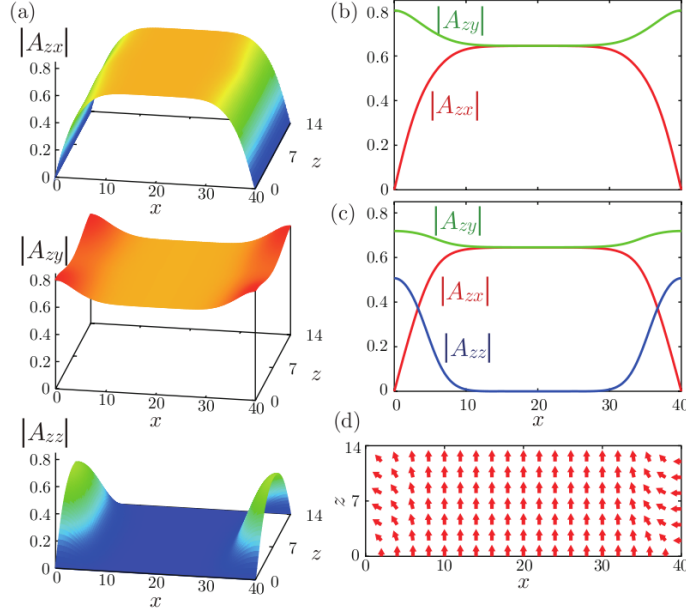


Figure 6.4: The OP for the A-phase with $D=14$. (a) Amplitude of each component. Profiles of each component along “I” (b), and along “II” (c). (d) Orientations of l -vector texture in the x - z plane of a slab.

edges. Since the directions of the mass current are different both edges, the linear dispersions have the opposite slope. The linear Dirac dispersions continue along the k_z -direction, which form a “Dirac valley”. The results are consistent with the strict quantum level structures of the Majorana fermion edge state by Bogoliubov-de Gennes equation [21].

6.3.2 $D = 14\xi_0$: Thick slab for A-phase

In a thick slab, the k_z -component of the OP is induced. For $D = 14$, the k_z -component appears near the edges at $x = 0$ and $x = L$ to avoid the polar state except at $z = 0$ and $z = D$, shown in Figs. 6.4(a)-6.4(c). The OP is described by $\Delta_z(\mathbf{r}, \mathbf{k}) = A_{zx}(\mathbf{r})k_x + A_{zy}(\mathbf{r})k_y + A_{zz}(\mathbf{r})k_z$, where the phases of A_{zz} and A_{zx} are the same and the relative phase between A_{zz} and A_{zy} is $\pi/2$. Since the thickness of $D = 14$ is small, the A_{zz} does not recover the bulk value of A_{zx} at the side edges $x = 0$ and $x = L$ along $z = D/2$ (Fig. 6.4(c)). As similarly at the edges $z = 0$ and $z = D$, l -vector is perpendicular to the edges at $x = 0$ and $x = L$ by the induced k_z -component, shown in Fig. 6.4(d).

The mass current $j_y(\mathbf{r})$ is shown in Fig. 6.5(a), and its profiles along “I” ($z = 0$), “II” ($z = D/2$), and “III” ($z = D$) are shown in Fig. 6.5(b). The mass current flows clockwise relative the local l -vector direction. The j_y from l -vector in the bulk region flows to the negative (positive) y -direction at $x = 0$ ($x = L$). At the side edges, since l -vector points to the negative x -direction, the j_y from the edges flows to the negative and positive y -directions in $z < D/2$ and $z > D/2$, respectively. Therefore, the edge mass current is strengthened in $z < D/2$ ($z > D/2$) and weakened in $z > D/2$ ($z < D/2$) at the edge $x = 0$ ($x = L$). The symmetry of the mass current between $z < D/2$ and $z > D/2$ is broken despite the symmetry of the OP.

Figure 6.5(c) shows LDOS at $(x, z) = (0, 0)$, $(0, D/2)$, $(0, D)$, and $(L/2, D/2)$. At $(0, 0)$

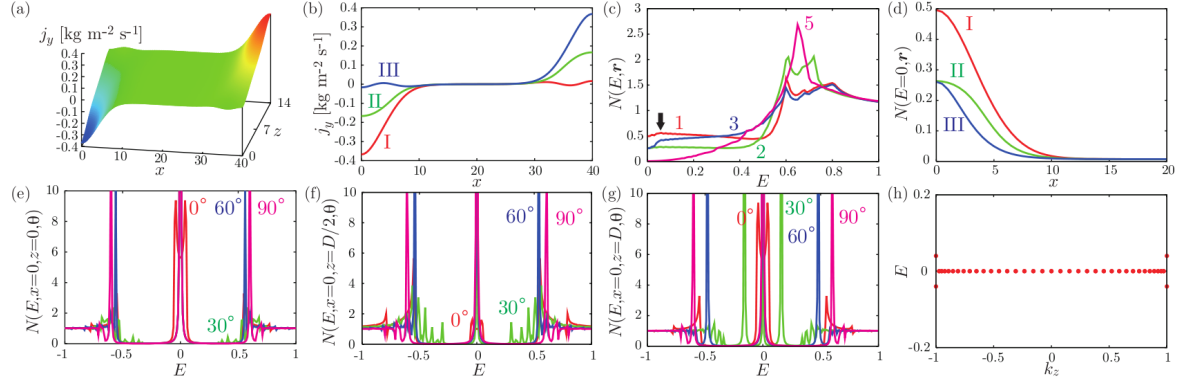


Figure 6.5: Calculated results for the A-phase with $D=14$. (a) Mass current $j_y(\mathbf{r})$ in the x - z plane. (b) Profiles of the mass current $j_y(\mathbf{r})$ along paths “I”, “II”, and “III”. (c) LDOS $N(E, \mathbf{r})$ at “1”, “2”, “3”, and “5”. (d) Zero energy LDOS $N(E=0, \mathbf{r})$ along “I”, “II”, and “III”. Angle-resolved LDOS $N(E, \mathbf{r}, \theta)$ with $\phi = 0^\circ$ at “1” (e), “2” (f), and “3” (g). (h) The peak energy of angle-resolved LDOS as a function of k_z for $k_y = 0$ at “1”.

and $(0, D)$ (the lines “1” and “3”), there are the zero energy LDOS and a small peak at a low energy indicated by the arrow in Fig. 6.5(c). Although l -vector points to the edge, the zero energy LDOS also exists at $(0, D/2)$ (the line “2”). The lines “1” and “3” are slightly decreased and increased, respectively, in low energy from the small peak as energy increases. The line “2” is almost constant in low energy. The LDOS (the lines “1”, “2”, and “3”) are enhanced sharply near $E \approx 0.5$. The LDOS at $(L/2, D/2)$ (the line “5”) shows the typical spectral behavior of the point node. In Fig. 6.5(d) we show the extent of the zero energy edge mode toward the bulk from the edge at $x = 0$. The amounts of the zero energy LDOS at $x = 0$ along $z = D/2$ and $z = D$ (the lines “II” and “III”) are smaller than that along $z = 0$ (the line “I”). The extent of the zero energy LDOS along “III” is of the order of $5\xi_0$ as in the thin slab $D = 8$; however, the zero energy LDOS along “I” and “II” are more widely extended.

The angle-resolved LDOS $N(E, \mathbf{r}, \theta)$ with $\phi = 0^\circ$ at $(0, 0)$, $(0, D/2)$, and $(0, D)$ are, respectively, displayed in Figs. 6.5(e), 6.5(f), and 6.5(g). The zero energy peaks of the angle-resolved LDOS appear except for $\theta = 0^\circ$. The peaks of the line $\theta = 0^\circ$ at the finite low energy appear from the upper and lower surfaces because the k_z -component of the pair potential is non-vanishing. Since thickness $D = 14$ is small, the original zero energy peak of $\theta = 0^\circ$ perpendicular to the upper and lower surfaces is split into the finite energy peaks, which is discussed particularly for the B-phase in next section. The splitting peaks at $(0, 0)$ are shown in Fig. 6.5(h) only at $k_z = \pm 1$ for $k_y = 0$. The finite energy peaks compose the small peak of the LDOS in the lines “1” and “3” in Fig. 6.5(c). Since the position $(0, D/2)$ is apart from the upper and lower surfaces, the energy peaks of $\theta = 0^\circ$ are small. Consequently, the peak of the LDOS at low energy is not clear (the line “2” in Fig. 6.5(c)). The point nodes of the OP near the side edges have a tilt to the x -direction according to l -vector, or the anti-nodes of the OP lie to some angles from the k_z -axis. Thus, the incident QPs from $(0, 0)$ with low angles from the k_z -axis do not feel the clear small gap in the vicinity of the point nodes. For instance, the line $\theta = 30^\circ$ in Fig. 6.5(e) should be compared with that in Fig. 6.3(e) for the thin slab $D = 8$. Therefore, the gap-like LDOS enhanced sharply near $E \approx 0.5$ appears (the line “1” in Fig. 6.5(c)). On the other hand, the incident QPs from $(0, D)$ with low angles

from the k_z -axis are reflected at the edge and regarded as with low angles from the $-k_z$ -axis. Since the QPs feel the small gap in the vicinity of the point nodes, they have the clear peaks in the angle-resolved LDOS (Fig. 6.5(g)). Therefore, the LDOS is slightly increased in low energy as energy increases (the line “3” in Fig. 6.5(c)). Since the QPs at $(0, D/2)$ have the two kinds of the characteristic momentum, the LDOS is almost constant in low energy (the line “2” in Fig. 6.5(c)).

The LDOS at the side edge is different and depends on the thickness of the slab. In the thin slab ($D = 8$), l -vector points to the z -direction everywhere and the LDOS is $N(E) = N(0) + \alpha E^2$ in low energy. In contrast, in the thick slab ($D = 14$), l -vector points to the x -direction near the side edge and the LDOS is $N(E) = N(0) + N_{\text{gap}}(E)$, where $N_{\text{gap}}(E)$ is almost zero in low energy and increases sharply near $E \approx 0.5$ like the LDOS with the full gap state. The edge mass current varies along the side edge in the thick slab, which is also a great difference with the thin slab.

Note that the A-phase is metastable in the slab with $D = 14$ at $T = 0.2T_c$ in the weak-coupling limit for $P \rightarrow 0$ [106]. In the same slab, the A-phase is stabilized at $T = 0.9T_c$ [106]; however, l -vector points to only the z -direction, because the k_z -component is absent owing to the longer coherence length at higher temperature. The mechanism is similar to that the A-phase is more stable than the B-phase, which has the k_x -, k_y -, and k_z -components, in a thin slab at low temperature. The calculated results shown in this subsection is not in free energy minimum at $P = 0$; however, the strong-coupling effect by pressure stabilizes the A-phase texture. Thus, the above characteristics from the texture will be observed at finite pressure.

6.4 B-phase

The B-phase is stable when the thickness of a slab is larger than $\approx 13\xi_0$ at $T = 0.2T_c$ [106]. The OP of the B-phase is described by [2]

$$A_{\mu i} = R_{\mu i}(\mathbf{n}_d, \theta_d) \begin{pmatrix} A_{xx} & 0 & 0 \\ 0 & A_{yy} & 0 \\ 0 & 0 & A_{zz} \end{pmatrix},$$

where $R_{\mu i}(\mathbf{n}_d, \theta_d)$ is a rotation matrix with a rotation axis \mathbf{n}_d and a rotation angle θ_d about \mathbf{n}_d . The rotation matrix gives the relative angle between the orbital momentum and the direction along which the spin of a Cooper pair is zero. The spin state is stable by the dipole-dipole interaction when $\theta_d = \theta_L \equiv \cos^{-1}(-1/4)$ and \mathbf{n}_d is perpendicular to the surface in the absence of a magnetic field [2]. If the thickness of a slab is much smaller than the dipole coherence length, \mathbf{n}_d is locked to the z -axis. Thus, we derive $A_{xx}(\mathbf{r})$, $A_{yy}(\mathbf{r})$, and $A_{zz}(\mathbf{r})$ with the uniform rotation matrix $R(\mathbf{z}, \theta_L)$. Note that the three components have the same phase.

At the surface of a slab, since the normal component to the surface of the orbital state vanishes, the planar state will be realized. The OP in the planar state is described by [2]

$$A_{\mu i} = R_{\mu i}(\mathbf{n}_d, \theta_d) \begin{pmatrix} A_{xx} & 0 & 0 \\ 0 & A_{yy} & 0 \\ 0 & 0 & 0 \end{pmatrix},$$

where we regard the z -axis as perpendicular to the edge. If $\theta_d = 0$, the OP can be written

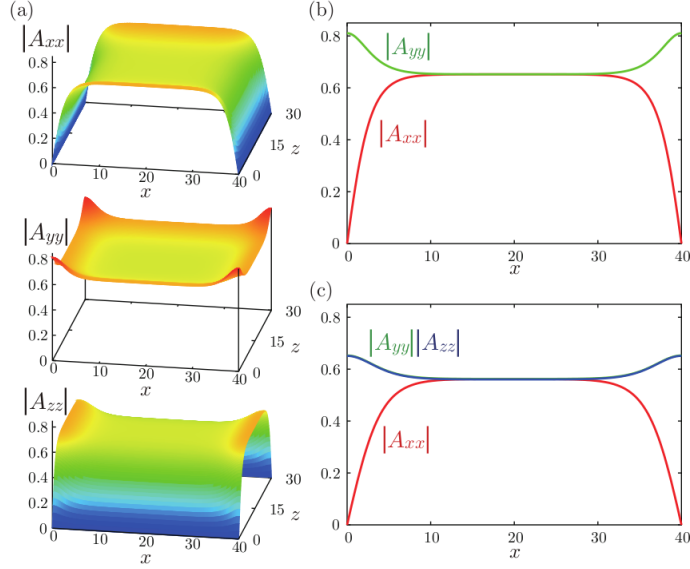


Figure 6.6: The OP for the B-phase with $D=30$. (a) Amplitude of each component. Profiles of each component along “I” (b), and along “II” (c).

by other descriptions as

$$\Delta_{\uparrow\uparrow}(\mathbf{k}) = -\Delta_p(k_x - ik_y), \quad \Delta_{\downarrow\downarrow}(\mathbf{k}) = \Delta_p(k_x + ik_y),$$

where $\Delta_{\uparrow\uparrow} = -\Delta_x + i\Delta_y$, $\Delta_{\downarrow\downarrow} = \Delta_x + i\Delta_y$, and $\Delta_p = A_{xx} = A_{yy}$. Therefore, in the planar state, $S_z = +1$ spin state has $L_z = -1$ orbital angular momentum and $S_z = -1$ spin state has $L_z = +1$ orbital angular momentum.

6.4.1 $D = 30\xi_0$: Thick slab for B-phase

We consider that the thickness of a slab is much longer than the coherence length, namely, the thickness can be regarded as macroscopic for the OP, and much shorter than the dipole coherence length. The requirement is satisfied for a thickness of $D = 30$. It is clearly seen that the component of the OP perpendicular to the edge becomes zero in Fig. 6.6(a). The polar state k_y occurs at the corner “1” ($x = 0, z = 0$). The planar state $k_x - ik_y$ for the up-up spin Cooper pairs and $k_x + ik_y$ for the down-down spin Cooper pairs is attained in the middle region around “4” ($x = L/2, z = 0$), shown in Fig. 6.6(b). The planar state $k_y \pm ik_z$ is realized at the side edge “2” ($x = 0, z = D/2$) and the OP is recovered to the bulk value of the B-phase around “5” ($x = L/2, z = D/2$), shown in Fig. 6.6(c). At all edges ($x = 0$, $x = L$, $z = 0$, and $z = D$), the Majorana fermion edge state exists [65, 66, 68].

The spin current $j_{sy}^x(\mathbf{r})$, $j_{sy}^z(\mathbf{r})$, $j_{sx}^y(\mathbf{r})$, and $j_{sz}^y(\mathbf{r})$ are shown in Fig. 6.7(a). Since the spin current flows in the three-dimensional real space, we show the schematic flow of the spin current in Fig. 6.7(b). The spin current for the i -component of spin turns around the i -axis. This is understandable as follows: Since the up-up spin Cooper pairs have negative chirality and the down-down spin Cooper pairs have positive chirality, the z -component of the spin current turns around the z -axis. Other components are also understood in the same manner. Note that the schematic flow in Fig. 6.7(b) is derived from A_{ii} before rotation by

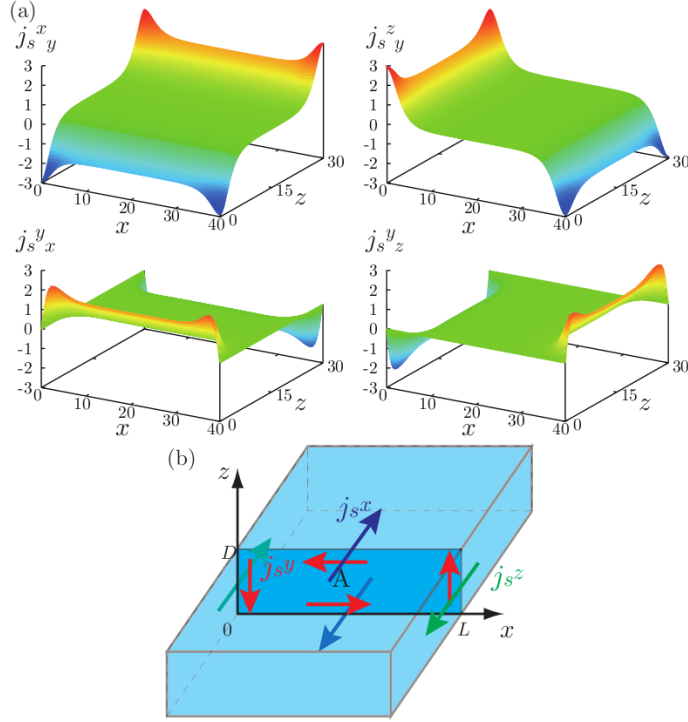


Figure 6.7: (a) The spin current for the B-phase with $D = 30$. The unit of the spin current is 10^{-9} J/m². (b) A schematic flow of the spin current for S_x , S_y , and S_z components.

$R(z, \theta_L)$. The rotation axes for the x - and y -component of the spin current are changed correspondingly.

Figure 6.8(a) shows the LDOS. It is seen that only the line “1” ($x = 0, z = 0$) has the zero energy LDOS from the zero energy Andreev bound state of QPs without the k_y -component. The lines “2” and “4” ($x = 0, z = D/2$ and $x = L/2, z = 0$) are almost the same and show the linear relation $N(E, \mathbf{r}) \propto E$ near $E = 0$ which reflects the surface Andreev bound states [108, 109]. The line “5” ($x = L/2, z = D/2$) corresponds to the bulk LDOS where the full gap is expected. In Fig. 6.8(b) we show the extension of the zero energy state toward the middle from the edge at $x = 0$. The zero energy LDOS of the line “I” ($z = 0$) reduces sharply as approaching the middle region from the edge. It is found that the value $N(E = 0, x = 0)$ in the line “IV” ($z = 0.5$) is much smaller than that of the line “I”. The line “II” along $z = D/2$ shows the absence of the zero energy LDOS. Therefore, we conclude that the zero energy LDOS is localized at the corner of the order of ξ_0 . The peak energy of the angle-resolved LDOS is shown in Figs. 6.8(c) for the side edge and 6.8(d) for the lower surface. Figure 6.8(c) is as a function of k_y for $k_z = 0$ and as a function of k_z for $k_y = 0$ at “2” ($x = 0, z = D/2$). Figure 6.8(d) is as a function of k_x for $k_y = 0$ and as a function of k_y for $k_x = 0$ at “4” ($x = L/2, z = 0$). These show that the side edge and lower surface have the same dispersion relation for low energy. The linear dispersion forms the Majorana cone at the surface [65].

The peak energy of the angle-resolved LDOS at the corner $(0, 0)$ is shown in Figs. 6.8(e) and 6.8(f). The energy is dispersionless along the k_z - and k_x -axes for $k_y = 0$. The Dirac valley-type dispersion is composed of the zero energy LDOS at the corner (the line “1” in

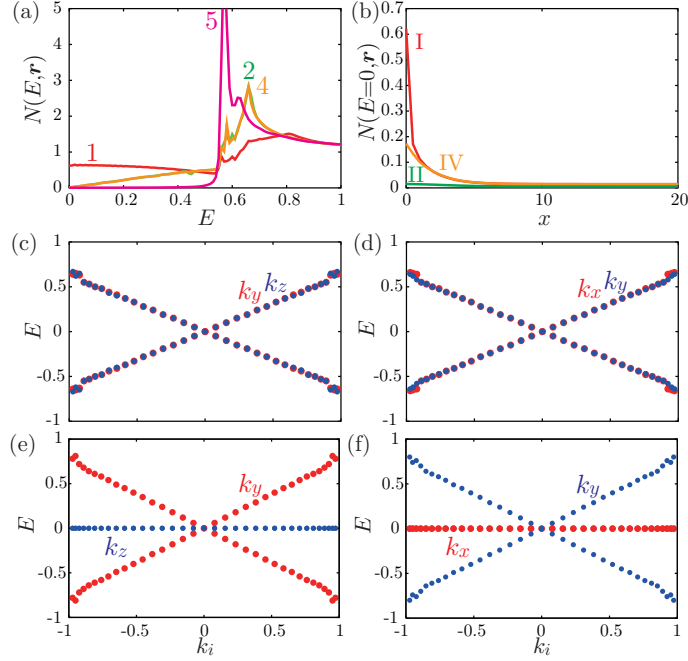


Figure 6.8: The LDOS for the B-phase with $D = 30$. (a) LDOS $N(E, \mathbf{r})$ at “1”, “2”, “4”, and “5”. (b) Zero energy LDOS $N(E = 0, \mathbf{r})$ along “I”, “II”, and “IV” ($z = 0.5$). The peak energy of angle-resolved LDOS as a function of k_y for $k_z = 0$ and as a function of k_z for $k_y = 0$ at “2” (c), and as a function of k_x for $k_y = 0$ and as a function of k_y for $k_x = 0$ at “4” (d). (e) and (f) are the same plots as (c) and (d), but at “1”.

Fig. 6.8(a)). This is different from the Majorana cone at the surface.

6.4.2 $D = 14\xi_0$: Thin slab for B-phase

We consider $D = 14$ in thickness of a slab which is the critical thickness for stabilizing the B-phase below which the stripe phase becomes stable [106]. Since the thickness is short, the k_z -component of the OP can not completely recover the bulk value. Except that the k_z -component is reduced, the qualitative features of the OP and the spin current are the same in the case of $D = 30$; however, the LDOS shows different spectrum.

Figure 6.9 shows the LDOS and the peak energy of the angle-resolved LDOS, which are compared with those in Fig. 6.8. The differences between them are following: Since the thickness of the slab is short, the line “5” for the center ($x = L/2, z = D/2$) has the spectrum from the full gap and the linear relation near $E = 0$, shown in Fig. 6.9(a). The latter comes from the contributions extending from the upper and lower surfaces. The line “2” for the side edge ($x = 0, z = D/2$) in Fig. 6.9(a) has the small peak at $E \approx 0.35$ composed of the deformed Majorana cone in $0.5 \lesssim |k_z| \lesssim 0.7$, shown in Fig. 6.9(c), because the QPs with the k_z -component reflect that the k_z -component of the OP does not recover the bulk value. The peak energy at “4” for the lower surface in Fig. 6.9(d) implies that the lowest energy of the Majorana cone is lifted from zero because of the tunneling of the zero energy modes bound at two surfaces corresponding to the upper and lower surfaces. For the same reason, the zero energy modes at the corner is split for $k_z = \pm 1$ in Fig. 6.9(e) and for $k_y = 0$ or $k_x = 0$ in

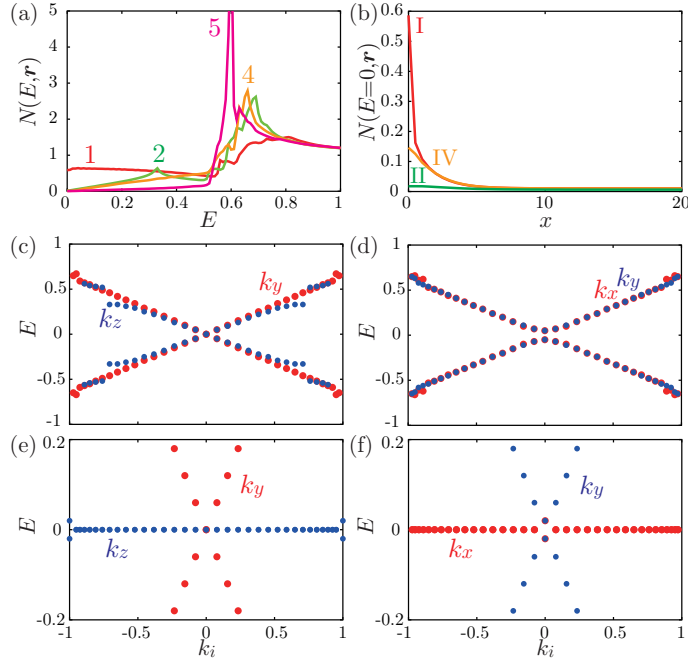


Figure 6.9: The same as in Fig. 6.8, but for the B-phase with $D = 14$.

Fig. 6.9(f). By the energy splitting, the zero energy LDOS is slightly reduced; however, the extension of the zero energy state is the same for the thick slab $D = 30$, shown in Fig. 6.9(b).

6.4.3 Dependence of the energy splitting on the thickness

The lowest energy of the Majorana cone at the lower surface is more lifted from the zero energy as the thickness is shorter. If the thickness is macroscopically long, the zero energy modes appear, shown in the left panel of Fig. 6.10(a) for the B-phase at “4” ($x = L/2, z = 0$) with $D = 30$. When the thickness is short, the zero energy modes bound at two surfaces are hybridized with each other. They form the symmetric and anti-symmetric states with the opposite sign energy E_+ and E_- , respectively, where $|E_+| = |E_-| = E_{\text{split}}$. The representative dispersion relation with $D = 12$ is shown in the middle panel in Fig. 6.10(a). In the case of more shorter thickness, the B-phase becomes the planar phase, which is metastable against the A-phase, because the k_z -component of the OP vanishes. Since the Fermi surface has the point nodes toward the direction of $k_x = k_y = 0$, the angle-resolved LDOS toward the direction corresponds to that of the normal state without the peak energy. We show the dispersion relation with $D = 8$ except the point $k_x = k_y = 0$ in the right panel in Fig. 6.10(a). There is a difference between the dispersion relations for $D = 12$ and $D = 8$ also in long wavelength which are curved and linear, respectively.

The dependence of the energy splitting on the thickness is shown in Fig. 6.10(b). The energy splitting has the relation $E_{\text{split}} \propto \exp(-D/3\xi_0)$, where $3\xi_0$ is effective coherence length. The exponential suppression is similar to the energy splitting of the Majorana zero energy modes bound at two vortices in a chiral p -wave superfluid [110, 111].

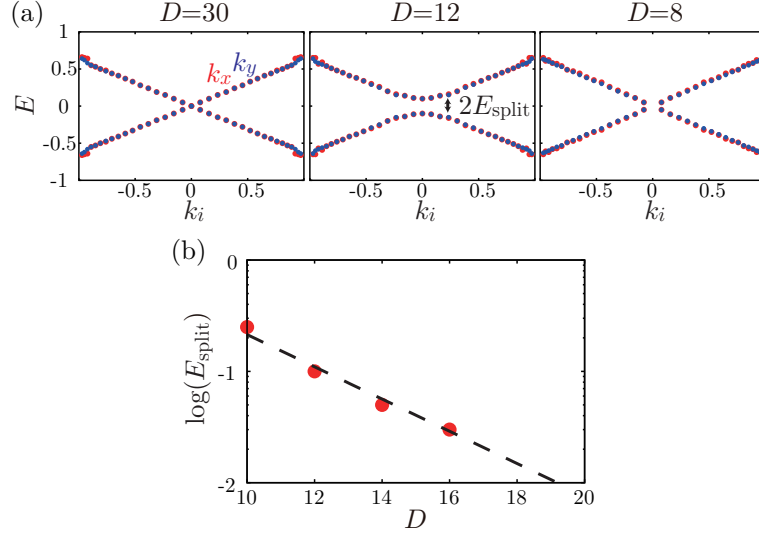


Figure 6.10: Calculated results for the B-phase at “4”. (a) The peak energy of angle-resolved LDOS as a function of k_x for $k_y = 0$ and as a function of k_y for $k_x = 0$ with several thicknesses $D = 30, 12,$ and 8 . (b) The dependence of the energy splitting on the thickness. The dashed line is proportional to $\exp(-D/3\xi_0)$.

6.5 Discussion

6.5.1 Majorana zero modes in the A- and B-phases

In the A-phase which has point nodes, since the zero energy QPs appear on the line $k_y = 0$ in the momentum space, the zero energy QPs are dispersionless along the k_z -direction (Fig. 6.3(g)). Therefore, the dispersion of the QPs forms the Dirac valley and the zero energy LDOS spreads over the order of $5\xi_0$ from the side edge (Figs. 6.3(c) and 6.3(d)). In contrast, since the OP in the B-phase has full gap on the Fermi surface, only the QPs with the momentum perpendicular to the edge are the zero energy Majorana QPs. Therefore, the dispersion of the QPs forms the Majorana cone (Figs. 6.8(c) and 6.8(d)). However, at the corner, the dispersion of the QPs forms the Dirac valley and the zero energy LDOS spreads over the order of ξ_0 . Types of dispersion relation for the A- and B-phases are summarized in Table 6.1.

The spin degeneracy of the QPs is also different between the A- and B-phases. In the A-phase, since the up-up and down-down spin Cooper pairs have the same chirality, the low energy QPs have the degenerate branch of the dispersion at the edge (Fig. 6.3(h)). In the B-phase, since the up-up and down-down spin Cooper pairs have the opposite chirality, the low energy QPs have two branches of the dispersion at the edge (Fig. 6.8(c)). This difference manifests itself in the edge current, namely, the mass current in the A-phase (Fig. 6.3(b)) and the spin current in the B-phase (Fig. 6.7).

6.5.2 Stripe phase

We discuss the Majorana zero modes at a domain wall in the stripe phase [106]. We take the thickness of a film along the z -direction and the modulation of the OP along the x -

Table 6.1: Types of dispersion relation at the upper or lower surface, side edge, and corner of a slab for the A- and B-phases. Dirac valley is formed from linear dispersion from $E = 0$ along a certain momentum direction and dispersionless zero energy modes along another momentum direction in long wavelength. Majorana cone is formed from isotropic linear dispersion from $E = 0$ on the plane parallel to a surface in the momentum space in long wavelength, where the zero mode is in a point on the Fermi surface. The mark \times indicates absence of zero energy modes.

		upper or lower surface	side edge	corner
A-phase	thin slab ($D = 8\xi_0$)	\times	Dirac valley	Dirac valley
	thick slab ($D = 14\xi_0$)	\times	Dirac valley	Dirac valley
B-phase	thin slab ($D = 14\xi_0$)	\times	Majorana cone	Dirac valley
	thick slab ($D = 30\xi_0$)	Majorana cone	Majorana cone	Dirac valley

direction. In the stripe phase, the k_z -component of the OP changes the sign at the domain wall perpendicular to the x -direction so that the pair breaking by the reflection at the surface of the film is prevented. Then, the OP is described as $\mathbf{\Delta}_{\text{right}} = (\Delta_{\parallel}k_x, \Delta_{\parallel}k_y, \Delta_{\perp}k_z)$ to the right of the domain wall and $\mathbf{\Delta}_{\text{left}} = (\Delta_{\parallel}k_x, \Delta_{\parallel}k_y, -\Delta_{\perp}k_z)$ to the left of the domain wall, where Δ_{\parallel} is finite everywhere and Δ_{\perp} vanishes at the domain wall.

The QPs with the k_z -component which across the domain wall have the finite energy Andreev bound states because they feel the sign change of the k_z -component of the pair potential, which is not the exact π -phase shift. In addition, since the QPs with $k_z = 0$ feel the full gap of the pair potential, they are not excited in low energy. Therefore, the Majorana zero energy QP is absent at the domain wall in the stripe phase. The domain wall is qualitatively different from the edge.

6.5.3 Experimental proposal

There are several experimental means to detect the Majorana nature. Surface specific heat measurement, which was performed in connection with detection of the Andreev surface bound state [112], resolves the side edge contribution $C_{\text{surface}}(T) = \gamma T$ of the A-phase in a thin slab at low temperatures, where $\gamma \propto N(E = 0)$, because the bulk contribution $C_{\text{bulk}} \propto T^3$ which comes from point nodes where $N(E) \propto E^2$ is distinguishable. Note that, in the A-phase, the contribution from the two upper and lower specular surfaces in the slab geometry is the same as that from the bulk. Thus, the surface specific heat $C_{\text{surface}}(T) = \gamma T$ of the Majorana QPs is distinctive. If the l -vector direction is modulated near the side edge, the LDOS at the surface is $N(E) = N(0) + N_{\text{gap}}(E)$. The surface specific heat from the LDOS is also $C_{\text{surface}}(T) = \gamma T$.

In the B-phase, the zero energy LDOS is localized at the corner of the order of ξ_0 . The contribution from the corner is interesting but smaller than that of the surface. Since we will discriminate $C_{\text{bulk}} \propto T^{-3/2}e^{-\Delta/k_B T}$ from the gap Δ and $C_{\text{surface}} \propto T^2$ from the linear behavior of LDOS $N(E, \mathbf{r}) \propto E$ near $E = 0$, the Majorana fermion can be observed. In the slab with short thickness where the zero energy modes are split at the upper and lower surfaces, the difference of the specific heat from the surface and bulk will not be distinctive because the gap structure and linear behavior of the LDOS coexist.

The observation of the edge mass current in the A-phase, which is intimately connected

with the intrinsic angular momentum [2], is also hopeful. The magnitude of the edge mass current is unchanged in wider slabs than $L = 40\xi_0$ for which we have calculated. Considering the observation of the torque from the edge mass current for a $10 \text{ mm} \times 7 \text{ mm} \times 0.6 \mu\text{m}$ slab sample (Bennett *et al.* [100] had been used) by a typical torsional oscillator, the frequency shift from the edge mass current is of the order of 10^{-23} Hz [113]. The torque is too small to observe by a torsional oscillator because the magnitude is $\sim N\hbar/2$, where N is the total number of ^3He atoms in the slab sample. We have to consider other experimental methods. Analytical derivation of the torque is shown in Appendix B. Also the edge spin current in the B-phase which flows three-dimensionally has been obtained quantitatively. The techniques to detect the spin current is desired. The specific experimental proposal to observe the edge current is a future problem.

The most direct evidence of the Majorana nature is derived from the observation of the anisotropic spin susceptibility. If we use the Majorana nature of the edge state, in the A-phase, the local spin operators result in $S_x \approx S_y \approx 0$ and only S_z parallel to d -vector remains nontrivial for $T \ll T_c$ [64]. This predicts the Ising-like spin dynamics for the local spin operator parallel to d -vector in the A-phase as well as that perpendicular to the edge in the B-phase [65, 68]. This is in sharp contrast to the susceptibility parallel to d -vector in the bulk A-phase which is suppressed at low temperatures according to the Yosida function. On the other hand, the susceptibility perpendicular to d -vector still assumes the bulk value, which is the same as it in the normal state. The anisotropic susceptibility has been discussed also by Shindou *et al.* [114] and has been calculated in the B-phase by Nagato *et al.* [68].

QP scattering or QP beam experiments are extremely interesting. They were performed in the past on ^4He where roton-roton scattering is treated [115] and on the ^3He B-phase where the surface Andreev bound state is investigated [116, 117]. Using this method, we may pick up Majorana QPs with a particular wave number. Particularly in the A-phase, the Majorana QPs from the edge is separated from other QPs from the nodal region.

Another option might be to use a free surface where the Majorana fermion surface state is formed. As shown by Kono [118], it can be detected through the excitation modes of the floating Wigner lattice of electrons placed on the surface. We need a special, but feasible configuration of the experimental setups.

Note that the recent work of transverse acoustic impedance measurements to detect the surface bound states in the superfluid ^3He will derive the important information of the Majorana QPs [119, 120, 121].

6.6 Summary

We have designed a concrete experimental setup to observe the Majorana nature at the surface in the slab geometry. In connection with realistic slab samples, we have considered the upper and lower surfaces and the side edges including the corners with several thicknesses. We have demonstrated that the quasi-classical Eilenberger equation yields the quantitatively reliable information on physical quantities for the superfluid ^3He A- and B-phases. Specifically, we have exhibited the difference of LDOS between the A- and B-phases and evaluated the mass current for the A-phase and the spin current for the B-phase quantitatively. Then, we have shown the influence on the Majorana zero modes from the spatial variation of l -vector for the A-phase in the thick slab and the energy splitting of the zero energy modes for the B-phase confined in the thin slabs. The corner of the slab in the B-phase is accompanied by the unique zero energy LDOS of corner modes. In addition, we have demonstrated the absence

of the Majorana zero energy QP at the domain wall in the stripe phase. On the basis of the quantitative consequences, it is proposed that the measurement of the specific heat, the edge current, and the anisotropic spin susceptibility provides feasible and verifiable experiments to check the Majorana nature. The control on the thickness of the slab is crucial to detect the Majorana surface states. The experiment controlling the thickness of the film of the superfluid ^3He is interesting [101].

Chapter 7

p-wave resonant superfluids of Fermi atomic gases

Recently, *p*-wave resonant superfluidity attracts much attention in Fermionic alkaline atomic gases, such as ${}^6\text{Li}$ [13, 14, 15] and ${}^{40}\text{K}$ [16, 17, 18], both experimentally and theoretically [50, 122, 123, 124, 125]. Experiments into achieving *p*-wave resonant superfluidity are steadily progressing and hence it is timely and necessary to consider the generic properties of *p*-wave superfluidity both at rest and under rotation to detect its superfluidity, which is signified by non-trivial topological structures or vortices. In this chapter, textures and vortices for *p*-wave resonant superfluids of Fermi atomic gases are calculated by the Ginzburg-Landau (GL) theory.

The textures are different from the superfluid ${}^3\text{He}$ by the boundary condition, because Fermi atomic gases are confined in harmonic trap potential. The trap potential is easily controlled, resulting in various shapes, such as cigar or pancake shapes. As we describe below, the trapping potential can be an important tool to control the three-dimensional (3D) texture. Indeed, the 3D trapping structure constrains the possible textures. Our purpose is to investigate a possible 3D textures in a 3D harmonic trap potential and thereby to help identifying *p*-wave superfluidity.

Moreover, we investigate vortices with Majorana quasi-particle (QP) in “spinless” *p*-wave resonant superfluids of Fermi atomic gases with high controllability [126, 63]. Therefore, they will be a favorable platform of quantum computation.

The organization of this chapter is as follows: We employ the GL framework under rotation and trap potential which relies only on global symmetry principle. The GL free energy functional form is introduced and the relevant physical quantities, such as supercurrent and *l*-vector are given in Sec. 7.1. We show the phase diagram of the stable states for uniform and infinite system, and explain how to numerically examine realistic confined systems in Sec. 7.2. Section 7.3 presents the stable texture in the cigar shape trap, especially, we mention the spontaneous supercurrent at rest and the half-quantum vortex (HQV) under rotation. In Sec. 7.4, we show the different textures stabilized in the pancake shape. In Sec. 7.5, we consider the quasi-two-dimensional (quasi-2D) shape trap. In this trap, a singular vortex with Majorana QP is realized. The final section is devoted to a summary.

7.1 Formulation

Here we employ the GL framework [2]. This framework is general and flexible enough to allow us to examine a generic topological structure, and applicable to cold fermionic atom gases with a harmonic trap potential under $k_B T_c \gg \hbar\omega$, where T_c and ω are the transition temperature and the trap frequency, respectively [127]. In terms of the tensor $A_{\mu i}$ forming order parameter (OP) of *p*-wave pairing the most general GL functional density f_{bulk} for the bulk condensation energy up to quartic order is described as

$$f_{\text{bulk}} = -\alpha_i A_{\mu i}^* A_{\mu i} + \beta_1 A_{\mu i}^* A_{\mu i}^* A_{\nu j} A_{\nu j} + \beta_2 A_{\mu i}^* A_{\mu i} A_{\nu j}^* A_{\nu j} + \beta_3 A_{\mu i}^* A_{\nu i}^* A_{\mu j} A_{\nu j} \\ + \beta_4 A_{\mu i}^* A_{\nu i} A_{\nu j}^* A_{\mu j} + \beta_5 A_{\mu i}^* A_{\nu i} A_{\nu j} A_{\mu j}^*, \quad (7.1)$$

which is invariant under spin and real space rotations in addition to the gauge invariance $U(1) \times SO^{(S)}(3) \times SO^{(L)}(3)$. The quartic order terms are characterized by five independent invariants, β_1 – β_5 in general [2]. Since the spin degrees of freedom are frozen due to applied magnetic field for magnetic Feshbach resonance, only the orbital degrees of freedom A_i in $A_{\mu i} = (\hat{\mathbf{m}} + i\hat{\mathbf{n}})_{\mu} A_i$ are active, where $\hat{\mathbf{m}}$ and $\hat{\mathbf{n}}$ are orthogonal. Namely it reduces to

$$f_{\text{bulk}} = -\alpha_0(1 - t_i) A_i^* A_i + \beta_{24} A_i^* A_i A_j^* A_j + \beta_3 A_i^* A_i^* A_j A_j, \quad (7.2)$$

where $\beta_{24} = \beta_2 + \beta_4$ and $t_i = T/T_{ci}$ (T_{ci} is the transition temperature for the *i*-component). As mentioned in Chap. 3, the dipole-dipole interaction causes splitting of the transition temperatures into two groups $T_{cx} = T_{cy}$ and T_{cz} . We introduce $\alpha = T_{cx}/T_{cz}$, which indicates the degree of the broken symmetry of the system and characterizes atomic species used [17]. The pairing state having the orbital projection $m_l = 0$ is favorable over $m_l = \pm 1$, namely $0 < \alpha < 1$ due to the dipole-dipole interaction [17]. The three components become degenerate for $\alpha \rightarrow 1$. When $\alpha \rightarrow 0$, the polar state with the OP $\Delta(\mathbf{k}) = A_z k_z$ tends to be stable.

The gradient energy consisting of the three independent terms [2] is given by

$$f_{\text{grad}} = K_1 (\partial_i^* A_j^*) (\partial_i A_j) + K_2 (\partial_i^* A_j^*) (\partial_j A_i) + K_3 (\partial_i^* A_i^*) (\partial_j A_j). \quad (7.3)$$

The centrifugal potential energy due to rotation with $\boldsymbol{\Omega}$, which is derived in Appendix C, is written as

$$f_{\text{cent}} = -\frac{m^2}{\hbar^2} \Omega^2 \rho^2 (K_1 A_i^* A_i + K_2 |A_{\theta}|^2 + K_3 |A_{\theta}|^2), \quad (7.4)$$

where $\partial_i = \nabla_i - i(m/\hbar)(\boldsymbol{\Omega} \times \mathbf{r})_i$. For $\boldsymbol{\Omega} \parallel \hat{\mathbf{z}}$, $\rho^2 = x^2 + y^2$ and $A_{\theta} = -A_x \sin \theta + A_y \cos \theta$ in the cylindrical coordinates.

The GL parameters α_0 , $\beta_{24} = \beta_2 + \beta_4$, β_3 and $K_1 = K_2 = K_3 = K$ are estimated by taking the weak-coupling approximation [2]:

$$\alpha_0 = \frac{N(0)}{3}, \quad \beta_2 = \beta_3 = \beta_4 = \frac{7\zeta(3)N(0)}{120(\pi k_B T_c)^2} \equiv \beta \quad (7.5)$$

and

$$K = \frac{7\zeta(3)N(0)(\hbar v_F)^2}{240(\pi k_B T_c)^2} \quad (7.6)$$

where $N(0)$ is the density of states at the Fermi level and v_F is the Fermi velocity. The weak-coupling approximation should be a good guide for understanding the generic properties of the *p*-wave superfluids of atom gases because it has been applied successfully, even to liquid ^3He with strong interacting fermions and only small additional strong corrections [2].

The GL free energy density functionals, eqs. (7.2)–(7.4), can be expressed with dimensionless units. The units of OP, length, and rotation frequency are the OP amplitude of the chiral state in a bulk $\Delta_0 = \sqrt{10\pi^2/7\zeta(3)}k_B T_c$, the GL coherence length $\xi_0 = \sqrt{7\zeta(3)/48\pi^2}(\hbar v_F/k_B T_c)$ with zero temperature, and $\Omega_0 = \hbar/m\xi_0^2$, respectively, where v_F is the Fermi velocity. In the dimensionless unit, eqs. (7.2)–(7.4) are written as

$$f_{\text{bulk}} = -(1 - t_i)A_i^* A_i + \frac{1}{2}A_i^* A_i A_j^* A_j + \frac{1}{4}A_i^* A_i^* A_j A_j, \quad (7.7)$$

$$f_{\text{grad}} = \frac{3}{5} [(\partial_i^* A_j^*)(\partial_i A_j) + (\partial_i^* A_j^*)(\partial_j A_i) + (\partial_i^* A_i^*)(\partial_j A_j)], \quad (7.8)$$

$$f_{\text{cent}} = -\frac{3}{5}\Omega^2 \rho^2 (A_i^* A_i + 2|A_\theta|^2), \quad (7.9)$$

respectively, where $\partial_i = \nabla_i - i(\boldsymbol{\Omega} \times \mathbf{r})_i$. From now on we use the dimensionless expressions.

The effect of harmonic trap potential on condensates depends on the dimensionless pairing interaction Γ that determines the transition temperature $T_c = CE_F \exp(-1/\Gamma)$, where E_F is the Fermi energy and C is a numerical coefficient of order unity [127]. We use the unit $\hbar\omega_0 = \sqrt{144\pi^2/35\zeta(3)}\sqrt{2\Gamma/(1+2\Gamma)}k_B T_c$ for the trap frequency ω . The p -wave triplet paring interaction is $\Gamma \approx \lambda^2/13$ with a gaseous parameter $\lambda = 2|a|p_F/\pi\hbar$, where a is the scattering length and p_F is the Fermi momentum [128]. The harmonic trap potential term [127] is

$$f_{\text{harm}} = \frac{3}{5}\omega_\perp^2 (\rho^2 + \lambda^2 z^2) A_i^* A_i, \quad (7.10)$$

where the dimensionless radial confining potential is ω_\perp and the anisotropy of the harmonic trap is expressed as $\lambda \equiv \omega_z/\omega_\perp$. The harmonic trap potential term acts to lower the transition temperatures.

Rotation frequency is also normalized by the critical rotation frequency Ω_c , where condensates fly away from the trap potential by centrifugal force. We sum up the centrifugal energy and the trap potential energy as

$$f_{\text{cent}} + f_{\text{harm}} = \frac{3}{5}(\omega_\perp^2 - \Omega^2)\rho^2(|A_r|^2 + |A_z|^2) + \frac{3}{5}(\omega_\perp^2 - 3\Omega^2)\rho^2|A_\theta|^2 + \frac{3}{5}\lambda^2\omega_\perp^2 z^2 A_i^* A_i$$

with cylindrical coordinates. Therefore, the critical rotation frequency is given by $\Omega_c = \omega_\perp/\sqrt{3}$.

The relevant physical quantities are described in terms of the OP $A_i(\mathbf{r})$ as follows. The total free energy:

$$F = \int d^3r (f_{\text{bulk}} + f_{\text{grad}} + f_{\text{cent}} + f_{\text{harm}}). \quad (7.11)$$

The current density:

$$j_i(\mathbf{r}) \equiv 2\text{Im} [A_j^* \nabla_i A_j + A_j^* \nabla_j A_i + A_i^* \nabla_j A_j]. \quad (7.12)$$

l -vector:

$$l_i(\mathbf{r}) \equiv -i\epsilon_{ijk} \frac{A_j^* A_k}{|\Delta(\mathbf{r})|^2} \quad (7.13)$$

with

$$|\Delta(\mathbf{r})|^2 = A_i^* A_i. \quad (7.14)$$

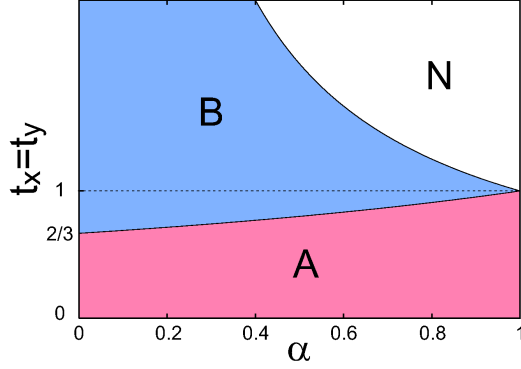


Figure 7.1: Phase diagram of the *p*-wave pairing state in an infinite system at rest, showing temperature ($t_x = t_y$) versus anisotropy $\alpha \equiv T_{cx}/T_{cz}$. N: normal state, A: chiral state $A_z(k_z + i\gamma k_\perp)$ and B: polar state $A_z k_z$.

7.2 Preliminary considerations

Before considering a realistic confined system, we first investigate an infinite system at rest. Then the state minimizing the condensation energy (7.7) is realized. As shown in Appendix D, the phase diagram in Fig. 7.1 consists of the three phases, A, B, and normal (N) phases. The B phase is described by $\Delta(\mathbf{k}) = A_z k_z$, i.e. the polar state. The A phase is described by a chiral OP expressed by

$$\Delta(\mathbf{k}) = A_z(k_z + i\gamma k_\perp), \quad (7.15)$$

where ($0 < \gamma \leq 1$) with $k_\perp = k_x \cos \phi + k_y \sin \phi$ (ϕ is arbitrary). This phase breaks the time reversal symmetry. The value of γ depends on temperature and anisotropy α ,

$$\gamma = \frac{2 - (3 - \alpha)t_x}{2 + (1 - 3\alpha)t_x}. \quad (7.16)$$

In the absence of the dipole-dipole interaction ($\alpha = 1$), the value of γ is unity. As the dipole-dipole interaction increases (α decreases), γ decreases. The decrease of γ becomes larger at high temperature. When the value of γ vanishes, the second order transition from the A phase to the B phase takes place. The transition temperature t_c is given by

$$t_c = \frac{2}{3 - \alpha}. \quad (7.17)$$

The phase diagram corresponds to the case being not so large Feshbach resonance splitting in BCS regime [122]. However, it is warned that the determined phase boundary is of qualitative at low temperatures which is beyond the GL framework. In the following we examine the A phase in confined geometries.

In order to obtain stable texture of the condensates in a realistic harmonic potential, we have identified stationary solutions by numerically solving the variational equations: $\delta f(\mathbf{r})/\delta A_i(\mathbf{r}) = 0$ in three dimensions where $f(\mathbf{r})$ is the GL energy density functional, the integrand of (7.11). We start with various initial configurations, including singular vortex state and non-singular vortex state, and determine the most stable texture by comparing the total GL energy (7.11).

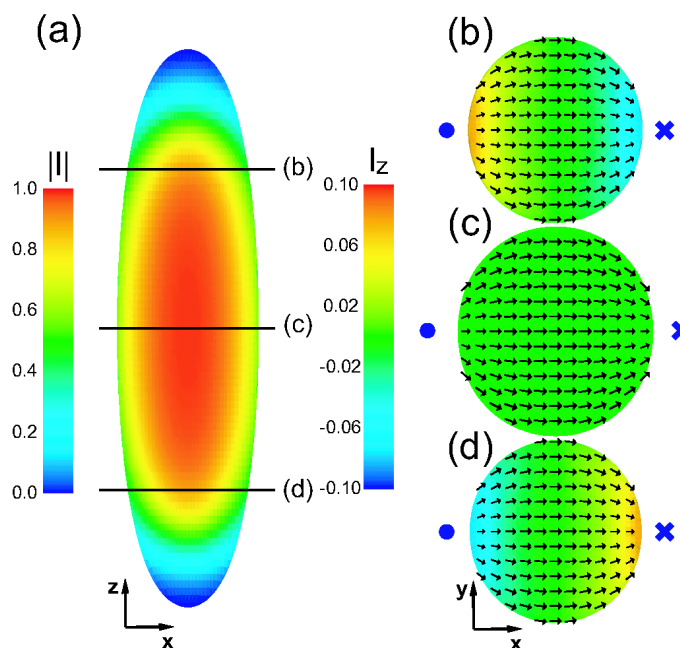


Figure 7.2: Stable texture at rest for cigar trap $\lambda = 0.2$. (a) Distribution of $|l|$ in the z - x plane. (b)-(d) Three cross sections indicated in (a), showing l_z (color) and l_x and l_y components (arrows), where the dot and cross marks indicate the imaginative source and sink for the l -vector stream lines.

7.3 Cigar shape trap

We first consider the stable texture for a cigar shape trap with the trap anisotropy $\lambda = 0.2$. We take $80 \times 80 \times 120$ meshes with the cloud sizes for the Thomas-Fermi (TF) approximation $R_x = R_y = 10\sqrt{5/3}$ and $R_z = 50\sqrt{5/3}$. We fix the temperature at $t_x = t_y = 0.4$ and the anisotropy parameter $\alpha = 0.9$.

7.3.1 Stable texture at rest

The stable l -vector texture at rest is shown in Fig. 7.2. Figure 7.2(a) displays the amplitude distribution of the l -vectors. It can be seen that the amplitude $|l|$ is maximum in the central region, and towards the outer regions $|l|$ decreases gradually. At the top and bottom ends, the polar state is realized where the l -vector vanishes. Three cross sections are shown in Figs. 7.2(b)-(d). In Fig. 7.2(c), which corresponds to the middle cross section, the l -vectors lie in the x - y plane, showing a streamline type pattern in which the l -vectors follow the circumference, like a fluid streaming along a circular boundary. Outside the condensates, an unseen sink and source of the l -vectors exist, giving two imaginative focal points situated outside. Namely the left dot and right cross marks in Figs. 7.2(b)-(d) correspond to the source and sink where the l -vectors appear and disappear. This streamline like texture contrasts with the so-called Pan-Am texture in superfluid ^3He A-phase [2] where l -vectors tend to point perpendicular to the wall due to the boundary condition. In the upper (Fig. 7.2(b)) and lower (Fig. 7.2(d)) cross sections the streamline texture is maintained, but an l_z component appears in addition.

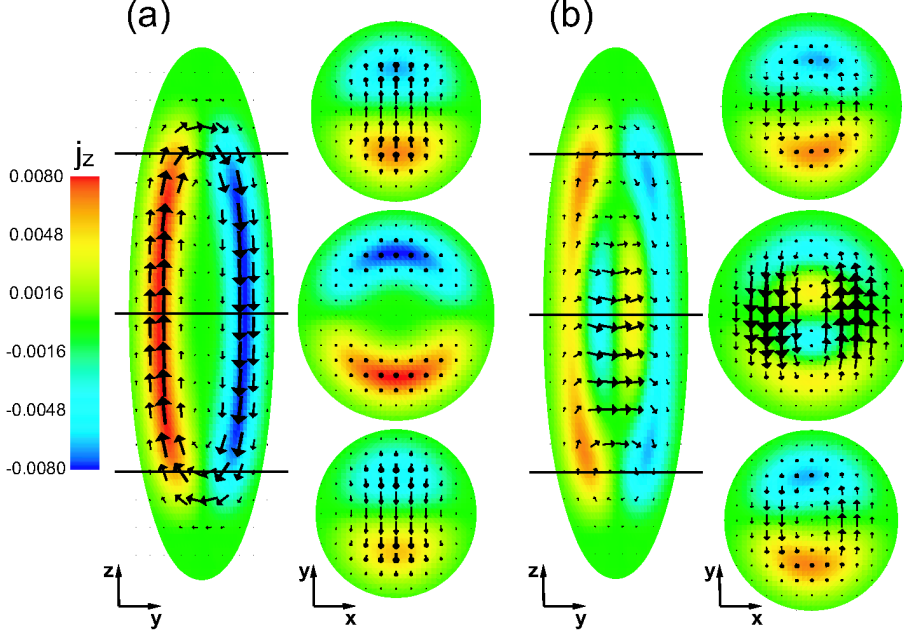


Figure 7.3: (a) Spontaneous circulating current flows at rest ($\Omega = 0$) in the z - y plane along the z direction. Three cross sections indicated in the left figure, showing j_z (color) and j_x and j_y components (arrows). (b) The current pattern under rotation ($\Omega = 0.3$). It is seen that the in-plane components j_x and j_y increase, producing the in-plane circular current due to rotation.

The associated supercurrent structure is depicted in Fig. 7.3. The j_z component shows a circulation supercurrent along the z -axis (see Fig. 7.3(a)). Since $\Omega = 0$, this circulation supercurrent is spontaneously generated. This non-trivial condensates flow can be explained in supercurrent characteristic of chiral p -wave superfluid:

$$\mathbf{j} = \rho_s \mathbf{v}_s + \mathbf{C}(\nabla \times \mathbf{l}), \quad (7.18)$$

where ρ_s and \mathbf{C} are diagonal tensor coefficients. The supercurrent has a structure that is similar to that for the total charge-current density of a system in classical electrodynamics. The current in classical electrodynamics is composed of two parts, the actual charge transport and an effective current in proportion to $\nabla \times \mathbf{M}$ due to the magnetization \mathbf{M} generated by the internal motion of the electrons. In chiral p -wave superfluid the Cooper pair may be thought of as representing the atom and \mathbf{l} the magnetic orbital moment \mathbf{M} . Therefore the first term in the supercurrent describes the usual flow of Cooper pairs, while the second one is an “orbital” supercurrent driven by the spatial variation of \mathbf{l} -vector.

In this system, the spontaneous supercurrent is not a usual supercurrent $\rho_s \mathbf{v}_s$ but an “orbital” supercurrent $\mathbf{C}(\nabla \times \mathbf{l})$ with the trap potential. In the middle cross section in Fig. 7.3(a), \mathbf{l} -vector in-plane bending $(\nabla \times \mathbf{l})_z$ produces a perpendicular current j_z . However, at the upper and lower planes in Fig. 7.3(a), the supercurrent acquires the j_x and j_y components because of the non-vanishing l_z component. Therefore, the perpendicular current at the center bends such that the condensates are conserved. It is clear from Fig. 7.3(a) that the supercurrent circulates perpetually along the z direction parallel to the long axis of the

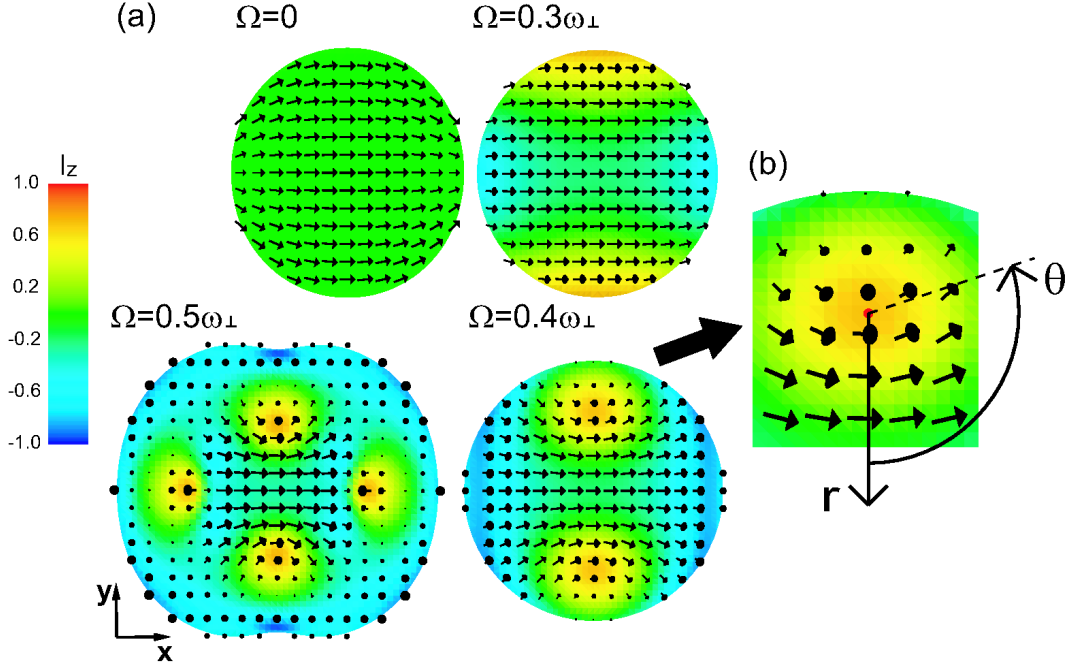


Figure 7.4: (a) Texture change with rotational speed Ω relative to the in-plane trap frequency ω_{\perp} . Middle cross sections are displayed showing l_z (color) and l_x and l_y components (arrows). As Ω increases, l -vectors acquire a negative z component (seen as a color change). At $\Omega = 0.4\omega_{\perp}$ two plus HQVs enter from the y direction seen as yellow objects. At $\Omega = 0.5\omega_{\perp}$ four plus HQVs and two minus HQVs are present and the condensates expand and deform. (b) The enlarged figure of HQV where the local coordinates (r, θ) are shown.

trap. This result is non-trivial and a remarkable manifestation in the topological nature of the texture.

In Fig. 7.3(b) we also display the current patterns under rotation ($\Omega = 0.3\omega_{\perp}$) for comparison at rest. It is seen that the in-plane components j_x and j_y increase, producing the in-plane circular current due to rotation, in particular in the middle cross section. Thus under rotations, the current consists of the spontaneous one along the z direction and the induced circular current in the plane.

7.3.2 Half-quantum vortex under rotation

In Fig. 7.4 where we depict the middle cross sections of the stable solutions for various rotation speeds (also see Fig. 7.6). It is seen that under rotation, the 3D texture deforms continuously and smoothly. As the rotational speed increases, l -vectors in the x - y plane pointing in the x direction acquire a negative z component, as seen by the color change from green to blue. This deformation yields in plane circular “orbital” supercurrent as already shown in Fig. 7.3(b).

Above a certain rotational speed ($\Omega = 0.4\omega_{\perp}$), two HQVs enter from the y direction, where the l -vector at the core pointing in the positive z direction, as seen by the yellow objects. The OP far away from the HQV core is described in terms of the local coordinated

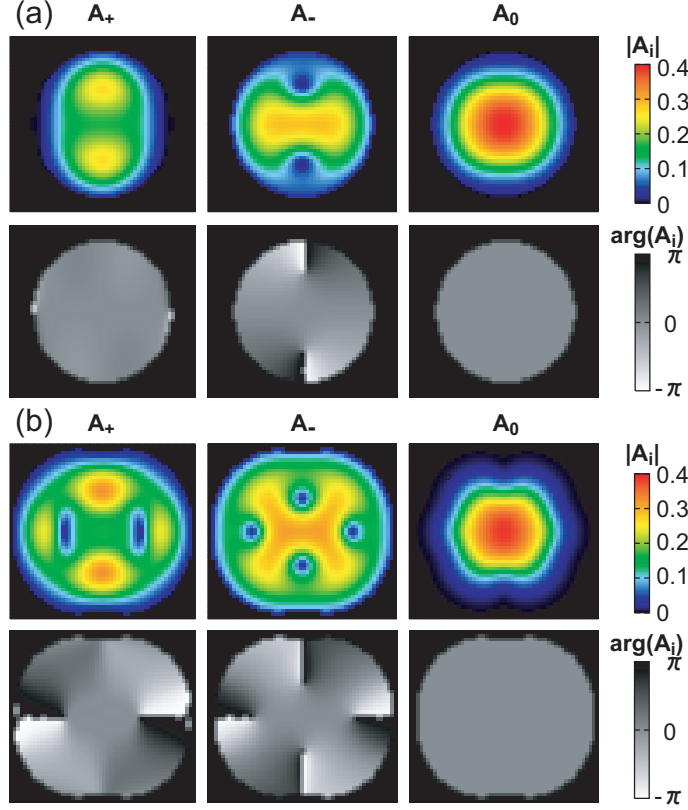


Figure 7.5: The amplitude (upper) and phase (lower) of the OP components A_+ , A_- and A_0 in the x - y plane at $z = 0$ corresponding to Fig. 7.4. (a) At $\Omega = 0.4\omega_\perp$ the vortices with winding number 1 enter A_- component. The depletion of the OP amplitude by the vortices is compensated by the growth of A_+ amplitude. (b) At $\Omega = 0.5\omega_\perp$ the vortices with winding number 1 appear. The vortices on the y - and x -axis are plus and plus-minus HQVs, respectively.

(r, θ) centered at the core (see Fig. 7.4(b)) as

$$\Delta(r \gg 1, \theta, \mathbf{k}) = \exp[i(\theta/2 + \pi/2)]|A_{xy}|[\sin(\theta/2)k_x - \cos(\theta/2)k_y] + |A_z|k_z, \quad (7.19)$$

where $|A_{xy}|$ and $|A_z|$ are amplitude of the polar state characterized by the basis functions k_x - k_y (x - y polar state) and by k_z (z polar state), respectively. The HQV is formed by only the x - y polar state as is seen from (7.19). The above state (7.19) can be rewritten as

$$\Delta(r \gg 1, \theta, \mathbf{k}) = \frac{1}{\sqrt{2}}|A_{xy}|(k_+ + e^{i\theta}k_-) + |A_z|k_0, \quad (7.20)$$

where $k_\pm = \mp(k_x \pm ik_y)/\sqrt{2}$ and $k_0 = k_z$. The vortex core of this HQV has the orbital angular momentum with positive z component because k_+ is non-vanishing there, so we define it as a plus HQV. Similarly, one can construct a minus HQV with the identical vorticity but the local orbital angular momentum of the negative z component in its core (k_-).

The realized OP rewritten as

$$\Delta(\mathbf{r}, \mathbf{k}) = A_+(\mathbf{r})k_+ + A_-(\mathbf{r})k_- + A_0(\mathbf{r})k_0, \quad (7.21)$$

where $A_{\pm} = \mp(A_x \mp iA_y)/\sqrt{2}$ and $A_0 = A_z$. In Fig. 7.5(a), the amplitudes (upper line) and phases (lower line) for each component A_+ , A_- , A_0 are displayed for $\Omega = 0.4\omega_{\perp}$ corresponding to Fig. 7.4. It is seen that there are two vortices with the winding number 1 in A_- component on the y axis. The depletion of the OP amplitude by the vortices is compensated by the growth of A_+ amplitude. The HQV is embedded in the surrounding OP field. As we walk around one of the HQV core, the p -wave pairing state changes in the following manner: At $\theta = \pi$, the OP is described as $\Delta(\mathbf{k}) = -|A_{xy}|k_x + |A_z|k_z$, namely this is the polar state. At $\theta = 0$, the OP is now $\Delta(\mathbf{k}) = -i|A_{xy}|k_y + |A_z|k_z$. This is a superposition of the polar state and the chiral state. The spatial position where the arrow of l -vector near the HQV core vanishes is the polar state, and on the opposite side of HQV core, the chiral state is superposed by the polar state. Since this HQV breaks the reflection symmetry, the isolated HQV is energetically disfavored and rather a pair of the HQV is advantageous. This is one of the reasons why we found a pair of the HQV at $\Omega = 0.4\omega_{\perp}$.

Upon further increase in the rotational speed ($\Omega = 0.5\omega_{\perp}$), the HQVs enter further from the x direction (see Fig. 7.4). They are different from above mentioned plus HQVs. As is seen from Fig. 7.5(b), a pair of plus-minus HQVs appears from the x direction. There are the vortices with the winding number 1 in each A_+ and A_- component on the different position of the x -axis. The depletion of the OP amplitude by the vortices is compensated by the growth of amplitude with the opposite orbital angular momentum component. The minus HQV is situated more inside in the trap potential than plus HQV, because of the repulsive interaction between the plus HQV on the x -axis and the y -axis. It is an analogous situation for the HQVs in the $F = 1$ spinor BEC [129]. We also notice from Fig. 7.4 ($\Omega = 0.5\omega_{\perp}$) that the condensate profile itself expands, deforms and deviates clearly from a circular form due to the non-trivial centrifugal energy.

Figure 7.6 shows a different view of Fig. 7.4, displaying the z - x cross section. At rest, l -vectors point almost to the x direction. As Ω increases, the downward l_z component appears, which causes a counterclockwise circular ‘‘orbital’’ supercurrent. At the top and bottom ends of the system the HQVs appear as indicated by asterisks. These blue lines show the polar state neighboring the HQV as mentioned above. In the $\Omega = 0.5\omega_{\perp}$ case, the side view of two pairs of plus-minus HQVs can be seen clearly. The light blue lines indicated by the red arrows correspond to the polar states between plus and minus HQV. These lines bend outward away from the center towards $\pm z$ direction. Around the positions indicated by the red arrows the condensate profile is greatly deformed. Because there the polar state dominates over the chiral state, which leads to the depletion of the condensate, resulting in this deformation.

7.4 Pancake shape trap

In order to understand the geometric effect of the textures stabilized in cigar shape trap, we examine the pancake trap case. We consider the anisotropy $\lambda = 3.0$ as an example, where we take $100 \times 100 \times 80$ meshes with the cloud size $R_x = R_y = 30\sqrt{5/3}$ and $R_z = 10\sqrt{5/3}$ in the TF approximation. We fix the temperature at $t_x = t_y = 0.5$ and $\alpha = 0.95$.

7.4.1 Axis symmetric texture at rest

Figure 7.7 displays the resulting l -vector texture (Fig. 7.7(a)) and associated in-plane supercurrent (Fig. 7.7(b)) at rest. It is seen that most of the l -vectors point to the negative z direction, except for those near the upper and lower surface regions, which acquire the r -component of the radial direction. The trap potential forces the l -vector to be parallel to

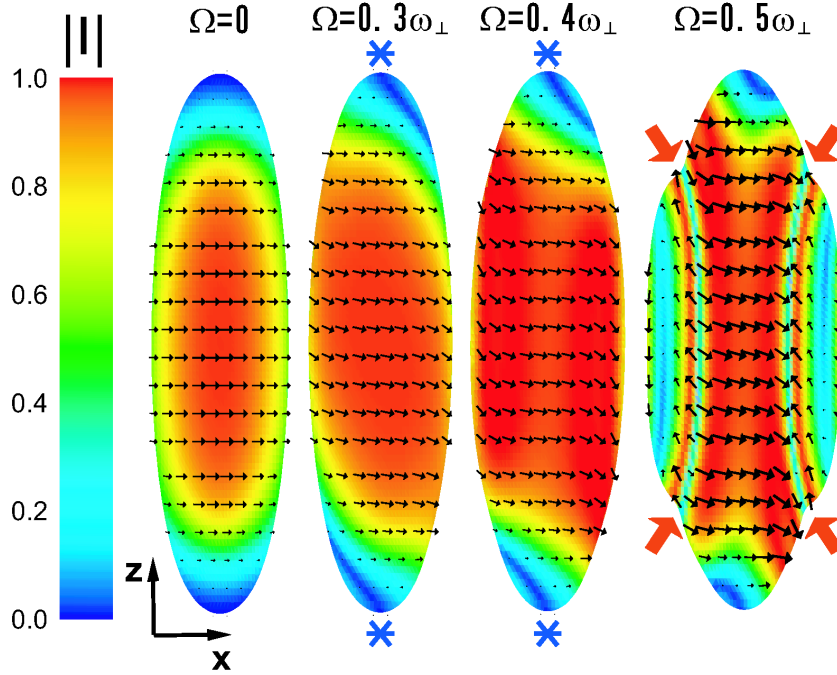


Figure 7.6: The z - x cross sections corresponding to Fig. 7.4. The l -vectors lie almost in the x - y plane at rest. Under rotation two HQVs appear, shown as asterisks. At $\Omega = 0.5\omega_{\perp}$ two pairs of the HQVs can be seen, indicated by red arrows.

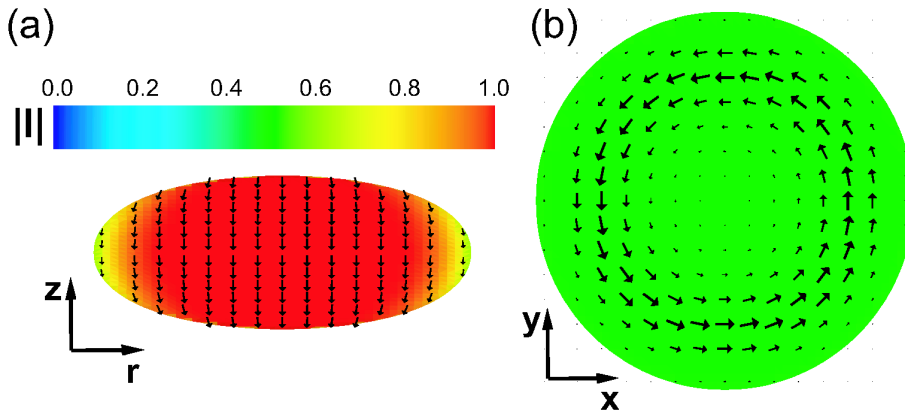


Figure 7.7: Stable texture in the pancake trap with $\lambda = 3.0$ at rest. (a) l -vector pattern in the z - r plane. The pattern is axial symmetric around z . (b) Spontaneous supercurrent in the x - y plane at $z = 0$.

the surface of condensates. This effect is especially strong when the curvature of the surface is large. Thus, in this case shown in Fig. 7.7(a), the left and right ends of the system force the l -vectors to point to the z direction, giving an overall l -vector configuration to the z direction, even for the vectors near the center. The amplitude of l -vectors decrease, namely the polar state mixes with the chiral state towards the outside.

This stable texture is axis symmetric around the z -axis, which is different in the cigar shape trap. This is because the effect of the trap potential is greater than one of the dipole-dipole interaction in the present situation ($\alpha = 0.95$), so that the chiral state consisting of the k_x and k_y components dominates over the polar state, resulting in the axis symmetric texture with respect to the z -axis. If the influence of the dipole-dipole interaction is much greater, or α becomes small, the stable texture is similar to those in the cigar shape trap.

The spatial variation of the amplitude of l -vectors towards the outer region generates a circular “orbital” supercurrent in the x - y plane as shown in Fig. 7.7(b). Since the spontaneous supercurrent flows around the external rotational axis, the axial symmetric texture is stable against low rotation.

7.4.2 Vortices under rotation

As shown in Fig. 7.8 where the x - y cross section at $z = 0$ is displayed for various rotations. Similarly to the previous texture changes in the cigar shape, we see a pair of the HQV enter from the y -axis for $\Omega = 0.3\omega_\perp$. Those vortices are exactly the same HQV as in the cigar case (see Fig. 7.4). The following sequence upon increasing Ω is very similar to the previous cigar case, slightly differing its rotation speed where in the pancake case the sequence is shifted to lower speed. We illustrate the x - z cross section at $y = 0$ in Fig. 7.9. The almost l -vectors pointing to the negative z direction at rest now deforms as Ω increases. From the right and left ends the polar state seen as blue color invades into the system. At $\Omega = 0.5\omega_\perp$ the condensate profile itself is deformed greatly because of the dominance of the polar state associated with increasing HQVs.

7.5 Quasi-2D trap

A necessary condition for Majorana zero modes to exist at a vortex core is as follows: (A) the vortex possesses an odd winding number and phase singularity in spinless chiral p -wave superfluids [97, 130] or (B) the vortex possesses one-half winding number, that is, the vortex is a HQV in spinful chiral p -wave superfluids [41].

Here, under those circumstances, we investigate experimental requirements to satisfy the condition (A) in spin polarized neutral atomic Fermi gases. In quasi-2D confinement that prohibits the Cooper pairs of the z -direction, chiral $k_x \pm ik_y$ paired states are realized unless the magnetic field for the Feshbach resonance is parallel to the quasi-2D system [122, 50]. A requirement of the quasi-2D system is $R_z \ll \xi$, namely, $\hbar\omega_z/(k_B T_c) \gg T_c/T_F$, where R_z is the radius of atomic gases toward the z -direction, ξ is the coherence length, ω_z is the trap frequency of the z -direction, T_c is the transition temperature, and T_F is the Fermi temperature. This requirement may be satisfied by the optical lattice potential of a period $\sim 3 \mu\text{m}$ [131, 132]. The aim of this study is to determine the stability condition for the singular vortex, which possesses Majorana zero energy modes at the vortex core, under the quasi-2D confinement that allows the chiral $k_x \pm ik_y$ paired state produced by the magnetic Feshbach resonance. It has been proposed that the vortices with Majorana zero modes in the p -wave resonant atomic Fermi gases are utilized for a topological quantum computer

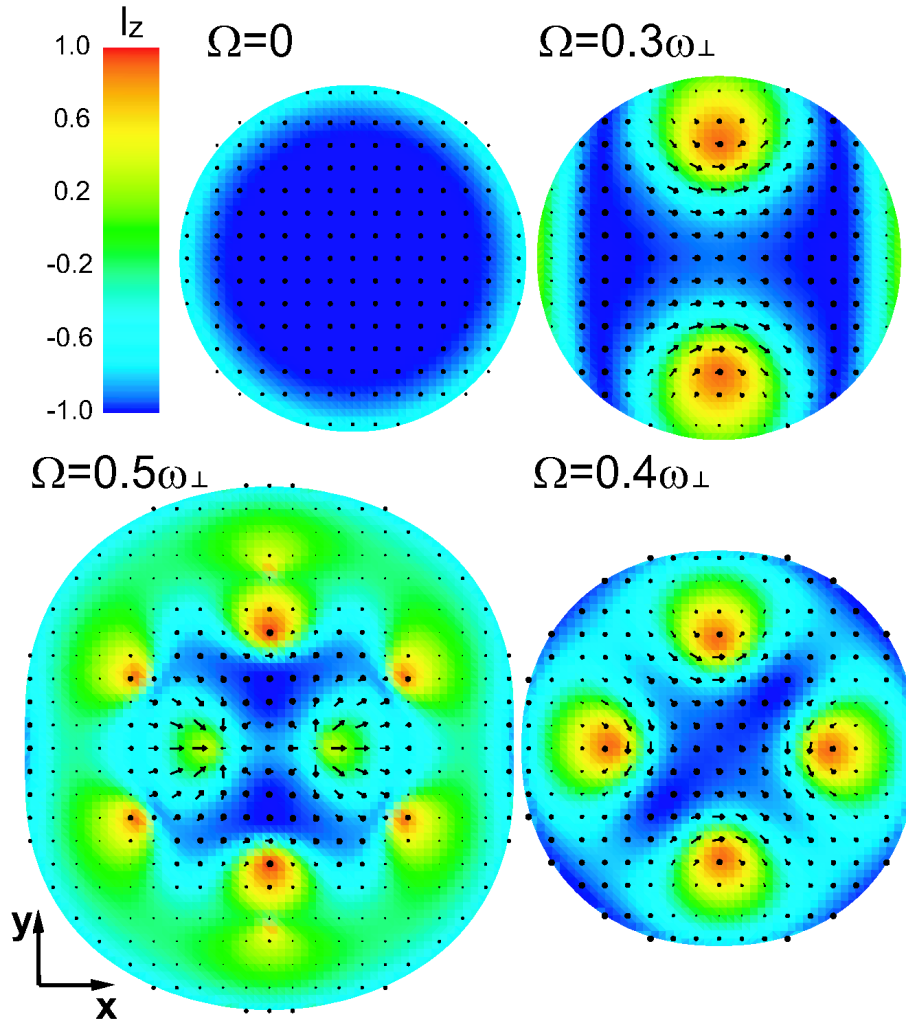


Figure 7.8: The x - y cross sectional view of the textures for the pancake shape trap with $\lambda = 3.0$ for various rotations. The two objects on the y -axis for $\Omega = 0.3\omega_{\perp}$ are the HQVs. Compare those with Fig. 7.4 in cigar shape case.

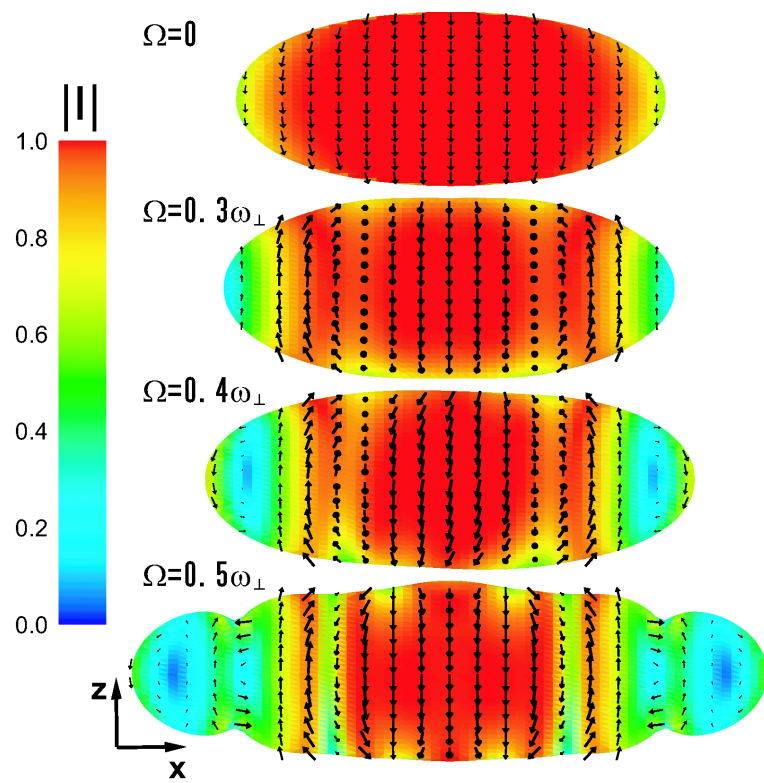


Figure 7.9: The x - z cross sectional view of the same textures in Fig. 7.8. The polar state indicated by blue color gradually enter from the right and left ends, making the system deform.

already including the optical methods of operating and reading out states of qubits [126, 63]. However, the strict stable conditions of the vortices with Majorana zero modes have not yet been discussed.

The OP of the spinless p -wave superfluidity in the quasi-2D trap potential can be expanded on the basis of rectangular coordinates with expansion coefficients A_i ($i = x, y$):

$$\Delta(\mathbf{k}) = A_x k_x + A_y k_y, \quad (7.22)$$

where \mathbf{k} is the unit vector in momentum space. We assume that the momentum toward the z -direction is prohibited by the quasi-2D trap potential.

We estimate the approximate profile of the condensates at rest within the TF approximation. In addition, we assume that the condensate is in the chiral state, which is stable in a bulk. The profile of OP amplitude is

$$|\Delta_c(r)| = \sqrt{(1-t) - \frac{3}{5}\omega^2 r^2}, \quad (7.23)$$

and the radius of condensates is

$$R_\Delta = \sqrt{\frac{5}{3} \frac{\sqrt{1-t}}{\omega}}. \quad (7.24)$$

Here, we introduce l -vector pointing in the direction of the orbital angular momentum of the Cooper pair. l -vector has only the z -component when the momentum toward the z -direction is suppressed. The z -component of l -vector is expressed with expansion coefficients on the basis of the component of the orbital angular momentum along the z -axis: $\Delta(\mathbf{k}) = A_+ k_+ + A_- k_-$. By using the coefficients,

$$l_z = \frac{|A_+|^2 - |A_-|^2}{|\Delta|^2}, \quad (7.25)$$

where $|\Delta|^2 = |A_+|^2 + |A_-|^2$ is the squared amplitude of the OP. If the condensates are purely in the chiral state, l_z has the unit value. l_z decreases when the polar state is mixed through gradient and centrifugal energies. Finally, l_z becomes zero, provided that the condensates are in the pure polar state.

7.5.1 Possible types of axisymmetric structure and a vortex

Since we assume the axisymmetric trap potential, axisymmetric structures of the condensates are stable when there is no vortex and only a singular vortex exists in the system. Here, we define the winding numbers of the plus and minus components as w_+ and w_- , respectively, where $A_\pm = |A_\pm| e^{i(w_\pm \theta + \alpha_\pm)}$ with a phase constant α_\pm . Axisymmetric structures of the OP consisting of the plus-minus components must have the combinations of the winding number $\langle w_+, w_- \rangle = \langle n-1, n+1 \rangle$, where n is an integer [133, 134]. The axisymmetric condition of what is stricter than that of multi-component spinor BECs [135]. Generally, the small winding number state is energetically favorable.

For the nonvortex structures, the possible combinations of the winding number are $\langle w_+, w_- \rangle = \langle -2, 0 \rangle$ and $\langle 0, 2 \rangle$. These structures are degenerate at rest. However, under positive rotation or counterclockwise rotation, the structure with $\langle -2, 0 \rangle$ is stable because the minus chiral component without phase winding is advantageous under positive rotation [136].

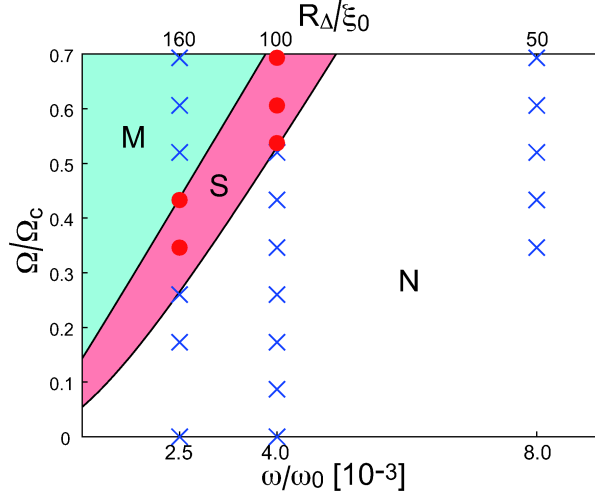


Figure 7.10: Phase diagram of the OP structures for trap frequency (ω) vs rotation frequency (Ω). The TF radii of the condensate (R_Δ) at rest are also noted. The region N is the nonvortex structure, S is the singular vortex structure where Majorana zero modes exist, and M is the multiple vortex structure. Solid circles and crosses show the structures with and without Majorana zero modes, respectively.

For the structures with a singular vortex, the possible combinations of the winding number are $\langle w_+, w_- \rangle = \langle -3, -1 \rangle$, $\langle -1, 1 \rangle$, and $\langle 1, 3 \rangle$. Among these combinations, the structure with $\langle -1, 1 \rangle$ is the most stable under low positive rotation, because the main component, which is the minus chiral component, has a winding number of 1.

Therefore, it is sufficient to consider the combination of winding number $\langle w_+, w_- \rangle = \langle -2, 0 \rangle$ for the nonvortex structure, and $\langle w_+, w_- \rangle = \langle -1, 1 \rangle$ for the structure with a singular vortex.

7.5.2 Stability region of the singular vortex

We show the phase diagram of the OP structures for trap frequency ω vs rotation frequency Ω in Fig. 7.10. We consider the three cases for the trap frequencies $\hbar\omega = 2.5, 4.0,$ and $8.0 \times 10^{-3} \sqrt{144\pi^2/35\zeta(3)} \sqrt{2\Gamma/(1+2\Gamma)} k_B T_c$. The condition of applying the GL framework $\hbar\omega \ll k_B T_c$ is satisfied because of $2\Gamma/(1+2\Gamma) < 1$. The calculated points are denoted by solid circles and crosses in Fig. 7.10. The region N is the nonvortex structure, S is the singular vortex structure where Majorana zero modes exist, and M is the multiple vortex region. Details of each structure are explained in the following subsections.

Rotation dependence

In this subsection, we show the representative structures with the trap frequency $2.5 \times 10^{-3} \omega_0$, where the TF radius of the condensate R_Δ is about $160\xi_0$ at rest. In this case, various vortex structures are stabilized by rotation.

We show the OP amplitude at rest in Figs. 7.11(a) and 7.11(b). The OP amplitude at the center is slightly suppressed from that of the chiral state in a bulk $\Delta(t) = \Delta_0 \sqrt{1-t}$. The OP amplitude is gradually decreased toward the outside by the trap potential, according

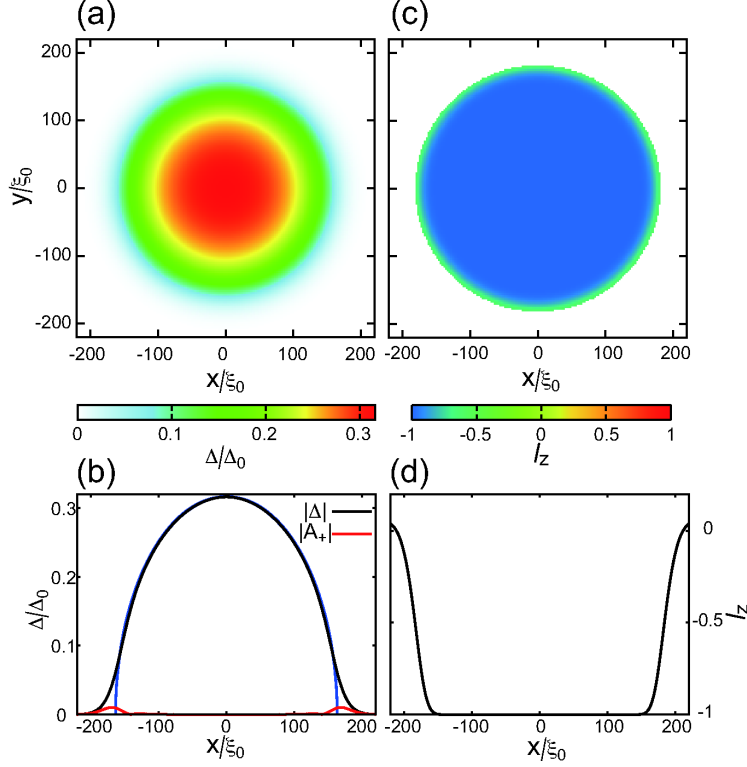


Figure 7.11: In the region N of Fig. 7.10 at rest: (a) Contour map of the OP amplitude, (b) cross sections of the OP amplitude, the plus chiral component, and TF estimate from eq. (7.23), (c) contour map of l_z where the region $\Delta/\Delta_0 \geq 0.01$ is shown, and (d) cross section of l_z .

to eq. (7.23) except near the edge. Since the condensation energy is small at the edge, the gradient energy makes a large contribution to the structures. The plus chiral component A_+ with the winding number $w_+ = -2$ is induced at the edge because the gradient energy terms in eq. (7.3), such as $A_+^*(\partial^2 A_-/\partial r^2)$, inevitably induce another component at the place where the main component A_- with the winding number $w_- = 0$ is spatially varied. The feature is absent in spinor BECs because the spatial differential operators act on real space, while the OP exists in spin space [47, 48].

This is also clear from the l_z values shown in Figs. 7.11(c) and 7.11(d). In almost all regions, $l_z = -1$, namely, the condensate is in the minus chiral state. However, the l -vectors shorten toward the outside of the condensate at the edge. The condensate is finally in the polar state.

A singular vortex enters the center of the condensate under rotation. We show the OP amplitude and the z -component of the l -vector in Fig. 7.12 at $\Omega = 0.35\Omega_c$. Since the vortex enters the condensate of the spinless chiral state and has a combination of odd winding number $\langle w_+, w_- \rangle = \langle -1, 1 \rangle$, the vortex is accompanied by Majorana zero modes. The condensate is in the minus chiral state in most of the regions; however, the plus chiral component is induced around the vortex core and at the edge. Note that the condensate at the edge is in the plus chiral state because of the effect of rotation through the gradient energy terms in eq. (7.3), such as $\Omega r A_+^*(\partial A_-/\partial r)$.

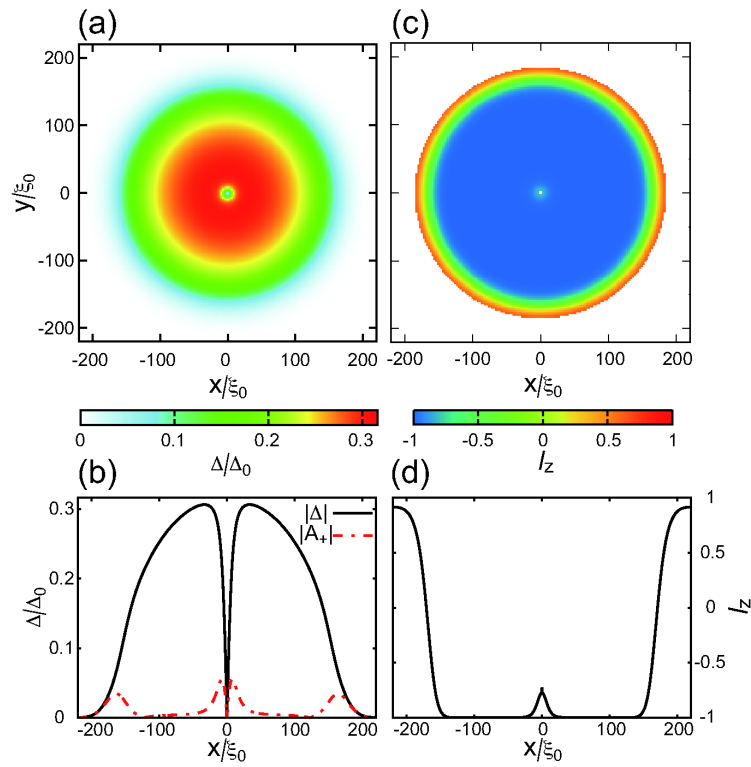


Figure 7.12: In the region S of Fig. 7.10 where a singular vortex is accompanied by Majorana zero modes at $\Omega = 0.35\Omega_c$: (a) Contour map of the OP amplitude, (b) cross sections of the OP amplitude (solid line) and the plus chiral component (dot-dash line), (c) contour map of l_z where the region $\Delta/\Delta_0 \geq 0.01$ is shown, and (d) cross section of l_z .

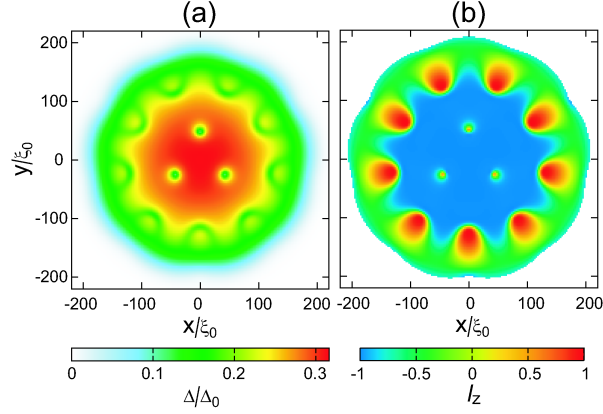


Figure 7.13: In the region M of Fig. 7.10 at $\Omega = 0.60\Omega_c$: (a) Contour map of the OP amplitude and (b) contour map of l_z where the region $\Delta/\Delta_0 \geq 0.01$ is shown.

On increasing the rotation frequency Ω , vortices enter the condensate one by one from outside. We show the OP amplitude in Fig. 7.13(a) and l_z in Fig. 7.13(b) where the condensate contains three vortices at $\Omega = 0.60\Omega_c$. All the vortices are not singular vortices in the system. The cores of the plus and minus chiral components are split and covered by the other component. The centrifugal energy, eq. (7.9), increases the condensate extension and brings the condensate at the edge into the polar state with the momentum toward the θ -direction. HQVs with $l_z = 1$ in the polar state effectively absorb the angular momentum by rotation.

Here, we introduce a pseudo-spin representation so that differences between the singular vortex and the splitting vortex can easily be seen. Since the OP has only two components, we can express the OP on the basis of the vector

$$\boldsymbol{\eta} \equiv \frac{1}{|\Delta|} \begin{pmatrix} A_+ \\ A_- \end{pmatrix}. \quad (7.26)$$

The pseudo-spin is defined using the vectors and Pauli matrices with the total spin $1/2$.

$$\begin{aligned} S_x &\equiv \frac{1}{2} \boldsymbol{\eta}^\dagger \sigma_x \boldsymbol{\eta} = \frac{1}{|\Delta|^2} \text{Re}(A_+^* A_-), \\ S_y &\equiv \frac{1}{2} \boldsymbol{\eta}^\dagger \sigma_y \boldsymbol{\eta} = \frac{1}{|\Delta|^2} \text{Im}(A_+^* A_-), \\ S_z &\equiv \frac{1}{2} \boldsymbol{\eta}^\dagger \sigma_z \boldsymbol{\eta} = \frac{1}{2} \frac{|A_+|^2 - |A_-|^2}{|\Delta|^2}. \end{aligned} \quad (7.27)$$

The z -component of the pseudo-spin S_z is one-half of l_z .

We define the topological charge $N \equiv w_- - w_+$. Axisymmetric vortices have the topological charge $N = 2$ and the HQVs with the combinations of the winding number $\langle w_+, w_- \rangle =$

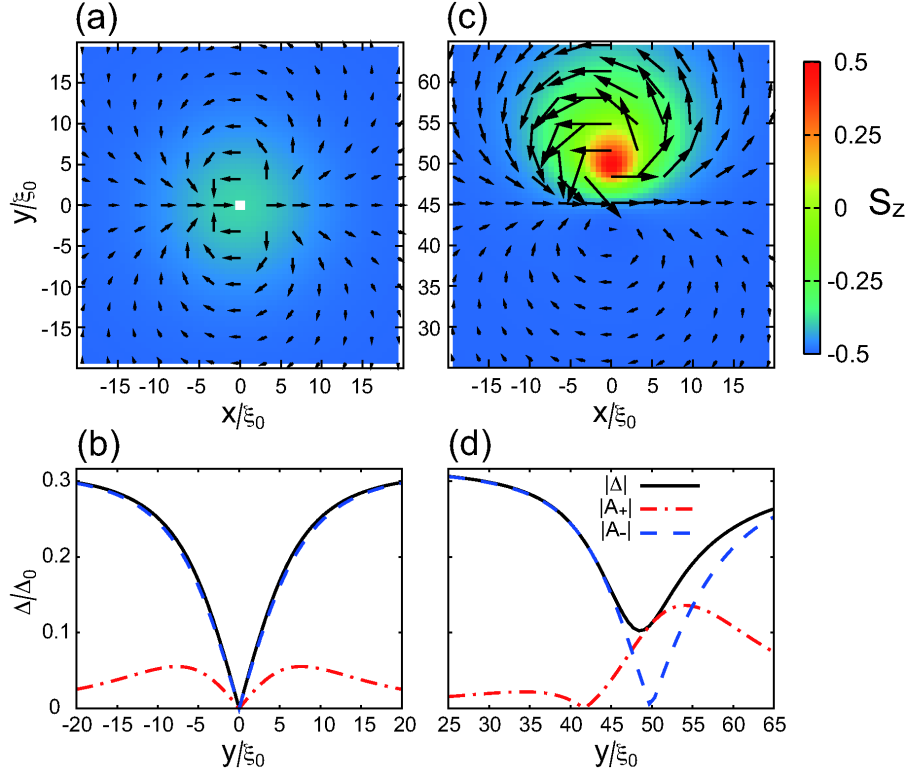


Figure 7.14: Pseudo-spin vectors (S_x, S_y) with the contour of the S_z component (a) around a singular vortex at $\Omega = 0.35\Omega_c$ (Fig. 7.12) and (c) around a splitting vortex at $\Omega = 0.60\Omega_c$ (Fig. 7.13). Cross sections of the OP amplitude (solid line), the plus chiral component (dot-dash line), and minus chiral component (dashed line) (b) across a singular vortex and (d) across a splitting vortex.

$\langle -1, 0 \rangle$ and $\langle 1, 0 \rangle$ have $N = 1$. The pseudo-spin can be rewritten with the topological charge:

$$\begin{aligned}
 S_x &= \frac{|A_+ A_-|}{|\Delta|^2} \cos(N\theta + \alpha'), \\
 S_y &= \frac{|A_+ A_-|}{|\Delta|^2} \sin(N\theta + \alpha'), \\
 S_z &= \frac{1}{2} \frac{|A_+|^2 - |A_-|^2}{|\Delta|^2},
 \end{aligned} \tag{7.28}$$

where the relative phase $\alpha' = \alpha_- - \alpha_+$. The pseudo-spin vector (S_x, S_y) rotates N times around a vortex with the topological charge N [137].

The axisymmetric singular vortex at the center of the condensate at $\Omega = 0.35\Omega_c$ has the topological charge $N = 2$ (Figs. 7.14(a) and 7.14(b)). Similarly, the vortices at $\Omega = 0.60\Omega_c$ have the topological charge $N = 2$ around a path far away from them (Figs. 7.14(c) and 7.14(d)). However, they are split into two HQVs with $N = 1$ because of the OP amplitude around the off-centered vortices without axisymmetry by a harmonic trap potential. The HQVs on the y -axis with the combinations of the winding number $\langle -1, 0 \rangle$ and $\langle 0, 1 \rangle$ are located on $(0, 42\xi_0)$ and $(0, 50\xi_0)$, respectively, in Fig. 7.14(d). The distance between two

HQVs is approximately $8\xi_0 \approx 3\xi(t)$, where $\xi(t) = \xi_0(1-t)^{-1/2}$ is the temperature-dependent coherence length.

Since the off-centered vortex has a finite OP everywhere, Majorana zero modes, which are zero energy excitations, may not exist. Note, however, that the vortex situated at a few times of coherence length is similar to the singular vortex with Majorana zero modes. The quasi-particle states of the off-centered vortex are unknown at present. We must solve the Bogoliubov-de Gennes equations in order to understand the quasi-particle states. This is our future problem.

Trapping dependence

The number of vortices is proportional to the rotation frequency and the system size, or the cross section that is perpendicular to the rotational axis. The radius of the condensate is inversely proportional to the trap frequency and is increased by the centrifugal energy under rotation. Since the effect of the centrifugal energy differs among orbital states, the region of the polar state appears predominantly at the edge of the condensate under high rotation. Therefore, the number of vortices in the chiral state situated in the central region does not increase with increasing rotation because the angular momentum is absorbed by HQVs in the polar state at the surrounding area, which prevent the vortex from entering the central region.

The vortex does not enter the chiral state up to high rotation in the case of $\omega = 8.0 \times 10^{-3}\omega_0$ and only the singular vortex enters under high rotation in the case of $\omega = 4.0 \times 10^{-3}\omega_0$. Namely, we will have to employ a low trap frequency in an experiment to observe Majorana zero modes. In the previous section under a 3D pancake-shape trap potential, the major radius of the condensate was approximately $30\xi_0$, which corresponds to high-trap-frequency cases in this section; therefore, the polar core vortex with a combination of winding number $\langle w_+, w_0, w_- \rangle = \langle -1, 0, 1 \rangle$, which corresponds to the singular vortex $\langle w_+, w_- \rangle = \langle -1, 1 \rangle$, did not enter the condensate.

7.6 Summary

By minimizing the generic GL energy functional within weak-coupling approximation, we find stable textures for *p*-wave superfluids in neutral atomic gases confined in 3D harmonic trap potentials which are to be realized in near future. In order to help detecting its superfluidity, we examine two typical trap geometries, cigar and pancake shapes. At rest, the obtained stable textures in both shapes exhibit the spontaneous supercurrent flow. Under rotation, a pair of the HQVs enters in the condensates. The isolated HQV is never stabilized in our calculations because of topological constrains.

It is interesting to note that the direction of the spontaneously generated supercurrent at rest is always perpendicular to the direction of the majority *l*-vectors, that is, the condensates in the cigar and pancake case *l*-vectors lie on the *x-y* plane and point to the *z* direction, respectively, so the supercurrent flows toward the *z* direction and in the *x-y* plane. This implies that the trap shape is critical in understanding and controlling the physics of the textures on the *p*-wave superfluid.

In the systems confined in the quasi-2D harmonic trap potential with a low frequency, the singular vortex accompanied by Majorana zero modes enters the center of the condensates under rotation. Under high rotation, the multiple vortex state is stabilized. The off-centered vortices in the multiple vortex state are split into two HQVs and are not accompanied by

Majorana zero modes; the quasi-particle states of the off-centered vortex are unknown at present. Note that a centered singular vortex is accompanied by Majorana zero modes even though some vortices exist in the chiral state.

Within the present quasi-2D harmonic trap potential, there is no stable parameter region in the (ω, Ω) plane for plural singular vortices, which is necessary for a topological quantum computer. We suggest the use of a quasi-2D square well potential for confinement, which is also used in the superfluid ^3He confined in parallel plates [44, 42]. This could accommodate a pair of singular vortices or more.

Chapter 8

Conclusion

8.1 Summary of this thesis

We have investigated textures and Majorana excitations such as Majorana quasi-particles (QPs) and Majorana fermions in the superfluid ^3He and p -wave resonant superfluids of Fermi atomic gases.

Textures in the superfluid ^3He A-phase confined in a narrow cylinder have been discussed in Chap. 5. Under magnetic fields larger than ~ 2 mT toward the cylindrical axis, l -vector forms radial disgyration (RD) at rest and Mermin-Ho (MH) texture under rotation. For a cylinder with radius $R = 50 \mu\text{m}$, d -vector forms hyperbolic type (hb); on the other hand, for a cylinder with radius $R = 115 \mu\text{m}$, d -vector tends to form axial type (ax). Therefore, by rotation, RD-hb changes to MH-hb in the $R = 50 \mu\text{m}$ cylinder and RD-ax changes to MH-hb in the $R = 115 \mu\text{m}$ [19, 20]. The results correspond to results of the experiment in ISSP, Univ. of Tokyo [77, 78, 79, 80, 81].

Character of Majorana excitations is different in the superfluid ^3He A- and B-phases, which have the same topological features of the spin Hall state and quantum spin Hall state, respectively. Majorana excitations in the superfluid ^3He A- and B-phases confined in a thin slab have been discussed in Chap. 6. In the A-phase, Majorana QPs and Majorana fermions exist at the side edge of the slab and dispersion relation forms “Dirac valley” [21, 22, 23]. Accompanying the Majorana excitations, mass current flow along the side edge. This mass current has the projection of angular momentum $\sim N\hbar/2$, where N is the number of ^3He atoms. In the B-phase, Majorana fermions exist at the all surface of the slab and dispersion relation forms Majorana cone. Accompanying the Majorana fermions, spin current flow along the surface three-dimensionally. If thickness of the slab is short, however, the zero energy modes of the Majorana fermions at upper and lower surfaces are split.

Textures and Majorana QPs in p -wave resonant superfluids of Fermi atomic gases have been discussed in Chap. 7. The p -wave resonant superfluids in three-dimensional trap potential form different textures from the superfluid ^3He [24, 25]. l -vector tends to align parallel to the circumference of the condensate and spontaneous mass current flow three-dimensionally even at rest. Under rotation, pairs of half-quantum vortices (HQVs) enter in the condensate. In quasi-two-dimensional trap potential, we have derived conditions to realize a singular vortex with a Majorana QP for trap frequency and rotation frequency [26].

8.2 Future studies

The mass current accompanying the Majorana excitations in the superfluid ^3He A-phase along the side edge of a slab has the projection of angular momentum $\sim N\hbar/2$. The value of the projection of the angular momentum is the same as that of the intrinsic angular momentum (IAM) by Cooper pairs of chiral p -wave superfluids. Relation between their angular momentum is a future study. If Cooper pairs consist of all atoms in the Fermi sea, the projection of the IAM is $\sim N\hbar/2$; on the other hand, if Cooper pairs consist of atoms near the Fermi level, the projection of the IAM is $\sim N\hbar/2(\Delta/E_F)^2$. Then, the problem of the IAM relates to the base of superconductivity and superfluidity. The relation may answer the problem of the IAM had been discussed for more than three decades.

HQVs in the superfluid ^3He have been investigated by NMR experiment; however, clear evidence of them has not observed yet [44]. The HQVs are stabilized by the Fermi liquid correction [40]; on the other hand, they are unstable under the strong-coupling effect by pressure [42, 43]. Then, the HQVs are unstable in the ordinary A-phase at high pressure and high temperature because the strong-coupling effect is greater than the Fermi liquid correction [138]. In thin slab with the thickness of the order of several times of the coherence length, however, the stable region of the A-phase is enlarged toward low pressure [139]. In the A-phase at the low pressure, the HQVs are stabilized by the only Fermi liquid correction. A left subject is how to observe the HQVs. We may answer it to study the magnetic response of the lattice of the HQV pairs by the quasi-classical theory.

Investigation of textures in the p -wave resonant superfluids of Fermi atomic gasses is only our investigation by the Ginzburg-Landau theory. After realizing the p -wave resonant superfluids, we should do a study based on the microscopic theory to derive quantitative results.

Appendix A

Symmetry of quasi-classical Green's function

We use the symmetry of the quasi-classical Green's function in Eilenberger Eq. (6.1) to reduce computational time. If we replace Matsubara frequency ω_n with $-\omega_n^*$, the quasi-classical Green's functions in Nambu space have relations

$$\begin{aligned}\hat{g}(\mathbf{r}, \mathbf{k}, -\omega_n^*) &= -\hat{g}(\mathbf{r}, \mathbf{k}, \omega_n)^\dagger, & \underline{\hat{g}}(\mathbf{r}, \mathbf{k}, -\omega_n^*) &= -\underline{\hat{g}}(\mathbf{r}, \mathbf{k}, \omega_n)^\dagger, \\ \hat{f}(\mathbf{r}, \mathbf{k}, -\omega_n^*) &= \underline{\hat{f}}(\mathbf{r}, \mathbf{k}, \omega_n)^\dagger, & \underline{\hat{f}}(\mathbf{r}, \mathbf{k}, -\omega_n^*) &= \hat{f}(\mathbf{r}, \mathbf{k}, \omega_n)^\dagger,\end{aligned}\quad (\text{A.1})$$

where we describe the complex conjugate of the Matsubara frequency explicitly because that is important when we calculate local density of states (LDOS). By the relations, we are allowed to sum only the positive ω_n to calculate self-consistent pair potential and mass and spin currents.

If we reverse the sign of relative momentum \mathbf{k} , the sign of spin-triplet components of the order parameter (OP) changes; on the other hand, that of a spin singlet component of the OP does not change. Specifically, general OP

$$\hat{\Delta}(\mathbf{r}, \mathbf{k}) = \begin{pmatrix} \Delta_{\uparrow\uparrow}(\mathbf{r}, \mathbf{k}) & \Delta_{\uparrow\downarrow}(\mathbf{r}, \mathbf{k}) \\ \Delta_{\downarrow\uparrow}(\mathbf{r}, \mathbf{k}) & \Delta_{\downarrow\downarrow}(\mathbf{r}, \mathbf{k}) \end{pmatrix}$$

has a relation, $\hat{\Delta}(\mathbf{r}, -\mathbf{k}) = -\hat{\Delta}^T(\mathbf{r}, \mathbf{k})$, where a superscript T indicates transposition of a matrix. Since the sign of Fermi velocity also changes, $\mathbf{v}(-\mathbf{k}) = -\mathbf{v}(\mathbf{k})$, the quasi-classical Green's functions in particle-hole space have relations

$$\begin{aligned}\hat{g}(\mathbf{r}, -\mathbf{k}, \omega_n^*) &= \underline{\hat{g}}(\mathbf{r}, \mathbf{k}, \omega_n)^*, & \underline{\hat{g}}(\mathbf{r}, -\mathbf{k}, \omega_n^*) &= \hat{g}(\mathbf{r}, \mathbf{k}, \omega_n)^*, \\ \hat{f}(\mathbf{r}, -\mathbf{k}, \omega_n^*) &= -\underline{\hat{f}}(\mathbf{r}, \mathbf{k}, \omega_n)^*, & \underline{\hat{f}}(\mathbf{r}, -\mathbf{k}, \omega_n^*) &= -\hat{f}(\mathbf{r}, \mathbf{k}, \omega_n)^*.\end{aligned}\quad (\text{A.2})$$

More reduction of computational time is possible by using mirror operators which define $S_x \mathbf{a} \equiv (-a_x, a_y, a_z)$, $S_z \mathbf{a} \equiv (a_x, a_y, -a_z)$, and $S_{xz} \mathbf{a} \equiv (-a_x, a_y, -a_z)$ with an arbitrary vector $\mathbf{a} = (a_x, a_y, a_z)$. If the mirror operators act on the center-of-mass coordinate of pair potential under the antiperiodic boundary condition mentioned in Sec. 6.2, $\Delta(S\mathbf{r}, \mathbf{k}) = \Delta(\mathbf{r}, S\mathbf{k})$, where S is one among S_x , S_z , and S_{xz} . Since $S\mathbf{v} \cdot S\nabla = \mathbf{v} \cdot \nabla$, the quasi-classical Green's function satisfies

$$\hat{g}(S\mathbf{r}, S\mathbf{k}, \omega_n) = \hat{g}(\mathbf{r}, \mathbf{k}, \omega_n). \quad (\text{A.3})$$

Therefore, the quasi-classical Green's function and pair potential are self-consistently obtained by numerical calculation for only the positive Matsubara frequency and one eighth of the Fermi surface in the coordinate $-L/2 \leq x \leq L/2$ and $-D/2 \leq z \leq D/2$ by the symmetry of the quasi-classical Green's function (A.1), (A.2), and (A.3). The calculation for the real space coordinates is carried out by parallel computing with OpenMP.

Appendix B

Angular momentum of the A-phase in a slab

We consider a slab with a thickness D along the z -direction and a macroscopic length of $2R$ along the x -direction. If the superfluid ^3He A-phase is confined in the slab with $D \leq 8\xi_0$, l -vector and d -vector point to the z -direction and they are uniform toward the z -direction, shown in Sec. 6.3.1. When a edge is at $x = 0$, a model order parameter is

$$\begin{aligned}\hat{\Delta}(x, \mathbf{k}) &= \begin{pmatrix} 0 & \Delta [\tanh(x/\xi)k_x + ik_y] \\ \Delta [\tanh(x/\xi)k_x + ik_y] & 0 \end{pmatrix} \\ &= \begin{pmatrix} 0 & \Delta \sin \theta [\cos \phi \tanh(x/\xi) + i \sin \phi] \\ \Delta \sin \theta [\cos \phi \tanh(x/\xi) + i \sin \phi] & 0 \end{pmatrix},\end{aligned}\quad (\text{B.1})$$

where $k_x = \cos \phi \sin \theta$, $k_y = \sin \phi \sin \theta$, $\xi = \hbar v_F / \Delta$, and Δ can be taken as positive real. Then, Riccati equations (6.3) are regarded as scalar equations:

$$\begin{aligned}\hbar v_F \cos \phi \sin \theta \frac{\partial a(x, \mathbf{k}, \omega_n)}{\partial x} &= \Delta \sin \theta \left[\cos \phi \tanh \left(\frac{x}{\xi} \right) + i \sin \phi \right] - 2\omega_n a(x, \mathbf{k}, \omega_n) \\ &\quad - \Delta \sin \theta \left[\cos \phi \tanh \left(\frac{x}{\xi} \right) - i \sin \phi \right] a^2(x, \mathbf{k}, \omega_n), \\ -\hbar v_F \cos \phi \sin \theta \frac{\partial b(x, \mathbf{k}, \omega_n)}{\partial x} &= \Delta \sin \theta \left[\cos \phi \tanh \left(\frac{x}{\xi} \right) - i \sin \phi \right] - 2\omega_n b(x, \mathbf{k}, \omega_n) \\ &\quad - \Delta \sin \theta \left[\cos \phi \tanh \left(\frac{x}{\xi} \right) + i \sin \phi \right] b^2(x, \mathbf{k}, \omega_n),\end{aligned}\quad (\text{B.2})$$

where Matsubara frequency is $\omega_n = (2n + 1)\pi k_B T$ and matrices of Riccati amplitude are

$$\hat{a}(x, \mathbf{k}, \omega_n) = \begin{pmatrix} 0 & a(x, \mathbf{k}, \omega_n) \\ a(x, \mathbf{k}, \omega_n) & 0 \end{pmatrix}, \quad \hat{b}(x, \mathbf{k}, \omega_n) = \begin{pmatrix} 0 & b(x, \mathbf{k}, \omega_n) \\ b(x, \mathbf{k}, \omega_n) & 0 \end{pmatrix}.\quad (\text{B.3})$$

These solutions are

$$\begin{aligned}a(x, \mathbf{k}, \omega_n) &= \frac{\omega_n - \sqrt{\omega_n^2 + \Delta^2 \sin^2 \theta} + \Delta \sin \theta [\cos \phi \tanh(x/\xi) + i \sin \phi]}{\omega_n + \sqrt{\omega_n^2 + \Delta^2 \sin^2 \theta} - \Delta \sin \theta [\cos \phi \tanh(x/\xi) - i \sin \phi]}, \\ b(x, \mathbf{k}, \omega_n) &= -\frac{\omega_n - \sqrt{\omega_n^2 + \Delta^2 \sin^2 \theta} - \Delta \sin \theta [\cos \phi \tanh(x/\xi) - i \sin \phi]}{\omega_n + \sqrt{\omega_n^2 + \Delta^2 \sin^2 \theta} + \Delta \sin \theta [\cos \phi \tanh(x/\xi) + i \sin \phi]}.\end{aligned}\quad (\text{B.4})$$

From eqs. (6.2), (6.4), and (6.15), quasi-classical Green's function is

$$\begin{aligned} g_0(x, \mathbf{k}, \omega_n) &= \frac{1 - a(x, \mathbf{k}, \omega_n)b(x, \mathbf{k}, \omega_n)}{1 + a(x, \mathbf{k}, \omega_n)b(x, \mathbf{k}, \omega_n)} \\ &= \frac{1}{\sqrt{\omega_n^2 + \Delta^2 \sin^2 \theta}} \left[\omega_n + \frac{\Delta^2 \sin^2 \theta \cos^2 \phi}{2(\omega_n + i\Delta \sin \theta \sin \phi)} \operatorname{sech}^2 \left(\frac{x}{\xi} \right) \right]. \end{aligned} \quad (\text{B.5})$$

B.1 Angular momentum by Matsubara Green's function

From eq. (6.13), mass current is

$$j_i(x) = mv_F N_0 \pi k_B T \sum_{\omega_n} \langle k_i \operatorname{Im} [g_0(x, \mathbf{k}, \omega_n)] \rangle_{\mathbf{k}}. \quad (\text{B.6})$$

Here,

$$\begin{aligned} \operatorname{Im} [g_0(x, \mathbf{k}, \omega_n)] &= - \frac{1}{2\sqrt{\omega_n^2 + \Delta^2 \sin^2 \theta}} \frac{\Delta^3 \sin^3 \theta \sin \phi \cos^2 \phi}{\omega_n^2 + \Delta^2 \sin^2 \theta \sin^2 \phi} \operatorname{sech}^2 \left(\frac{x}{\xi} \right) \\ &= - \frac{1}{2\sqrt{\omega_n^2 + \Delta^2(k_x^2 + k_y^2)}} \frac{\Delta^3 k_x^2 k_y}{\omega_n^2 + \Delta^2 k_y^2} \operatorname{sech}^2 \left(\frac{x}{\xi} \right). \end{aligned} \quad (\text{B.7})$$

For Fermi surface average, mass current has only the y -component. Since $\operatorname{Im}[g_0]$ is even function for ω_n , the y -component of mass current is

$$j_y(x) = 2mv_F N_0 \pi k_B T \sum_{\omega_n > 0} \int_0^\pi \frac{d\theta \sin \theta}{2} \int_0^{2\pi} \frac{d\phi}{2\pi} \sin \phi \sin \theta \operatorname{Im} [g_0(x, \mathbf{k}, \omega_n)]. \quad (\text{B.8})$$

By the ϕ -integration,

$$\begin{aligned} & \int_0^{2\pi} \frac{d\phi}{2\pi} \sin \phi \operatorname{Im} [g_0(x, \mathbf{k}, \omega_n)] \\ &= - \frac{\Delta^3 \sin^3 \theta}{2\sqrt{\omega_n^2 + \Delta^2 \sin^2 \theta}} \operatorname{sech}^2 \left(\frac{x}{\xi} \right) \int_0^{2\pi} \frac{d\phi}{2\pi} \frac{\sin^2 \phi \cos^2 \phi}{\omega_n^2 + \Delta^2 \sin^2 \theta \sin^2 \phi} \\ &= - \frac{\Delta^3 \sin^3 \theta}{2\sqrt{\omega_n^2 + \Delta^2 \sin^2 \theta}} \operatorname{sech}^2 \left(\frac{x}{\xi} \right) \frac{2\omega_n^2 + \Delta^2 \sin^2 \theta - 2\omega_n \sqrt{\omega_n^2 + \Delta^2 \sin^2 \theta}}{2\Delta^4 \sin^4 \theta} \\ &= - \frac{1}{4\Delta \sin \theta} \left[\sqrt{\omega_n^2 + \Delta^2 \sin^2 \theta} + \frac{\omega_n^2}{\sqrt{\omega_n^2 + \Delta^2 \sin^2 \theta}} - 2\omega_n \right] \operatorname{sech}^2 \left(\frac{x}{\xi} \right). \end{aligned} \quad (\text{B.9})$$

By the θ -integration,

$$\begin{aligned} & \int_0^\pi \frac{d\theta \sin^2 \theta}{2} \int_0^{2\pi} \frac{d\phi}{2\pi} \sin \phi \operatorname{Im} [g_0(x, \mathbf{k}, \omega_n)] \\ &= - \frac{1}{8\Delta} \operatorname{sech}^2 \left(\frac{x}{\xi} \right) \int_0^\pi d\theta \sin \theta \left[\sqrt{\omega_n^2 + \Delta^2 \sin^2 \theta} + \frac{\omega_n^2}{\sqrt{\omega_n^2 + \Delta^2 \sin^2 \theta}} - 2\omega_n \right] \\ &= - \frac{1}{8\Delta} \operatorname{sech}^2 \left(\frac{x}{\xi} \right) \left[\frac{3\omega_n^2 + \Delta^2}{\Delta} \sin^{-1} \frac{\Delta}{\sqrt{\omega_n^2 + \Delta^2}} - 3\omega_n \right]. \end{aligned} \quad (\text{B.10})$$

Therefore,

$$j_y(x) = -\frac{mv_F N_0}{4\Delta} \operatorname{sech}^2\left(\frac{x}{\xi}\right) \pi k_B T \sum_{\omega_n > 0} \left[\frac{3\omega_n^2 + \Delta^2}{\Delta} \sin^{-1} \frac{\Delta}{\sqrt{\omega_n^2 + \Delta^2}} - 3\omega_n \right]. \quad (\text{B.11})$$

In low temperature limit, summation of $\omega_n = (2n+1)\pi k_B T$ can be replaced by integration:

$$\begin{aligned} & \pi k_B T \sum_{\omega_n > 0} \left[\frac{3\omega_n^2 + \Delta^2}{\Delta} \sin^{-1} \frac{\Delta}{\sqrt{\omega_n^2 + \Delta^2}} - 3\omega_n \right] \\ & \approx \pi k_B T \int_0^\infty \frac{d\omega}{2\pi k_B T} \left[\frac{3\omega^2 + \Delta^2}{\Delta} \sin^{-1} \frac{\Delta}{\sqrt{\omega^2 + \Delta^2}} - 3\omega \right] \\ & = \frac{1}{2} \lim_{\omega \rightarrow \infty} \left[\frac{\omega}{\Delta} (\omega^2 + \Delta^2) \sin^{-1} \frac{\Delta}{\sqrt{\omega^2 + \Delta^2}} - \omega^2 \right] \\ & = \frac{1}{2} \lim_{\omega \rightarrow \infty} \left[\frac{\omega}{\Delta} (\omega^2 + \Delta^2) \left\{ \frac{\Delta}{\sqrt{\omega^2 + \Delta^2}} + \frac{1}{6} \frac{\Delta^3}{(\omega^2 + \Delta^2)^{3/2}} \right\} - \omega^2 \right] \\ & = \frac{\Delta^2}{3}. \end{aligned} \quad (\text{B.12})$$

Finally, mass current is

$$j_y(x) = -\frac{mv_F N_0 \Delta}{12} \operatorname{sech}^2\left(\frac{x}{\xi}\right). \quad (\text{B.13})$$

Angular momentum of the system is derived by extending a edge circularly. Then,

$$\begin{aligned} L_z &= 2\pi R D \int_R^0 dx j_y(x) (R-x) \\ &= \frac{mv_F N_0 \Delta}{6} \pi R D \int_0^R dx (R-x) \operatorname{sech}^2\left(\frac{x}{\xi}\right) \\ &= \frac{mv_F N_0 \Delta}{6} \pi R D \xi^2 \ln\left(\cosh \frac{R}{\xi}\right) \\ &\approx \frac{mv_F N_0 \Delta}{6} \xi \pi R^2 D, \end{aligned} \quad (\text{B.14})$$

because $R \gg \xi$. Since $\xi = \hbar v_F / \Delta$ and

$$N_0 = \frac{mk_F}{\pi^2 \hbar^2} = \frac{mk_F}{\pi^2 \hbar^2} \frac{1}{v_F^2} \left(\frac{\hbar k_F}{m} \right)^2 = \frac{3}{mv_F^2} \frac{k_F^3}{3\pi^2} = \frac{3}{mv_F^2} \frac{N}{V} = \frac{3N}{mv_F^2 \pi R^2 D}, \quad (\text{B.15})$$

angular momentum is

$$L_z = \frac{N\hbar}{2}. \quad (\text{B.16})$$

B.2 Angular momentum by retarded Green's function

Quasi-classical retarded Green's function is derived by analytic continuation of quasi-classical Matsubara Green's function as

$$\hat{g}_0^R(x, \mathbf{k}, E) = \hat{g}_0(x, \mathbf{k}, \omega_n)|_{i\omega_n \rightarrow E+i\eta}, \quad (\text{B.17})$$

where η is infinitesimal positive constant. From eq. (B.5), quasi-classical retarded Green's function is

$$\begin{aligned} g_0^R(x, \mathbf{k}, E) &= \frac{1}{\sqrt{\Delta^2 \sin^2 \theta - E^2 - i\eta \operatorname{sgn}(E)}} \left[-iE + \frac{\Delta^2 \sin^2 \theta \cos^2 \phi}{\eta + 2i(\Delta \sin \theta \sin \phi - E)} \operatorname{sech}^2 \left(\frac{x}{\xi} \right) \right] \\ &= \frac{1}{\sqrt{\Delta^2 (k_x^2 + k_y^2) - E^2 - i\eta \operatorname{sgn}(E)}} \left[-iE + \frac{\Delta^2 k_x^2}{\eta + 2i(\Delta k_y - E)} \operatorname{sech}^2 \left(\frac{x}{\xi} \right) \right], \end{aligned} \quad (\text{B.18})$$

where $\operatorname{sgn}(E) \equiv E/|E|$. Mass current by retarded Green's function is

$$j_i(x) = mv_F N_0 \int_{-\infty}^0 dE \langle k_i \operatorname{Re} [g_0^R(x, \mathbf{k}, E)] \rangle_{\mathbf{k}}. \quad (\text{B.19})$$

For Fermi surface average, mass current has only the y -component. The y -component of mass current is

$$j_y(x) = mv_F N_0 \int_{-\infty}^0 dE \int_0^\pi \frac{d\theta \sin \theta}{2} \int_0^{2\pi} \frac{d\phi}{2\pi} \sin \phi \sin \theta \operatorname{Re} [g_0^R(x, \mathbf{k}, E)]. \quad (\text{B.20})$$

For the bound state $-\Delta \sin \theta < E < 0$,

$$g_0^R(x, \mathbf{k}, E) = \frac{1}{\sqrt{\Delta^2 \sin^2 \theta - E^2}} \left[-iE + \frac{\Delta^2 \sin^2 \theta \cos^2 \phi}{\eta + 2i(\Delta \sin \theta \sin \phi - E)} \operatorname{sech}^2 \left(\frac{x}{\xi} \right) \right]. \quad (\text{B.21})$$

Here,

$$\begin{aligned} &\operatorname{Re} [g_0^R(x, \mathbf{k}, E)] \\ &= \pi \frac{\Delta^2 \sin^2 \theta \cos^2 \phi}{\sqrt{\Delta^2 \sin^2 \theta - E^2}} \frac{-1}{2\pi i} \left[\frac{1}{2(\Delta \sin \theta \sin \phi - E) + i\eta} - \frac{1}{2(\Delta \sin \theta \sin \phi - E) - i\eta} \right] \operatorname{sech}^2 \left(\frac{x}{\xi} \right) \\ &= \pi \frac{\Delta^2 \sin^2 \theta \cos^2 \phi}{\sqrt{\Delta^2 \sin^2 \theta - E^2}} \delta[2(\Delta \sin \theta \sin \phi - E)] \operatorname{sech}^2 \left(\frac{x}{\xi} \right). \end{aligned} \quad (\text{B.22})$$

By the ϕ -integration,

$$\begin{aligned} &\int_0^{2\pi} \frac{d\phi}{2\pi} \sin \phi \operatorname{Re} [g_0^R(x, \mathbf{k}, E)] \\ &= \frac{\Delta^2 \sin^2 \theta}{2\sqrt{\Delta^2 \sin^2 \theta - E^2}} \operatorname{sech}^2 \left(\frac{x}{\xi} \right) \int_0^{2\pi} d\phi \sin \phi \cos^2 \phi \delta[2(\Delta \sin \theta \sin \phi - E)] \\ &= \frac{\Delta \sin \theta}{4\sqrt{\Delta^2 \sin^2 \theta - E^2}} \operatorname{sech}^2 \left(\frac{x}{\xi} \right) \\ &\quad \times \left[\int_{-1}^1 dx x \sqrt{1-x^2} \delta \left(x - \frac{E}{\Delta \sin \theta} \right) + \int_1^{-1} dx x \left(-\sqrt{1-x^2} \right) \delta \left(x - \frac{E}{\Delta \sin \theta} \right) \right] \\ &= \frac{E}{2\Delta \sin \theta} \operatorname{sech}^2 \left(\frac{x}{\xi} \right). \end{aligned} \quad (\text{B.23})$$

By the energy-integration,

$$\int_{-\Delta \sin \theta}^0 dE \int_0^{2\pi} \frac{d\phi}{2\pi} \sin \phi \operatorname{Re} [g_0^R(x, \mathbf{k}, E)] = -\frac{\Delta \sin \theta}{4} \operatorname{sech}^2 \left(\frac{x}{\xi} \right). \quad (\text{B.24})$$

By the θ -integration,

$$\int_0^\pi \frac{d\theta \sin^2 \theta}{2} \int_{-\Delta \sin \theta}^0 dE \int_0^{2\pi} \frac{d\phi}{2\pi} \sin \phi \operatorname{Re} [g_0^R(x, \mathbf{k}, E)] = -\frac{\Delta}{6} \operatorname{sech}^2 \left(\frac{x}{\xi} \right). \quad (\text{B.25})$$

Therefore,

$$j_y^{\text{bound}}(x) = -\frac{mv_F N_0 \Delta}{6} \operatorname{sech}^2 \left(\frac{x}{\xi} \right). \quad (\text{B.26})$$

According to the same procedure below eq. (B.13), angular momentum from the bound state is

$$L_z^{\text{bound}} = N\hbar. \quad (\text{B.27})$$

For the continuum $E < -\Delta \sin \theta$,

$$g_0^R(x, \mathbf{k}, E) = -\frac{1}{\sqrt{E^2 - \Delta^2 \sin^2 \theta}} \left[E + \frac{\Delta^2 \sin^2 \theta \cos^2 \phi}{2(\Delta \sin \theta \sin \phi - E)} \operatorname{sech}^2 \left(\frac{x}{\xi} \right) \right]. \quad (\text{B.28})$$

By the ϕ -integration,

$$\begin{aligned} & \int_0^{2\pi} \frac{d\phi}{2\pi} \sin \phi \operatorname{Re} [g_0^R(x, \mathbf{k}, E)] \\ &= -\frac{\Delta^2 \sin^2 \theta}{2\sqrt{E^2 - \Delta^2 \sin^2 \theta}} \operatorname{sech}^2 \left(\frac{x}{\xi} \right) \int_0^{2\pi} \frac{d\phi}{2\pi} \frac{\sin \phi \cos^2 \phi}{\Delta \sin \theta \sin \phi - E} \\ &= -\frac{\Delta^2 \sin^2 \theta}{2\sqrt{E^2 - \Delta^2 \sin^2 \theta}} \operatorname{sech}^2 \left(\frac{x}{\xi} \right) \frac{\Delta^2 \sin^2 \theta - 2E(E + \sqrt{E^2 - \Delta^2 \sin^2 \theta})}{2\Delta^3 \sin^3 \theta} \\ &= \frac{1}{4\Delta \sin \theta} \left[\sqrt{E^2 - \Delta^2 \sin^2 \theta} + \frac{E^2}{\sqrt{E^2 - \Delta^2 \sin^2 \theta}} + 2E \right] \operatorname{sech}^2 \left(\frac{x}{\xi} \right). \end{aligned} \quad (\text{B.29})$$

By the energy-integration,

$$\begin{aligned} & \int_{-\infty}^{-\Delta \sin \theta} dE \int_0^{2\pi} \frac{d\phi}{2\pi} \sin \phi \operatorname{Re} [g_0^R(x, \mathbf{k}, E)] \\ &= \frac{1}{4\Delta \sin \theta} \operatorname{sech}^2 \left(\frac{x}{\xi} \right) \int_{-\infty}^{-\Delta \sin \theta} dE \left[\sqrt{E^2 - \Delta^2 \sin^2 \theta} + \frac{E^2}{\sqrt{E^2 - \Delta^2 \sin^2 \theta}} + 2E \right] \\ &= \frac{1}{4\Delta \sin \theta} \operatorname{sech}^2 \left(\frac{x}{\xi} \right) \lim_{E \rightarrow \infty} \left[\Delta^2 \sin^2 \theta + E^2 \sqrt{1 - \left(\frac{\Delta \sin^2 \theta}{E} \right)^2} - E^2 \right] \\ &= \frac{1}{4\Delta \sin \theta} \operatorname{sech}^2 \left(\frac{x}{\xi} \right) \lim_{E \rightarrow \infty} \left[\Delta^2 \sin^2 \theta + E^2 \left\{ 1 - \frac{1}{2} \left(\frac{\Delta \sin^2 \theta}{E} \right)^2 \right\} - E^2 \right] \\ &= \frac{\Delta \sin \theta}{8} \operatorname{sech}^2 \left(\frac{x}{\xi} \right). \end{aligned} \quad (\text{B.30})$$

By the θ -integration,

$$\int_0^\pi \frac{d\theta \sin^2 \theta}{2} \int_{-\infty}^{-\Delta \sin \theta} dE \int_0^{2\pi} \frac{d\phi}{2\pi} \sin \phi \operatorname{Re} [g_0^R(x, \mathbf{k}, E)] = \frac{\Delta}{12} \operatorname{sech}^2 \left(\frac{x}{\xi} \right). \quad (\text{B.31})$$

Therefore, from the continuum, mass current is

$$j_y^{\text{cont}}(x) = \frac{mv_F N_0 \Delta}{12} \operatorname{sech}^2\left(\frac{x}{\xi}\right), \quad (\text{B.32})$$

and angular momentum is

$$L_z^{\text{cont}} = -\frac{N\hbar}{2}. \quad (\text{B.33})$$

Finally, total angular momentum is

$$L_z = L_z^{\text{bound}} + L_z^{\text{cont}} = \frac{N\hbar}{2}. \quad (\text{B.34})$$

Appendix C

Ginzburg-Landau functional under rotation

We start with the Hamiltonian in a co-rotating frame:

$$H = H_0 - \boldsymbol{\Omega} \cdot \mathbf{L}, \quad (\text{C.1})$$

$$H_0 = \sum_i [(p_i^2/2m) + U(\mathbf{r}_i)] + V, \quad (\text{C.2})$$

where H_0 is the Hamiltonian in a non-rotating system, consisting of the kinetic energy term, the harmonic trap potential term U and the interaction energy term V . The angular velocity due to the external rotation is $\boldsymbol{\Omega}$ and the angular momentum is $\mathbf{L} = \sum_i 1/2 (\mathbf{r}_i \times \mathbf{p}_i - \mathbf{p}_i \times \mathbf{r}_i)$. We can write H in the form

$$H = \sum_i \left[\frac{1}{2m} (\mathbf{p}_i - m\mathbf{v}_{n,i})^2 + U(\mathbf{r}_i) \right] + V - \sum_i \frac{1}{2} m\mathbf{v}_{n,i}^2, \quad (\text{C.3})$$

where $\mathbf{v}_{n,i} = \boldsymbol{\Omega} \times \mathbf{r}_i$ is the ‘‘normal fluid’’ velocity at the location of the particle i . The last term is the centrifugal energy.

The gradient energy given by the first term of the Hamiltonian (C.3)

$$f_{\text{grad}} = \frac{7\zeta(3)N(0)}{16(\pi k_B T_c)^2} [(\mathbf{p}^* - m\mathbf{v}_n)_i A_j^*] [(\mathbf{p} - m\mathbf{v}_n)_k A_l] \langle v_{Fi} k_j v_{Fk} k_l \rangle_{\mathbf{k}}, \quad (\text{C.4})$$

where $\langle \dots \rangle_{\mathbf{k}}$ denotes the Fermi surface average. Taking the contraction of the subscripts in the Fermi surface average, the mean value is finite. Replacing \mathbf{p} with $-i\hbar\nabla$, we obtain the well-known form of the gradient energy [2]

$$f_{\text{grad}} = K_1(\partial_i^* A_j^*)(\partial_i A_j) + K_2(\partial_i^* A_j^*)(\partial_j A_i) + K_3(\partial_i^* A_i^*)(\partial_j A_j). \quad (\text{C.5})$$

In a similar manner, the centrifugal energy given by the last term of the Hamiltonian (C.3) can be recast into

$$f_{\text{cent}} = - \frac{7\zeta(3)N(0)}{16(\pi k_B T_c)^2} [(m\mathbf{v}_n)_i A_j^*] [(m\mathbf{v}_n)_k A_l] \langle v_{Fi} k_j v_{Fk} k_l \rangle_{\mathbf{k}} \quad (\text{C.6})$$

$$= - \frac{m^2}{\hbar^2} [K_1(\boldsymbol{\Omega} \times \mathbf{r})_i A_j^*(\boldsymbol{\Omega} \times \mathbf{r})_i A_j + K_2(\boldsymbol{\Omega} \times \mathbf{r})_i A_j^*(\boldsymbol{\Omega} \times \mathbf{r})_j A_i + K_3(\boldsymbol{\Omega} \times \mathbf{r})_i A_i^*(\boldsymbol{\Omega} \times \mathbf{r})_j A_j]. \quad (\text{C.7})$$

Taking $\boldsymbol{\Omega} \parallel \hat{\mathbf{z}}$, and $\boldsymbol{\Omega} \times \mathbf{r} = \Omega \rho \hat{\boldsymbol{\theta}}$, we finally obtain the expression of the centrifugal potential as

$$f_{\text{cent}} = -\frac{m^2}{\hbar^2} \Omega^2 \rho^2 (K_1 A_i^* A_i + K_2 |A_\theta|^2 + K_3 |A_\theta|^2). \quad (\text{C.8})$$

Appendix D

Bulk energy in Ginzburg-Landau functional

The bulk free energy (7.7) is written as

$$f_{\text{bulk}} = - (1 - t_x)(|A_x|^2 + |A_y|^2) - (1 - \alpha t_x)|A_z|^2 + \frac{1}{2}(|A_x|^2 + |A_y|^2 + |A_z|^2)^2 + \frac{1}{4}(A_x^{*2} + A_y^{*2} + A_z^{*2})(A_x^2 + A_y^2 + A_z^2). \quad (\text{D.1})$$

By taking A_x real, $A_y = |A_y|e^{i\theta_y}$ and $A_z = |A_z|e^{i\theta_z}$ without loss of generality, we write it as

$$f_{\text{bulk}} = - (1 - t_x)(|A_x|^2 + |A_y|^2) - (1 - \alpha t_x)|A_z|^2 + \frac{3}{4}(|A_x|^4 + |A_y|^4 + |A_z|^4) + (|A_x|^2|A_y|^2 + |A_y|^2|A_z|^2 + |A_z|^2|A_x|^2) + \frac{1}{2} [|A_x|^2|A_y|^2 \cos 2\theta_y + |A_y|^2|A_z|^2 \cos(2\theta_y - 2\theta_z) + |A_z|^2|A_x|^2 \cos 2\theta_z]. \quad (\text{D.2})$$

There are six cases, which are possibly the minimum solutions: (i) $\theta_y = \theta_z = 0$, (ii) $\theta_y = 0$, $\theta_z = \pi/2$, (iii) $\theta_y = \pi/2$, $\theta_z = 0$, (iv) $\theta_y = \pi/2$, $\theta_z = \pi/2$. (v) $\theta_y = \pi/3$, $\theta_z = 2\pi/3$ and (vi) $|A_x|^2 = |A_y|^2 = 0$.

The relevant minimum solutions are found for (ii) and (vi). In the former case (ii) the solution is given by

$$f_{\text{bulk}} = -\frac{1}{8}[3(1 - t_x)^2 - 2(1 - t_x)(1 - \alpha t_x) + 3(1 - \alpha t_x)^2],$$

$$|A_x|^2 + |A_y|^2 = \frac{1}{4}[3(1 - t_x) - (1 - \alpha t_x)], \quad (\text{D.3})$$

$$|A_z|^2 = \frac{1}{4}[-(1 - t_x) + 3(1 - \alpha t_x)].$$

This solution is valid for $2 + (-3 + \alpha)t_x \geq 0$, which determines the boundary between this phase called the A phase and the single component phase called B phase below. The other solution for (vi) is expressed as

$$f_{\text{bulk}} = -\frac{1}{8}(1 - \alpha t_x)^2, \quad (\text{D.4})$$

$$|A_z|^2 = \frac{2}{3}(1 - \alpha t_x).$$

This B phase is described by a single component, thus it corresponds to the so-called polar phase.

Bibliography

- [1] D. Osheroff, R. Richardson, and D. Lee: Phys. Rev. Lett. **28** (1972) 885.
- [2] D. Vollhardt and P. Wölfle: *The Superfluid Phase of Helium 3* (Taylor and Francis, London, 1990).
- [3] F. Wilczek: Nat. Phys. **5** (2009) 614.
- [4] C. J. Pethick and H. Smith: *Bose-Einstein Condensation in Dilute Gases* (Cambridge University Press, Cambridge, 2008).
- [5] M. H. Anderson, J. R. Ensher, M. R. Matthews, C. E. Wieman, and E. A. Cornell: Science **269** (1995) 198.
- [6] K. B. Davis, M. O. Mewes, M. R. Andrews, N. J. van Druten, D. S. Durfee, D. M. Kurn, and W. Ketterle: Phys. Rev. Lett. **75** (1995) 3969.
- [7] C. C. Bradley, C. A. Sackett, J. J. Tollett, and R. G. Hulet: Phys. Rev. Lett. **75** (1995) 1687.
- [8] M. Greiner, C. A. Regal, and D. S. Jin: Nature **426** (2003) 537.
- [9] S. Jochim, M. Bartenstein, A. Altmeyer, G. Hendl, S. Riedl, C. Chin, J. H. Denschlag, and R. Grimm: Science **302** (2003) 2101.
- [10] M. W. Zwierlein, C. A. Stan, C. H. Schunck, S. M. F. Raupach, S. Gupta, Z. Hadzibabic, and W. Ketterle: Phys. Rev. Lett. **91** (2003) 250401.
- [11] C. Regal, M. Greiner, and D. Jin: Phys. Rev. Lett. **92** (2004) 040403.
- [12] M. W. Zwierlein, C. A. Stan, C. H. Schunck, S. M. F. Raupach, A. J. Kerman, and W. Ketterle: Phys. Rev. Lett. **92** (2004) 120403.
- [13] J. Zhang, E. van Kempen, T. Bourdel, L. Khaykovich, J. Cubizolles, F. Chevy, M. Teichmann, L. Tarruell, S. Kokkelmans, and C. Salomon: Phys. Rev. A **70** (2004) 030702.
- [14] C. Schunck, M. Zwierlein, C. Stan, S. Raupach, W. Ketterle, A. Simoni, E. Tiesinga, C. Williams, and P. Julienne: Phys. Rev. A **71** (2005) 045601.
- [15] Y. Inada, M. Horikoshi, S. Nakajima, M. Kuwata-Gonokami, M. Ueda, and T. Mukaiyama: Phys. Rev. Lett. **101** (2008) 100401.
- [16] C. Regal, C. Ticknor, J. Bohn, and D. Jin: Phys. Rev. Lett. **90** (2003) 053201.

- [17] C. Ticknor, C. A. Regal, D. S. Jin, and J. L. Bohn: Phys. Rev. A **69** (2004) 042712.
- [18] J. Gaebler, J. Stewart, J. Bohn, and D. Jin: Phys. Rev. Lett. **98** (2007) 200403.
- [19] Y. Tsutsumi and K. Machida: J. Phys. Soc. Jpn. **78** (2009) 114606.
- [20] Y. Tsutsumi: *Busseikenkyuu* **94** (2010) 26.
- [21] Y. Tsutsumi, T. Mizushima, M. Ichioka, and K. Machida: J. Phys. Soc. Jpn. **79** (2010) 113601.
- [22] Y. Tsutsumi, T. Mizushima, M. Ichioka, and K. Machida: J. Low Temp. Phys. **162** (2011) 196.
- [23] Y. Tsutsumi, M. Ichioka, and K. Machida: to be published in Phys. Rev. B.
- [24] Y. Tsutsumi and K. Machida: Phys. Rev. A **80** (2009) 035601.
- [25] Y. Tsutsumi and K. Machida: J. Phys. Soc. Jpn. **78** (2009) 084702.
- [26] Y. Tsutsumi and K. Machida: J. Phys. Soc. Jpn. **79** (2010) 034301.
- [27] G. Eilenberger: Z. Phys. **214** (1968) 195.
- [28] Y. Nagato, K. Nagai, and J. Hara: J. Low Temp. Phys. **93** (1993) 33.
- [29] N. Schopohl and K. Maki: Phys. Rev. B **52** (1995) 490.
- [30] N. D. Mermin: Phys. Rev. A **9** (1974) 868.
- [31] N. D. Mermin: Phys. Rev. B **13** (1976) 112.
- [32] G. Barton and M. A. Moore: J. Phys. C **7** (1974) 2989.
- [33] H. Adachi, Y. Tsutsumi, and K. Machida: J. Phys. Soc. Jpn. **79** (2010) 044301.
- [34] A. J. Leggett: Rev. Mod. Phys. **47** (1975) 331.
- [35] M. M. Salomaa and G. E. Volovik: Rev. Mod. Phys. **59** (1987) 533.
- [36] P. W. Anderson and P. Morel: Phys. Rev. **123** (1961) 1911.
- [37] P. W. Anderson and W. F. Brinkman: Phys. Rev. Lett. **30** (1973) 1108.
- [38] R. Balian and N. R. Werthamer: Phys. Rev. **131** (1963) 1553.
- [39] M. C. Cross and W. F. Brinkman: J. Low Temp. Phys. **27** (1977) 683.
- [40] M. M. Salomaa and G. E. Volovik: Phys. Rev. Lett. **55** (1985) 1184.
- [41] D. A. Ivanov: Phys. Rev. Lett. **86** (2001) 268.
- [42] T. Kawakami, Y. Tsutsumi, and K. Machida: Phys. Rev. B **79** (2009) 092506.
- [43] T. Kawakami, Y. Tsutsumi, and K. Machida: J. Phys. Soc. Jpn. **79** (2010) 044607.
- [44] M. Yamashita, K. Izumina, A. Matsubara, Y. Sasaki, O. Ishikawa, T. Takagi, M. Kubota, and T. Mizusaki: Phys. Rev. Lett. **101** (2008) 025302.

- [45] D. M. Stamper-Kurn, M. R. Andrews, A. P. Chikkatur, S. Inouye, H.-J. Miesner, J. Stenger, and W. Ketterle: *Phys. Rev. Lett.* **80** (1998) 2027.
- [46] J. Stenger, S. Inouye, D. M. Stamper-Kurn, H. J. Miesner, A. P. Chikkatur, and W. Ketterle: *Nature* **396** (1998) 345.
- [47] T. Ohmi and K. Machida: *J. Phys. Soc. Jpn.* **67** (1998) 1822.
- [48] T.-L. Ho: *Phys. Rev. Lett.* **81** (1998) 742.
- [49] C. A. Regal and D. S. Jin: *Phys. Rev. Lett.* **90** (2003) 230404.
- [50] C.-H. Cheng and S.-K. Yip: *Phys. Rev. Lett.* **95** (2005) 070404.
- [51] C.-H. Cheng and S.-K. Yip: *Phys. Rev. B* **73** (2006) 064517.
- [52] C. Nayak, S. H. Simon, A. Stern, M. Freedman, and S. Das Sarma: *Rev. Mod. Phys.* **80** (2008) 1083.
- [53] G. Moore and N. Read: *Nucl. Phys. B* **360** (1991) 362.
- [54] N. Read and D. Green: *Phys. Rev. B* **61** (2000) 10267.
- [55] L. Fu and C. L. Kane: *Phys. Rev. Lett.* **100** (2008) 096407.
- [56] M. Sato, Y. Takahashi, and S. Fujimoto: *Phys. Rev. Lett.* **103** (2009) 020401.
- [57] C. Caroli, P. de Gennes, and J. Matricon: *Phys. Lett.* **9** (1964) 307.
- [58] N. B. Kopnin and M. M. Salomaa: *Phys. Rev. B* **44** (1991) 9667.
- [59] G. E. Volovik: *JETP Lett.* **57** (1993) 244.
- [60] G. E. Volovik: *Pis'ma Zh. Eksp. Teor. Fiz.* **70** (1999) 601.
- [61] G. E. Volovik: *The Universe in a Helium Droplet* (Clarendon Press, Oxford, 2003).
- [62] A. Y. Kitaev: *Annals of Physics* **303** (2003) 2.
- [63] C. Zhang, S. Tewari, and S. Das Sarma: *Phys. Rev. Lett.* **99** (2007) 220502.
- [64] M. Stone and R. Roy: *Phys. Rev. B* **69** (2004) 184511.
- [65] S. B. Chung and S.-C. Zhang: *Phys. Rev. Lett.* **103** (2009) 235301.
- [66] G. E. Volovik: *Pis'ma Zh. Eksp. Teor. Fiz.* **90** (2009) 440.
- [67] G. E. Volovik: *Pis'ma Zh. Eksp. Teor. Fiz.* **90** (2009) 639.
- [68] Y. Nagato, S. Higashitani, and K. Nagai: *J. Phys. Soc. Jpn.* **78** (2009) 123603.
- [69] N. Mermin and T.-L. Ho: *Phys. Rev. Lett.* **36** (1976) 594.
- [70] P. Anderson and G. Toulouse: *Phys. Rev. Lett.* **38** (1977) 508.
- [71] T. Mizushima, K. Machida, and T. Kita: *Phys. Rev. Lett.* **89** (2002) 030401.

- [72] A. Leanhardt, Y. Shin, D. Kielpinski, D. Pritchard, and W. Ketterle: Phys. Rev. Lett. **90** (2003) 140403.
- [73] W. Pogosov, R. Kawate, T. Mizushima, and K. Machida: Phys. Rev. A **72** (2005) 063605.
- [74] K. Wright, L. Leslie, A. Hansen, and N. Bigelow: Phys. Rev. Lett. **102** (2009) 030405.
- [75] L. Buchholtz and A. Fetter: Phys. Lett. A **58** (1976) 93.
- [76] L. Buchholtz and A. Fetter: Phys. Rev. B **15** (1997) 5225.
- [77] R. Ishiguro: Dr. Thesis, Kyoto University (2003).
- [78] R. Ishiguro, O. Ishikawa, M. Yamashita, Y. Sasaki, K. Fukuda, M. Kubota, H. Ishimoto, R. Packard, T. Takagi, T. Ohmi, and T. Mizusaki: Phys. Rev. Lett. **93** (2004) 125301.
- [79] R. Ishiguro, K. Izumina, M. Kubota, O. Ishikawa, Y. Sasaki, and T. Takagi: presented at JPS 62nd Annual Meeting (2007).
- [80] K. Izumina, T. Igarashi, M. Kubota, R. Ishiguro, O. Ishikawa, Y. Sasaki, and T. Takagi: presented at JPS 2008 Autumn Meeting (2008).
- [81] K. Izumina: private communication.
- [82] T. Takagi: J. Phys. Chem. of Solids **66** (2005) 1355.
- [83] P. de Gennes: Phys. Lett. A **44** (1973) 271.
- [84] V. Ambegaokar, P. de Gennes, and D. Rainer: Phys. Rev. A **9** (1974) 2676.
- [85] K. Maki: J. Low Temp. Phys. **32** (1978) 1.
- [86] J. Wheatley: Rev. Mod. Phys. **47** (1975) 415.
- [87] J. Sauls and J. Serene: Phys. Rev. B **24** (1981) 183.
- [88] D. S. Greywall: Phys. Rev. B **33** (1986) 7520.
- [89] E. Thuneberg: J. Low Temp. Phys. **122** (2001) 657.
- [90] H. Choi, J. Davis, J. Pollanen, T. Haard, and W. Halperin: Phys. Rev. B **75** (2007) 174503.
- [91] E. Thuneberg: Phys. Rev. B **36** (1987) 3583.
- [92] T. Kita: Phys. Rev. B **66** (2002) 224515.
- [93] K. Aoyama and R. Ikeda: Phys. Rev. B **76** (2007) 104512.
- [94] V. Ruutu, Ü. Parts, and K. Krusius: J. Low Temp. Phys. **103** (1996) 331.
- [95] E. R. Dobbs: *Helium Three* (Oxford University Press, New York, 2000).
- [96] T. Takagi: private communication.

- [97] Y. Tsutsumi, T. Kawakami, T. Mizushima, M. Ichioka, and K. Machida: *Phys. Rev. Lett.* **101** (2008) 135302.
- [98] Y.-H. Li and T.-L. Ho: *Phys. Rev. B* **38** (1988) 2362.
- [99] A. B. Vorontsov and J. A. Sauls: *Phys. Rev. B* **68** (2003) 064508.
- [100] R. G. Bennett, L. V. Levitin, A. Casey, B. Cowan, J. Parpia, and J. Saunders: *J. Low Temp. Phys.* **158** (2010) 163.
- [101] M. Saitoh and K. Kono: *J. Low Temp. Phys.* **148** (2007) 483.
- [102] J. W. Serene and D. Rainer: *Phys. Rep.* **101** (1983) 221.
- [103] N. Schopohl: *J. Low Temp. Phys.* **41** (1980) 409.
- [104] M. Fogelström and J. Kurkijärvi: *J. Low Temp. Phys.* **98** (1995) 195.
- [105] Y. Wada, S. Murakawa, Y. Tamura, M. Saitoh, Y. Aoki, R. Nomura, and Y. Okuda: *Phys. Rev. B* **78** (2008) 214516.
- [106] A. B. Vorontsov and J. A. Sauls: *Phys. Rev. Lett.* **98** (2007) 045301.
- [107] A. L. Fetter: *Phys. Rev. B* **14** (1976) 2801.
- [108] L. J. Buchholtz and G. Zwicknagl: *Phys. Rev. B* **23** (1981) 5788.
- [109] Y. Nagato, M. Yamamoto, and K. Nagai: *J. Low Temp. Phys.* **110** (1998) 1135.
- [110] M. Cheng, R. M. Lutchyn, V. Galitski, and S. Das Sarma: *Phys. Rev. Lett.* **103** (2009) 107001.
- [111] T. Mizushima and K. Machida: *Phys. Rev. A* **82** (2010) 023624.
- [112] H. Choi, J. P. Davis, J. Pollanen, and W. P. Halperin: *Phys. Rev. Lett.* **96** (2006) 125301.
- [113] Y. Okuda: private communication.
- [114] R. Shindou, A. Furusaki, and N. Nagaosa: *Phys. Rev. B* **82** (2010) 180505.
- [115] A. C. Forbes and A. F. G. Wyatt: *Phys. Rev. Lett.* **64** (1990) 1393.
- [116] M. P. Enrico, S. N. Fisher, A. M. Guénault, G. R. Pickett, and K. Torizuka: *Phys. Rev. Lett.* **70** (1993) 1846.
- [117] T. Okuda, H. Ikegami, H. Akimoto, and H. Ishimoto: *Phys. Rev. Lett.* **80** (1998) 2857.
- [118] K. Kono: *J. Low Temp. Phys.* **158** (2010) 288.
- [119] S. Murakawa, Y. Tamura, Y. Wada, M. Wasai, M. Saitoh, Y. Aoki, R. Nomura, Y. Okuda, Y. Nagato, M. Yamamoto, S. Higashitani, and K. Nagai: *Phys. Rev. Lett.* **103** (2009) 155301.
- [120] S. Murakawa, A. Yamaguchi, M. Arai, M. Wasai, Y. Aoki, H. Ishimoto, R. Nomura, and Y. Okuda: *J. Low Temp. Phys.* **158** (2010) 141.

- [121] S. Murakawa, Y. Wada, Y. Tamura, M. Wasai, M. Saitoh, Y. Aoki, R. Nomura, Y. Okuda, Y. Nagato, M. Yamamoto, S. Higashitani, and K. Nagai: *J. Phys. Soc. Jpn.* **80** (2011) 013602.
- [122] V. Gurarie, L. Radzihovsky, and A. Andreev: *Phys. Rev. Lett.* **94** (2005) 230403.
- [123] T.-L. Ho and R. B. Diener: *Phys. Rev. Lett.* **94** (2005) 090402.
- [124] Y. Ohashi: *Phys. Rev. Lett.* **94** (2005) 050403.
- [125] K. Quader, R. Liao, and F. Popescu: *Int. J. Mod. Phys. B* **22** (2008) 4358.
- [126] S. Tewari, S. Das Sarma, C. Nayak, C. Zhang, and P. Zoller: *Phys. Rev. Lett.* **98** (2007) 010506.
- [127] M. Baranov and D. Petrov: *Phys. Rev. A* **58** (1998) R801.
- [128] M. Baranov and M. Kugan: *Physica B* **191** (1993) 341.
- [129] A.-C. Ji, W. M. Liu, J. L. Song, and F. Zhou: *Phys. Rev. Lett.* **101** (2008) 010402.
- [130] T. Mizushima, M. Ichioka, and K. Machida: *Phys. Rev. Lett.* **101** (2008) 150409.
- [131] S. Stock, Z. Hadzibabic, B. Battelier, M. Cheneau, and J. Dalibard: *Phys. Rev. Lett.* **95** (2005) 190403.
- [132] Z. Hadzibabic, P. Krüger, M. Cheneau, B. Battelier, and J. Dalibard: *Nature* **441** (2006) 1118.
- [133] J. A. Sauls and M. Eschrig: *New J. Phys.* **11** (2009) 075008.
- [134] M. Eschrig and J. Sauls: *New J. Phys.* **11** (2009) 075009.
- [135] T. Isoshima, K. Machida, and T. Ohmi: *J. Phys. Soc. Jpn.* **70** (2001) 1604.
- [136] M. Ichioka and K. Machida: *Phys. Rev. B* **65** (2002) 224517.
- [137] T. Mizushima, N. Kobayashi, and K. Machida: *Phys. Rev. A* **70** (2004) 043613.
- [138] T. Kawakami, T. Mizushima, and K. Machida: arXiv:1010.5038.
- [139] K. Kawasaki, T. Yoshida, M. Tarui, H. Nakagawa, H. Yano, O. Ishikawa, and T. Hata: *Phys. Rev. Lett.* **93** (2004) 105301.